# Electrochemical dissolution of Fe in concentrated aqueous electrolyte

Hind Aati Almalki

Supervisor: Prof. Katherine B. Holt

A Thesis Submitted to University College London

For The Degree of Doctor of Philosophy

2021-2024

## DECLARATION

I, Hind Aati Almalki confirm that the work presented in this thesis is my own. Where information has been derived from other sources, I confirm that this has been indicated in the thesis.'

Date : 30th of July 2024

Signature of candidate :……..

## ACKNOWLEDGEMENTS

I would like to express my deep gratitude to my supervisor, Katherine, for her unwavering support and invaluable insight during my doctoral research. Her guidance was instrumental in completing my research. I thank her for believing in me and for providing the guidance I needed to overcome the challenges I faced along the way.

I am so grateful to my parents for their unconditional love and support. Their belief in me and constant encouragement have been the foundation of my success. They instilled in me the values of hard work and perseverance, and I am so grateful for their endless love and support.

To my husband, Ahmed, whose unwavering support and understanding have been my rock throughout this journey. His patience and faith in me were indispensable. I thank him for always being there for me, for his encouragement, and for giving me the strength to persevere.

To my children, I thank them for their collective encouragement and always being there for me.

In the end, I would like to extend my sincere thanks to Umm Al-Qura University in the Kingdom of Saudi Arabia for giving me the opportunity to study abroad and providing the necessary funding for this.

## ABSTRACT

All-iron aqueous redox flow batteries provide a low-cost, safe solution for energy storage by utilising the Fe(II)/Fe(0) couple ($Fe^0 \rightarrow Fe^{2+} + 2e^-$) at the anode and the Fe(III)/Fe(II) couple ($Fe^{3+} + e^- \rightarrow Fe^{2+}$) at the cathode. While the simplicity of this battery design is attractive, several fundamental challenges must be overcome to allow full exploitation. These include slow kinetics for the $Fe^{2+}/Fe^0$ plating and stripping reaction leading to decreased coulombic efficiency and competing $H_2O$ reduction at the Fe electrode leading to harmful $H_2$ generation.

In this thesis the $Fe^{2+}/Fe^0$ redox response, measured using cyclic voltammetry, varies with electrolyte concentration (from 0.1 M to 2.5 M $Li_2SO_4$). At lower concentrations (from 0.1 M to 1.8 M), the iron dissolution rate increases with the electrolyte concentration and the reaction is rapid. At high concentrations (2.0 M and above), the CV results found that the current drops and the iron dissolution reaction stops.

To understand these results, the viscosity, conductivity, and infrared spectra of lithium sulfate solutions were measured with different concentrations. The viscosity increases with increasing concentration from 0.1 to 1.8 M. Also, the conductivity increases as the concentration increases from 0.1 to 1.8 M. When concentrations exceed 1.8 M, the viscosity increases more significantly and there is no further increase in conductivity values. Turning to the infrared result, there are changes in the structure of water in the electrolyte with increasing concentration. From 0.1 to 1.8 M, ions are more independent of each other. When concentrations reach higher than 1.8 M, an ionic interaction occurs between sulfate and lithium, which causes sulfate to lose its symmetry, which is reflected in the IR spectra. Changes also occur in the hydrogen bonds of water as a result of the trapping of water molecules by electrolyte ions. These results together suggest that the slower oxidation of iron at higher concentrations could be due to increased solution viscosity or decreased conductivity due to ions interacting with each other through ion-pairing.

Raman spectroscopy of the iron electrode after oxidation shows formation of iron sulfate surface films in $Li_2SO_4$, which indicates that electrode passivating reactions within the aqueous electrolyte are taking place at 2.0 M and above. This

result is consistent with the CV results where the dissolution of iron stopped, and the current became passivated. This passivation is due to the formation of the iron sulfate film.

In-situ IR spectroelectrochemistry data shows changes to water and electrolyte structure at potentials at which Fe dissolution takes place. At low concentrations, the sulfate peak is more symmetrical, and sulfate does not lose its symmetry, and therefore each ion dissolves separately and does not interact much with other ions. At high concentrations, the IR results show changes in the asymmetric sulfate stretch due to the loss of sulfate symmetry and the appearance of a new peak in the symmetric stretch region. This indicates the presence of interactions between ions in the solution and the formation of ion pairs.

The effect of adding 4.5 M $MgCl_2$ to different concentrations of $Li_2SO_4$ was also investigated to improve the dissolution efficiency of the iron electrode. The results of cyclic voltammetry showed that the dissolution of iron became faster and the deposition of a layer of iron sulphate on the electrode was prevented as the Raman spectra showed few vibrational peaks of sulfate. The IR absorption results show the sulfate peak loses its symmetry at low concentrations. This is because the increase in the number of ions in the solution leads to increased interaction of sulfate with surrounding ions, which leads to broadening and splitting of the peak.

Finally, the redox response of $Fe^{2+}/Fe^{0}$ in LiTFSI from 0.1 M to 15 m was studied. The reaction current decreased and the dissolution rate of iron decreased due to the large size of TFSI anions and the high viscosity of the solution. However, no passivation layer was formed on the surface with adsorption of $TFSI^{-}$ anions on the surface according to the Raman and IR results.

## IMPACT STATEMENT

The primary focus of investigations was on the electrochemical dissolution of iron in concentrated aqueous lithium salt solutions, specifically $Li_2SO_4$ and LiTFSI. These investigations are of relevance to different applications in energy storage, corrosion science, and industrial electrochemical processes. This study offers crucial insights into the behaviour and stability of iron in these environments, which can have an impact on the design and improvement of electrochemical systems.

The solubility characteristics of iron in concentrated $Li_2SO_4$ and LiTFSI solutions have a direct impact on the performance and efficiency of all-iron redox flow batteries. Concentrated electrolytes with high ionic conductivity can improve energy efficiency and power density. Comprehending the rates at which iron dissolves aids in optimising the concentration of electrolytes to achieve a balance between the performance and lifespan of batteries.
Understanding the solubility of iron in lithium electrolytes is valuable for developing sophisticated electrolyte compositions that minimise electrode corrosion, hence prolonging battery lifespan and enhancing safety. Highly concentrated lithium solutions can create stable electrochemical conditions for some electrode materials.

Studying the process of iron dissolving in concentrated electrolytes yields useful information about corrosion mechanisms in situations with high levels of ionic strength. This information is crucial for the advancement of efficient corrosion inhibitors and protective coatings, particularly in environments where $Li_2SO_4$ or LiTFSI are used. Gaining knowledge about the thermodynamics of iron dissolution also facilitated the choice of suitable materials for constructing and sustaining electrochemical systems. This mitigates the likelihood of failures caused by corrosion and decreases maintenance expenses, particularly in the energy and chemical sectors.

The impact of iron's solubility in lithium solutions on the effectiveness and productivity of electroplating procedures is significant. Understanding these

principles enables more precise regulation of deposition rates, surface finishes, and adhesion qualities, resulting in electroplated goods of superior quality.
Studying the process of iron dissolving in highly concentrated aqueous lithium solutions has significant consequences for many electrochemical uses. This study contributes to the progress of energy storage technologies, improves industrial electrochemical processes, and promotes environmental sustainability by offering a more comprehensive comprehension of iron's behaviour in these settings. Further investigation in this field is crucial to stimulate technical advancement and achieve economic and environmental advantages.

Investigation on the electrochemical dissolution of iron in highly concentrated aqueous lithium sulphate ($Li_2SO_4$) solutions, after the addition of magnesium chloride ($MgCl_2$), has yielded significant understanding of the intricate interactions occurring inside electrolyte solutions. These findings are crucial for optimising efficiency in energy storage systems and augmenting industrial electrochemical processes.

The best way to benefit from study, both in and outside of academia, it is essential to disseminate findings through publication in academic publications and presentations at conferences. Thus far, we have successfully showcased our research at three conferences, namely Electrochem 2022, Electrochem 2023, and RSC CNN symposium 2024. In addition, we are currently in the process of preparing our work for imminent publication in an academic journal.

## Table of Contents

## LIST OF FIGURES

## LIST OF TABLES

## LIST OF APPENDIX FIGURES

# CHAPTER 1.

# INTRODUCTION

## 1.1 Introduction to Redox Flow Batteries

Redox flow batteries (RFBs) are a type of electrochemical energy storage device designed to address the challenges of integrating renewable energy sources, like solar and wind, into the power grid. Renewable energy generation is often intermittent and unpredictable, leading to mismatches between energy supply and demand. RFBs help solve this problem by storing excess renewable energy and releasing it when demand is high or when generation is low. During charge and discharge of a redox flow battery, electrochemical reduction and oxidation reactions are used to store energy in liquid electrolyte solutions flowing through electrochemical cells [1].

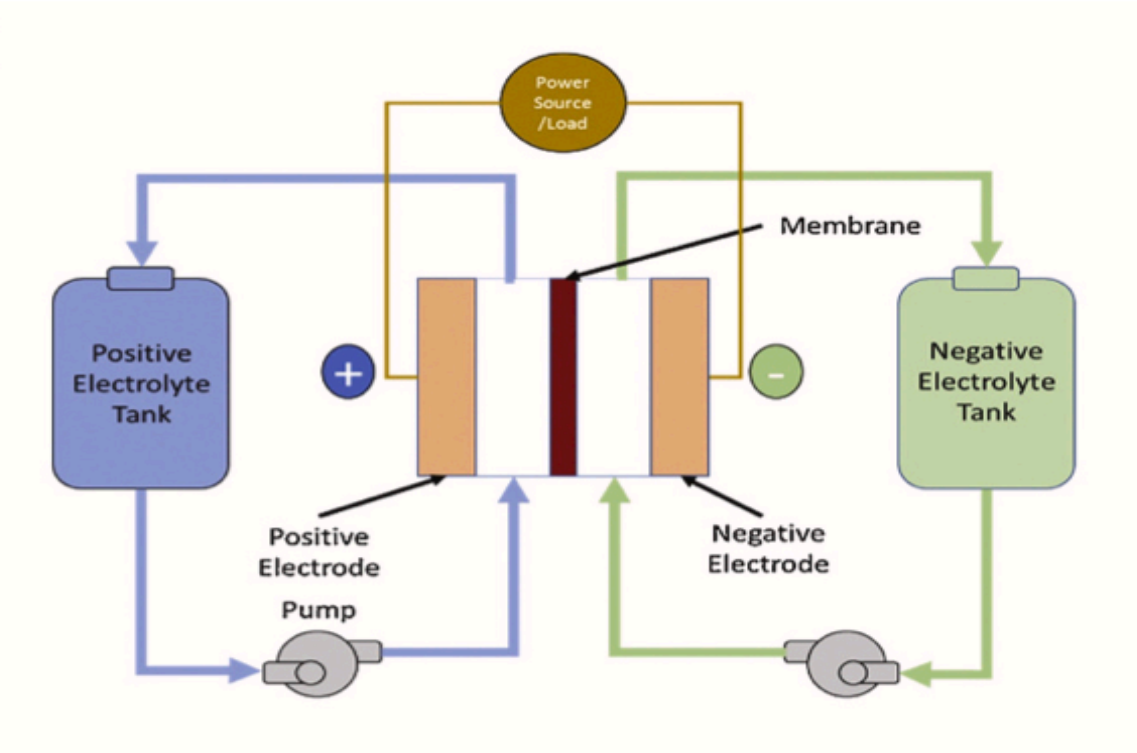


**Figure 1.1** Structure diagram of RFB system, adapted from Ref [2]

As shown in figure 1.1, a RFB consists of two half-cells separated by a porous ion membrane that allows ions to pass through, as well as two electrodes where oxidation and reduction reactions occur. Furthermore, electrolytes contain redox active ions. They are pumped through the cell through external tanks. In doing so, they promote reduction at the positive electrode and oxidation at the negative

electrode, producing an electrical potential. During discharge, on the electrode surfaces, redox reactions occur as follows:

$$C^{x+} + xe^- \rightarrow C \qquad \text{at positive electrode (cathode)} \quad (1.1)$$

$$A \rightarrow A^{x+} + xe^- \qquad \text{at negative electrode (anode)} \quad (1.2)$$

To determine that the reaction in the RFB is spontaneous, the cell potential must be calculated. The cell potential is the difference in the standard reduction potentials for the anode and cathode reactions as in the following equation (1.3):

$$E^0_{Cell} = E^0_{cathode} - E^0_{anode} \qquad (1.3)$$

If the cell potential ($E^0_{cell}$) was positive, this indicates that the reaction occurs spontaneously under standard conditions. The oxidation process occurs at the anode (more negative potential), and reduction occurs at the cathode (more positive potential). A large difference between the potentials causes a spontaneous redox reaction, generating an electric current.

During discharge in RFB, oxidation occurs at the anode and reduction occurs at the cathode, which generates an electric current and the battery reactions are spontaneous. To recharge the battery, an external power source is used, which reverses the electrochemical reactions that occur during discharge. That is, reduction occurs at the anode and oxidation occurs at the cathode.

Aqueous RFB systems have attracted considerable attention due to their superior characteristics over other forms of storage, as shown in Table 1.1. Four advantages can be attributed to redox flow cells: low cost, flexibility of operation, high efficiency, and large scale [3].

**Table 1.1** Comparison between three storage system, adapted from Ref [3]

| Power storage system | Advantages | Disadvantages |
|---|---|---|
| Conventional systems such as: flooded lead-acid battery | Well-known technology<br>Low maintenance<br>Low size | Heavy<br>High construction cost<br>Expensive technology<br>Short life span<br>Not portable |
| Developmental systems such as: sodium/sulphur battery | High energy efficiency<br>Flexible operation | Thermal management<br>Difficult maintenance |
| Redox flow battery | Low cost<br>Flexible operation<br>High efficiency<br>Large scale | Newer technology<br>An extra electrolyte tank is needed<br>Complex monitoring and control |

The use of aqueous electrolytes in batteries and electrochemical cells has certain disadvantages, primarily related to the restricted electrochemical stability window[4] and the possibility of competing reactions, such as hydrogen evolution at the anode during charging. The overall electrochemical stability window for water is 1.23 V, at which water decomposes into $H_2$ and $O_2$ as in the following equations:

Decomposition of water during charging:

At anode: reduction reaction (Hydrogen Evolution Reaction):

$2H_2O + 2e^- \rightarrow H_2 + 2OH^-$ Occurs at 0 V vs SHE (1.4)

At cathode: oxidation reaction (Oxygen Evolution Reaction):

$2H2O \rightarrow O_2 + 4H^+ + 4e^-$ Occurs at 1.23 V vs SHE. (1.5)

This makes the process of choosing an electrode limited, as one must stay away from materials that have working potentials close to those of $H_2$ and $O_2$ evolution.

One of the most popular types of RFB is the vanadium redox flow battery (V-RFB). Its benefits are superior to those of other types. V-RFBs contain a single

element (vanadium) that can exist in different oxidation states in their electrolytes, so cross-contamination is likely to be reduced [5] .The V-RFB is composed of two half-cells that are separated by a membrane to prevent cross-transfer of electrolytes. To maintain the electrical circuit, this membrane transports protons. Nafion is the most widely used material for the membrane of V-RFB batteries due to its high conductivity and chemical stability [6].

A V-RFB cell's electrodes are made from carbon such as carbon felt, carbon paper, carbon cloth, graphite felt, and carbon nanotubes, which have high electrical conductivity, large specific surface area, and low cost. In order to prepare the vanadium electrolytes, vanadium salts are dissolved in sulfuric acid or hydrochloric acid. $VO_2^+$ and $VO^{+2}$ ions are contained in the electrolyte in the positive half-cells, while $V^{+3}$ and $V^{+2}$ ions are present in the electrolyte in the negative half-cells [6]. It is possible to store and release energy electrochemically by changing the valence state of the vanadium species.

In discharge process:

$$V^{2+} \rightarrow V^{3+} + e^- \qquad E^0 = -0.255\ V \quad (1.6)$$

$$VO_2^+ + 2H^+ + e^- \rightarrow VO^{2+} + H_2O \qquad E^0 = +1.004\ V \quad (1.7)$$

The overall reaction:

$$V^{2+} + VO_2^+ + 2H^+ \rightarrow V^{3+} + VO^{2+} + H_2O \qquad E^0 = +1.259\ V \quad (1.8)$$

V-RFB have advantages over other types of batteries, including the longest cycle life for a flow battery. The liquid electrolyte does not degrade significantly, and it can be used for decades without the need to replace it. Additionally, graphite electrodes are extremely stable, and there are very few instances of membrane failure. It is also important to note that V-RFBs have a very low self-discharge rate.

There are a number of disadvantages associated with V-RFB batteries, compared to other types of batteries, including high vanadium metal prices, heavy

weight of aqueous electrolyte and some of its forms of oxidation are toxic. Consequently, it is important to avoid using vanadium and to choose an environmentally friendly type such as iron-based types (Fe-RFB), which are also less expensive and more readily available [7] as shown in Table 1.2.

**Table 1.2** Characteristic of Vanadium-RFB compared with Fe-RFB, adapted from Ref [8]

| Vanadium-RFB | Fe-RFB |
|---|---|
| High efficiency 80-90% | Lower efficiency 80-60% |
| High toxic | Eco-friendly |
| High cost<br>$500-700/kwh | Lower cost<br>$100-200/kwh |

## 1.2. Types of iron-redox flow battery

Reactions associated with the iron-based RFBs are the focus of this thesis. A brief description of different types of reported Fe-RFB will be presented in this section:

1- All-iron redox flow battery (Fe-RFB): The system includes only one element, with the Fe(II)/Fe(0) couple ($Fe^0 \rightarrow Fe^{2+} + 2e^-$) at the anode and Fe(III)/Fe(II) couple ($Fe^{3+} + e^- \rightarrow Fe^{2+}$) at the cathode . As a result of studies of this system, significant progress has been made in controlling the oxidation-reduction potential window. Iron has the advantage of not suffering from many of the problems that other materials suffer from, being inexpensive, readily available, and non-toxic. Despite these advantages, the problem of hydrogen gas generation at the anode during charging remains an issue [2].

2- Iron-chromium redox flow battery (FeCr-RFB): This system is based on $Fe^{2+}/Fe^{3+}$ (positive electrode) and $Cr^{3+}/Cr^{2+}$ (negative electrode) redox pairs. Although the Fe/Cr system has many advantages such as low cost and available materials, it has some disadvantages that must be overcome, including the need for a specific electrocatalyst for the slow $Cr^{3+/2+}$ reaction and hydrogen gas generation as a side reaction [9].

3- Iron-vanadium redox flow battery (FeV-RFB): This has better electrochemical activity (faster kinetics) than the FeCr-RFB system, as well as a higher operating temperature range, so there is no need for a catalyst in the system. Furthermore, it is possible to control the hydrogen evolution [10]. However, the disadvantages of the high cost of vanadium salts remains.

4- Iron-lead redox flow battery (FeLRFB): A new RFB system using $Pb/Pb^{2+}$ and $Fe^{2+}/Fe^{3+}$ as redox pairs for anolytes and catholytes [2]. The environmental toxicity of Pb remains a disadvantage.

5- Iron-cadmium redox flow battery (FeCd-RFB): The cadmium plates the electrode very efficiently in the acidic medium, which reduces the competing generation of hydrogen gas, but the accumulated cadmium blocks the current, resulting in a reduction in battery efficiency [2].

6- Zinc-iron redox flow battery (ZnFe-RFB): The zinc redox couple has been suggested for its properties, including its fast kinetics and abundant availability. There is, however, a risk of zinc dendrites forming and battery life being decreased due to its high solubility [11].

7- Tin-iron redox flow battery (SnFe-RFB): Tin exhibits fast kinetics and low toxicity. Therefore, it might be an ideal anode material for RFBs. However, the generation of hydrogen gas during the charging process may severely limit the cycle performance of the system [12].

All of these examples use the $Fe^{2+/3+}$ redox couple as the positive electrode, with the negative electrode being different in each case. An ideal negative electrode reaction has yet to be identified, as all show either slow kinetics or compete with the hydrogen evolution reaction in aqueous solutions.

### 1.3. All-iron redox flow battery

Based on the Fe-RFB examples described above, the all-iron RFB in particular is attractive for further investigation. Since iron is readily available, low in cost,

and does not have adverse health consequences, it distinguishes itself from other metals. The hydrogen evolution side reaction at the iron anode is less compared with some other metal anodes. Since the standard reduction potential of the $Fe^{2+}/Fe$ redox couple is -0.44 V vs SHE, which is negative enough to avoid interference with the hydrogen evolution reaction potential under standard conditions, the driving force for HER is limited. Therefore, the all-iron cell is in principle more efficient [7].

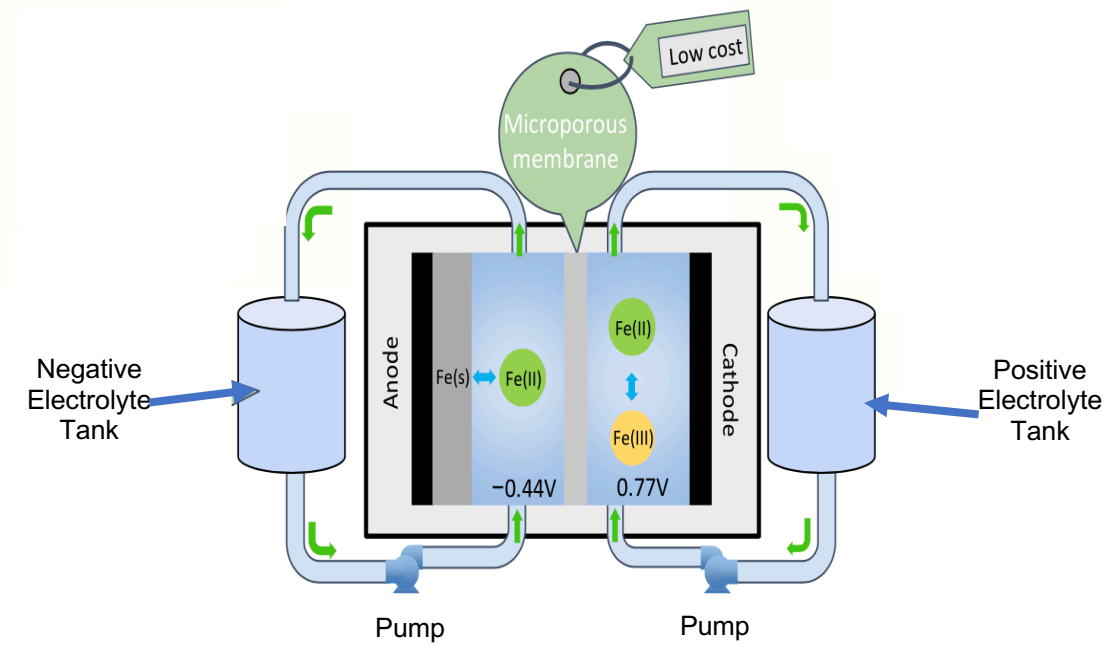


**Figure 1.2** Structure diagram of all iron-RFB system, adapted from Ref [13]

A diagram of the all-iron Fe-RFB is shown in figure 1.2 As with all RFB, the Fe-RFB consists of two halves of a cell that are separated by an ion membrane. The electrolytes are dissolved ferrous salts, which are typically in the form of chlorides ($FeCl_2$ and $FeCl_3$) or sulphates ($FeSO_4$ and $Fe_2(SO_4)_3$). Electrolyte is stored in two tanks and pumped into the cell using a pump on either side.

The transport of ions across the membrane is critical to maintaining charge balance during operation. The oxidation-reduction reactions occur at both electrodes ($Fe^{2+}/Fe^{3+}$ at the positive electrode and $Fe^{3+}/Fe^{2+}$ at the negative electrode), and the resulting ionic imbalance is neutralized by protons ($H^+$) which act as charge carriers across the membrane, moving to balance the charge at

both electrodes. In addition, chloride ($Cl^-$) or sulfate ($SO_4^{2-}$) ions if the electrolyte contains chloride or sulfate ions also move across the membrane. These ions are transported by diffusion, where ions move from the higher concentration of ions on one side to the other to achieve equilibrium. Ions are also transported by migration where an electric potential difference is produced due to oxidation-reduction reactions, cations (such as $H^+$) move towards the negative electrode, and anions (such as $Cl^-$ or $SO_4^{2-}$) move towards the positive electrode.

In the All-Fe RFB, the membrane selectively allows the passage of (H+, $Cl^-$, $SO_4^{2-}$) which balances the charge without allowing significant crossover of iron ions. The membrane's selectivity is crucial to prevent $Fe^{2+}$ and $Fe^{3+}$ ions from crossing, as their crossover would lead to reduce coulombic efficiency of all iron RFB.

The charging reactions for the Fe-RFB are:

$$Fe^{2+} + 2e^- \rightarrow Fe^0 \quad \text{(Anode).} \qquad (1.9)$$

$$Fe^{2+} \rightarrow Fe^{3+} + e^- \quad \text{(Cathode).} \qquad (1.10)$$

While the discharging reactions are:

$$Fe^0 \rightarrow Fe^{2+} + 2e^- \qquad E^0 = -0.44\ V \text{ (Anode).} \qquad (1.11)$$

$$Fe^{3+} + e^- \rightarrow Fe^{2+} \qquad E^0 = +0.77\ V \text{ (Cathode).} \qquad (1.12)$$

During discharge, $Fe^0$ is oxidized to $Fe^{2+}$ at the anode, releasing electrons. These electrons travel through the external circuit to the cathode, where $Fe^{3+}$ is reduced to $Fe^{2+}$ by accepting electrons.

The overall cell potential for the all Fe-RFB can be calculated from the standard electrode potentials of the anode and cathode reactions during discharge (equation 1.3):

$$E^0_{cell} = (0.77) - (-0.44)$$

$$E^0_{cell} = +1.21\ V$$

The standard potential ($E^0$) of a redox reaction also can be calculated using the standard Gibbs free energies of formation for the reactants and products, along with the electron stoichiometry of the reaction.

the standard Gibbs free energy change for the reaction, $\Delta G^0$, is:

$$\Delta G^0 = \sum \Delta G^0_{Products} - \sum \Delta G^0_{Reactans} \qquad (1.13)$$

the standard Gibbs free energy change for the reaction in equation (1.11) is:

$$\Delta G^0 = (\Delta G^0 \text{of } \mathrm{Fe}^{2+}) - (\Delta G^0 \text{of } \mathrm{Fe}^0)$$
$$\Delta G^0 = (-78.9) - (0) = -78.9 \text{ kJ/mol}$$

the standard Gibbs free energy change for the reaction in equation (1.12) is:

$$\Delta G^0 = (\Delta G^0 \text{of } \mathrm{Fe}^{2+}) - (\Delta G^0 \text{of } \mathrm{Fe}^{3+})$$
$$\Delta G^0 = (-78.9) - (-4.7) = -74.2 \text{ kJ/mol}$$

The standard potential $E^0$ is related to $\Delta G^0$ by the equation (1.14):

$$E^0 = -\frac{\Delta G^0}{nF} \qquad (1.14)$$

where:

$\Delta G^0$ is the Gibbs free energy change,

n is the number of electrons transferred,

F is the Faraday constant (F=96485 C/mol).

For the $Fe/Fe^{2+}$ Reaction:

$\Delta G^0$ = −78.9 kJ/mol = -78900 J/mol , n = 2

$$E^0 = -\frac{-78900}{2\ x\ 96485} = -0.41 \text{ V}$$

For the $Fe^{3+}/Fe^{2+}$ Reaction:

$\Delta G^0$ = −74.2 kJ/mol = -74200 J/mol , n = 1

$$E^0 = -\frac{-74200}{1\ x\ 96485} = -0.77 \text{ V}$$

In electrochemical cells, the Nernst potential can be used to calculate the potential of a half-cell or a full cell when the concentrations are not at standard conditions.

$$E = E^0 - \frac{RT}{nF}\ ln\frac{[Products]}{[Reactants]} \qquad (1.15)$$

where:

- $E$ is the cell potential under non-standard conditions,
- $E^0$ is the standard cell potential (measured at standard conditions: 1 M concentrations, 1 atm., and 25 °C or 298 K),

- R is the gas constant (R=8.314 $J \cdot K^{-1} \cdot mol^{-1}$)
- T is the temperature in Kelvin,
- n is the number of moles of electrons transferred in the redox reaction,
- F is the Faraday constant (F≈96485 C/mol),
- [Products]/[Reactants] is the reaction quotient, Q, representing the concentrations (or partial pressures) of the products and reactants.

At 25 °C, the equation (1.15) simplifies to:

$$E = E^0 - \frac{0.0591}{n} \, log \frac{[Products]}{[Reactants]} \qquad (1.16)$$

where 0.0591 is the approximate value of RT/F when T=298 K.

Overpotential is the additional potential beyond the thermodynamic equilibrium potential that is required to drive an electrochemical reaction at a measurable rate.

The Tafel slope is an important parameter in electrochemical kinetics that provides information about the rate-determining step of an electrochemical reaction. The Tafel slope is derived from the Tafel equation, which describes the relationship between the overpotential (η) and the current density (j). The rate-determining step of the reaction can significantly influence the experimentally determined Tafel slope, as different mechanisms and steps can result in different slopes.

The general form of the Tafel equation (1.17) is:

$$\eta = a + \mathrm{b} \log \mathrm{j} \qquad (1.17)$$

where:

η is the overpotential (the potential difference between the actual electrode potential and the equilibrium potential),

a is a constant,

b is the Tafel slope, given by:

$$\mathrm{b} = \frac{2.303 \, \mathrm{RT}}{\alpha \mathrm{nF}} \qquad (1.18)$$

R is the gas constant (8.314 J/(mol.K)

T is the temperature in Kelvin,

α is the charge-transfer coefficient (a dimensionless factor related to the symmetry of the energy barrier for the reaction),
n is the number of electrons involved in the rate-determining step,
F is Faraday's constant (96,485 C/mol).

The Tafel slope provides information about the mechanism of the electrochemical reaction:
If a single-electron transfer is the rate-determining step with a charge-transfer coefficient α=0.5 , the Tafel slope can be calculated as: b ≈118 mV/decade
If the rate-determining step involves multiple electrons (e.g., n=2), the Tafel slope decreases. For instance, if two electrons are transferred and α=0.5, the Tafel slope would be around 59 mV/decade.

The experimentally determined Tafel slope (b) depends on the rate-determining step of the electrochemical reaction. Different rate-determining steps will yield different Tafel slopes due to variations in the charge-transfer coefficient ($\alpha$) and the number of electrons ($n$) involved. By analyzing the Tafel slope, it can be inferring details about the reaction mechanism, such as the number of electrons involved in the rate-determining step and the nature of the reaction pathway. For example, lower Tafel slopes generally indicate a faster reaction at lower overpotentials, which is desirable in batteries.

Despite the many advantages of this battery that we discussed earlier, there are also some disadvantages, including:
1. The amount of energy stored by a redox flow battery usually depends on the capacity of the electrolyte (its concentration and volume). However, for the Fe-RFB capacity is limited by the size of the deposited Fe layer on the anode, and thus the energy capacity cannot be separated from the size of the deposited layer.

The capacity $Q$ (in ampere-hours) of an All-Fe RFB is given by equation (1.19):

$$Q = n \cdot F \cdot C \cdot V \qquad (1.19)$$

where:

- $n$ is the number of electrons transferred per iron redox reaction.
  For an All-Fe RFB, n=1 for the $Fe^{2+}/Fe^{3+}$ and $Fe^{2+}/Fe^{0}$ reactions.

- $F$ is Faraday's constant, approximately 96,485 C/mol, which converts moles of electrons to coulombs.
- $C$ is the concentration of iron ions ($Fe^{2+}$ or $Fe^{3+}$) in the electrolyte, in mol/L.
- $V$ is the total volume of the electrolyte, in liters (L).

2. The formation of hydrogen gas on the anode during the charging process reduces coulombic efficiency (CE).The typical pH of Fe-RFB is neutral .
3. The precipitation of $Fe(OH)_2$ (rust) occurs when the pH value is high, resulting in cell damage. The hydrogen evolution reaction during RFB charging increases the pH of the electrolyte by generating hydroxide ions. This high pH can cause $Fe(OH)_2$ precipitation based on the following reaction:

$$Fe^{2+} + 2OH^- \rightarrow Fe(OH)_2 \qquad (1.20)$$

This damages the battery by blocking the flow channels and deteriorating the cell components.
4. Lack of stability of the Fe electrode to corrosion in aqueous solution.
5. Slow kinetics for the $Fe^{2+}/Fe^0$ plating and stripping reaction leading to decreased CE.
6. The need to maintain a lower concentration of Fe concentration in the electrolyte to prevent saturation and precipitation.

The concentration of $Fe^{2+}$ in the electrolyte can reach significant levels, especially after all $Fe^0$ (metallic iron) is removed from the electrode surface during charging, where $Fe^0$ at the negative electrode is oxidized to $Fe^{2+}$, which dissolves in the electrolyte.

The concentration of $Fe^{2+}$ is limited by factors such as solubility, diffusion, and the static electrolyte. Through diffusion, Fe(II) ions move from the region of higher concentration (near the electrode) to regions of lower concentration (the bulk electrolyte).

Also, in a static electrolyte (without agitation or flow), $Fe^{2+}$ can accumulate near the electrode if it exceeds its solubility limit, reaching saturation and causing precipitation, which affects the performance of the battery.

For optimal battery operation, the concentration of $Fe^{2+}$ must be kept below the solubility limit to avoid precipitation. This can be achieved by using larger electrolyte volumes.

The diffusion and dissolution rate is also improved by moving the electrolyte as a uniform concentration of $Fe^{2+}$ is maintained, allowing for more stable battery performance.

Savinell and his colleagues[14] (1981) created the first iron RFB with the ability to store and discharge energy with a current efficiency of 90% and an energy efficiency of 50% at a temperature of ~60$^{o}$C and using a porous separator. Savinell 's team worked to improve the performance of the cells and study the factors affecting this. $FeCl_2$ and $FeCl_3$ aqueous were used as battery electrolytes. They tried to control several factors to raise the low cell potential and operate it at high potential. An important factor is minimising electrolyte resistance by choosing an appropriate concentration and adjusting the pH.The potential drop in an electrolyte is typically calculated using Ohm’s law. To control the acidity, ammonium chloride was added to overcome parasitic reactions like hydrogen evolution and hydroxide formation.

Graphite or titanium was chosen as a non-reactive material to be coated with iron as the anode. In order to control the CE of the battery, the reactions at the iron plate at the negative electrode must be controlled, such as its oxidation by the ferric ion that could crossover from the cathode side. For this reason, a separator membrane with fine permeability was chosen to prevent the ferric species accumulating in the anode side of the cell. The pH must be adjusted upwards (to about 3) to reduce the rate of anode corrosion and prevent oxide formation, as well as to reduce the rate of hydrogen evolution, as the potential at which hydrogen evolution occurs shifts to more negative potentials, reducing the likelihood of it occurring within the operating potential window of the battery. It was found that ionic additives have an effective role in reducing corrosion. It was found that adding magnesium maintains the pH stability of the electrolyte, which leads to improved cell performance, and therefore there is no need to add any acid.

Pourbaix diagrams (also called potential-pH diagrams) are graphical representations that show the stable phases of an element as a function of the pH and the electrochemical potential of a solution[15]. these diagrams are especially useful for understanding the stability of metal ions in aqueous environments, which is valuable in corrosion studies, electrochemistry.

The vertical axis is the electrode potential, while the pH of the solution is the horizontal axis. The diagram is divided into regions that show where different chemical species (e.g., solid, ionic, or dissolved) are stable.
Horizontal lines represent reactions that depend only on voltage. Vertical lines indicate reactions that depend only on pH. Diagonal lines indicate reactions that are affected by pH and potential.

Pourbaix diagrams help identify conditions where metals might corrode (where the metal ion form is stable) or passivate (where a protective oxide layer is stable).

For example, the diagram (fig. 1.3 ) illustrates the regions of equilibrium states of iron. In the Fe zone (immune zone), electrochemical reactions take place in the direction of $Fe^{2+}$ ion reduction, and corrosion does not take place in this region.
It is in ($Fe^{2+}$, $Fe^{3+}$, and $FeO_4^{2-}$) zones that metallic iron is oxidized and is referred to as corrosion zones. There is an area ($Fe_3O_4$ and $Fe_2O_3$) in which iron oxidizes (corrodes), leading to the formation of an oxide layer that prevents corrosion (the passivation zone). The $Fe(OH)_2$ region is also a passivation zone, which forms green rust.

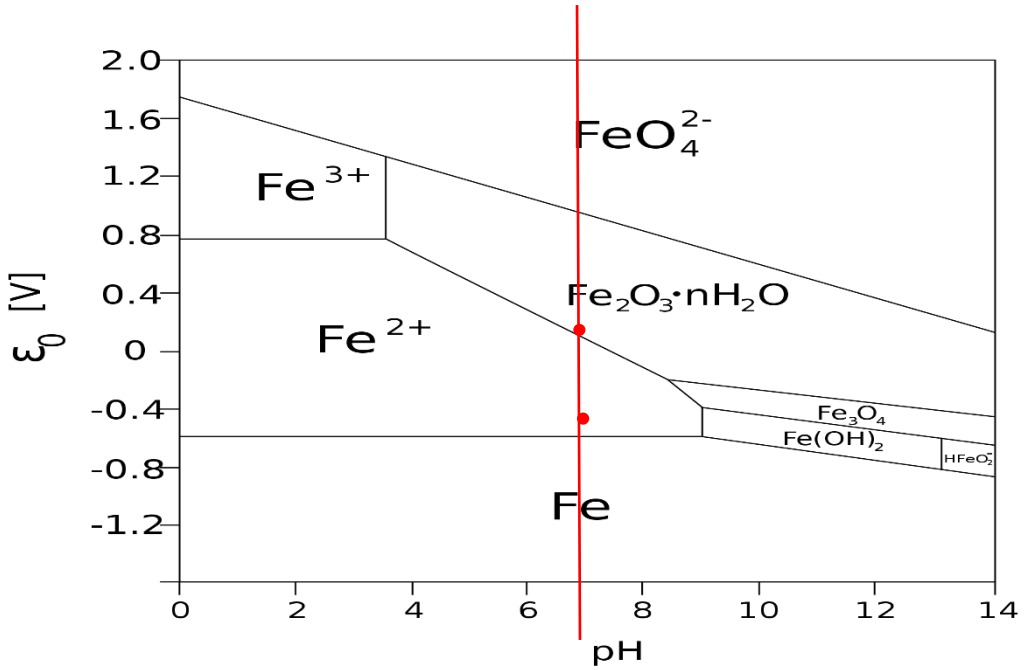


**Figure 1.3** Pourbaix diagram of iron, adapted from Ref[15]
Red line shows the pH value for $Li_2SO_4$ electrolyte.
Dots show the range of potentials used in CVs.

A limitation of the use of Pourbaix diagrams is that they do not typically include minor species like dissolved oxygen ($O_2$ aq)) or carbon dioxide ($CO_2$ aq)), which are often present in small quantities but can strongly impact electrochemical processes. For example, dissolved $O_2$ can act as an oxidizing agent, affecting corrosion rates but not represented in the basic Pourbaix diagram.

Standard Pourbaix diagrams are also constructed at a set temperature (often 25°C) and 1 atm pressure. Different conditions can shift the stability regions, especially for reactions involving gases like $H_2$ or $O_2$.
In summary, Pourbaix diagrams are powerful tools for predicting the stability of chemical species based on potential and pH. However, they must be used cautiously in complex systems, where kinetic factors, impurities, and environmental conditions could significantly alter the predicted outcomes.

The pH of the electrolyte in an all-Fe RFB is a critical factor affecting battery performance, efficiency, and stability. Iron ions are sensitive to pH, with higher pH leading to precipitation of iron compounds, while lower pH can affect redox chemistry and corrosion of cell components.

All-iron redox flow batteries typically operate in an acidic electrolyte, with pH typically ranging from about 1 to 3.

As we can see from the Pourbaix diagram above, acidic conditions are necessary to maintain the solubility of $Fe^{2+}$ and $Fe^{3+}$ ions in solution. At low pH, $Fe^{2+}$ and $Fe^{3+}$ remain stable in the electrolyte without precipitating as insoluble hydroxides at pH above 3. Such precipitates reduce the amount of active iron ions in solution, reducing battery capacity and efficiency.

Acidic conditions also affect the stability of electrodes and other cell components. Although mild acidity supports the dissolution of iron ions, a pH that is too low (e.g., below 1) can increase corrosion rates on components such as current collectors and flow plates, potentially reducing battery life.

Regular monitoring of pH can be essential for long-term battery operation, as side reactions or impurities can cause gradual changes in pH. It is therefore sometimes necessary to add acids such as sulfuric acid ($H_2SO_4$) or hydrochloric acid (HCl) to the electrolyte to maintain an optimal pH.

In this study, $NaHSO_4$ was added to different concentrations of $Li_2SO_4$ and the pH changed from 6.8 to 4.3, but the CV scan shape did not differ as much when acid was added and when it was not added. Therefore, the effect of acid addition on different concentrations of lithium sulfate was not studied.

Passivation is a phenomenon in which a protective layer forms on the surface of the electrode, preventing further reactions. In iron-based systems, passivation can occur when a layer of iron oxide or iron hydroxide forms on the iron electrode, preventing the efficient redox cycle of $Fe^{2+}/Fe^{0}$ and increasing resistance.

Chloride ions help prevent passivation by forming soluble complexes with $Fe^{2+}$ such as $FeCl^{+}$, $FeCl_2$, or $FeCl_3^{-}$ depending on the chloride concentration and pH of the solution. These complexes hinder the formation of iron oxides or iron hydroxides that can block the electrode surface. Thus keeping the iron surface active for redox reactions and increasing battery efficiency.

A number of recent studies have focused on demonstrating the advantages of the Fe-RFB and improving its performance by focusing on the anodic or cathodic reaction or the electrolytes used or one of the components of the cell, as discussed further below.

### 1.3.1. Anode studies

Anode studies have focussed on improving the efficiency of the Fe deposition and stripping reactions and minimising the side reactions that lead to lower CE. Jiang and Liu[16] conducted a comprehensive review of previous research related to charge storage in the anode. Future ideas that contribute to developing the anode mechanism in new iron batteries were summarized. Increased utilization of Fe oxides and sulphides has been urged because it has a significant impact on increasing the energy density of batteries due to the large number of electrons that will participate in oxidation and reduction reactions. The attempt to recover spent anode electrodes are considered among the most important ideas working on anode development in the future.

Balakrishnan and others[17] studied the causes of low charging efficiency of the negative electrode and poor cell performance in all Fe-RFB containing $Fe/Fe^{2+}$ and $Fe^{3+}/Fe^{2+}$ redox couples. 0.03 M $Zn^{2+}$ were added to the anolyte and it was found that zinc ions inhibit the evolution of hydrogen at the anode by forming a $Zn(OH)_2$ compound as a layer deposited on the anode. As a result, the CE increases, and the overall battery performance improves.

The possibility of increasing the efficiency of the Fe-RFB anode reaction was studied by adding ascorbic acid to the electrolyte[18]. Ascorbic acid was adsorbed on the anode surface at pH = 0. This inhibited the hydrogen evolution at the anode, which increased the CE. Also, at pH = 3, this acid changes the iron precipitation mechanism at the anode, where ascorbic acid forms ferrous ascorbate complexes as a layer on the electrode. It also works to shift the equilibrium potential of the anode to more negative values. The positive effect of increasing temperature on efficiency was also studied.

Some factors that affect the efficiency of iron plating at the negative electrode were studied[19] by adding chloride ions to the anode electrolyte at different concentrations. Through cyclic voltammetry measurements, it was determined that the chloride ion reduces hydrogen evolution and enhances the kinetics of iron plating due to its high ability to adsorption on the surface of the electrode. The effect of chloride-bound cations on the coating layer formed on the electrode was also investigated. Sodium chloride recorded the highest efficiency for iron plating at 97%. The negative effect of adding glycine and glycerol on the plating efficiency at the negative electrode has also been proven.

### 1.3.2. Cathode studies

Cathode studies have largely focussed on improving the sometimes slow kinetics of the $Fe^{2+/3+}$ redox couple by improving the catalytic properties of the cathode material.

A series of electrically spun nanofiber mats of polyacrylonitrile (PAN) precursors have been used as electrodes in an Fe-RFB where they were manufactured and treated with heat and KOH [20]. These nanofibers were used to increase the kinetics of redox reactions ($Fe^{3+}/Fe^{2+}$) and thus improve battery performance. Several properties of these treated nanofibers were examined, including their morphology, porosity, and electrochemical performance using cyclic voltammetry. There was a significant increase in porosity of the mat following treatment. In comparison to another electrically spun nanofiber mat heat-treated only, the heat-and-KOH-treated mat increased the anodic peak current of the $Fe^{3+}/Fe^{2+}$ redox couple by 60% at the same scanning rate. Also, when comparing the heat and KOH treated mats with the commercial carbon electrode, it was found that the mats recorded a significantly higher catalytic activity. Consequently, these mats are considered promising candidates for use as electrodes in Fe-RFB.

Anarghya et al [21] modified the graphite electrode used as a positive electrode (cathode) in the Fe-RFB due to the slow kinetics of the reactions at the positive electrode, which in turn affects the overall performance of the battery.The graphite electrode was modified using nitrogen-saturated carbon particles

derived from Bermuda grass. A variety of characterisation techniques were used, including SEM, EDAX, Raman, and XPS. According to the results, the N-containing electrode had a significant improvement in electrochemical properties when compared with the unmodified electrode, since the peak cathodic and anodic currents recorded higher values and the reaction became more reversible, resulting in a higher level of efficiency. As a result, the coulombic efficiency of the battery is increased to 95%. These positive results are attributed to the catalytic properties of the electrode due to nitrogen incorporation.

Similarly, a graphite electrode has been modified with nanoparticles of $WO_3$, which are electrochemically active materials that serve to enhance electrical activity, kinetics and reversibility of the Fe(II)/Fe(III) couple[22]. With the use of cyclic voltammetry, electrochemical impedance spectroscopy, and dynamic polarization studies (Tafel analysis), it was found that the nano-modified electrodes were highly effective towards the redox reaction Fe(III)/Fe(II). Using these electrodes as a cathode, the CE of the whole redox flow cell increased to 60%, which is higher than the results obtained for the electrode without modification (18%).

By using graphene oxide (GO) modified graphite felt as a positive electrode, the performance of the Fe-RFB was enhanced [23]. Electrostatic spraying was used to apply a layer of GO to the graphite felt. GO was selected due to its excellent electrochemical properties as it provides a large surface area and effective reactive sites that increase the catalytic activity. The results revealed that the GO-modified electrode performed better than the unmodified carbon felt, due to the catalytic effect of the conducting network of defective edges of oxygen on the surface of the layered flakes of the GO.

Sawant and McKone [24] conducted a study on the redox chemistry of $Fe^{3+/2+}$ using rotating-disk electrode voltammetry to investigate the kinetics and mechanisms of redox reactions. It provides several key benefits due to its ability to control mass transport effectively. They used polycrystalline Pt and Au working electrodes as a model. When the Fe solution species concentration was increased by a factor of 100, the exchange current densities at Pt only increased by approximately 15-fold. This indicates that the reaction is not solely dependent

on the Fe concentration, or that the main mechanism changes as the electrolyte concentration increases. Thus this study shows that even the mechanism of a simple and well established redox reaction may be more complex and requires further research to understand.

### 1.3.3. Role of electrolyte

Electrolyte studies fall into two categories: investigating the effect of changing electrolyte properties, such as concentration, other ions present and addition of other additives, or investigating the effect of changing or modifying the Fe redox species.

The effect of adding 1-ethyl-3-methylimidazolium chloride (EMIC) to a high concentration of $FeSO_4$ electrolyte was investigated by Yu and others [13] The CV technique was used to determine the rates and efficiency of the plating and stripping of iron, to provide insights into the strength of the interaction between Fe ions and water. This paper shows that the solubility of $FeSO_4$ was improved by addition of EMIC.

The effect of adding hydrochloric acid to the iron chloride electrolyte in a RFB was studied by Furquan and others [25]. The use of hydrochloric acid enhances the CE of the battery, partly by increasing the solubility and stability of the $FeCl_2$ redox species. After 150 cycles, the discharge capacity reached a constant level of 98% and the CE was 99%. Without the addition of acid to the electrolyte, the capacity retention is approximately 73%, and the CE is around 74%. Through the utilisation of 3D X-ray tomography and field emission scanning electron microscopes (FE-SEM), it was demonstrated that the addition of acid to the electrolyte increased reversibility of the iron deposition process at the cathode. Furthermore, it affects the battery's recycling lifespan.

Changing the Fe electrolyte species has also been demonstrated to be advantageous. An all-iron alkaline flow battery has been developed by coupling iron/ferrous gluconate complexes with $[Fe(CN)_6]^{3-}/[Fe(CN)_6]^{4-}$ [26]. Cyclic voltammetry results showed the battery demonstrated outstanding long-term energy storage performance and reached a CE of over 99%. Shroder aimed to improve the redox reaction by adding organic ligands to create complexes like iron(III)-N,N’-ethylene-bis-(o-hydroxyphenyl glycine), initially improving

performance by minimizing hydrogen evolution. Nevertheless, as time passes, these compounds deteriorate, resulting in a decline in the battery's capacity. Complexes formed by ferrocene and glycerol compounds have been utilised in batteries, albeit they require additional enhancement. Liu decreased the resistance of the electrolyte in charge transfer by creating gluconate complexes with iron. On the other hand, Kwon employed Fe(BIS-TRIS) and ferrocyanide as redox couples to enhance the battery's efficiency. However, over time, this had an impact on the redox reactions due to their passage through the membrane.

Shin et al [27] investigated the stability of all-iron aqueous RFB that utilise Fe[DIPSO] and ferrocyanide as the redox couples. The investigation focused on examining the stability of ferrocyanide under different pH conditions as its degradation had been reported under high pH conditions. A further problem is the imbalanced pH impacts in both the catholyte and anolyte electrolytes, due to water molecules crossing the membrane between the two half-cells. When the pH and concentration parameters of the catholyte and anolyte are carefully optimised, the capacity of the RFB is effectively maintained during the entire cycling process. After implementing the optimised electrolyte condition, the device's performance remains consistently high for a duration of 23 days, ensuring its long-term stability. These findings demonstrate that the stability of the RFB can be improved by manipulating the pH and concentration of its electrolytes.

## 1.4 Electrolytes

As this thesis concerns the influence of electrolyte composition on the redox reactions of Fe, this section gives a brief overview of the definitions of different types of electrolytes.

### 1.4.1. Definitions of electrolytes

Electrolyte salts are compounds that exhibit inherent positive or negative electrical charges when they are dissolved in water [28]. Electrolyte solutions can be categorised into many classifications, such as dilute electrolytes and concentrated electrolytes. A dilute electrolyte refers to a solution with a comparatively low concentration of dissolved ions. In this particular solution, the

ions are adequately spaced apart, resulting in little interactions between them. Studying dilute electrolytes is generally simpler because the ions exhibit greater independence in their behaviour. The occurrence of interactions such as ionic pairing or aggregation is minimal. Consequently, the properties may be accurately predicted using straightforward models such the Debye-Hückel theory [29]. Electrolytes of concentration in the mM range can be classed as dilute electrolytes (for a 1:1 electrolyte).

A concentrated electrolyte is a solution with a relatively high concentration of dissolved ions (greater than mM concentration). In this particular solution, the ions are densely arranged, resulting in substantial interactions between them, such as ionic pairing and aggregation, which causes their behaviour to deviate from the ideal state. Their conductivity is often high because of the abundance of ions available to transport the current. However, at very high concentrations, the presence of ionic pairing or aggregation can cause the conductivity to stabilise or even decrease [29].

Water-in-salt electrolytes (WiSE) are a novel type of electrolytes that have extremely high concentrations of salt in water, exceeding the solubility limits of traditional aqueous electrolytes. The definition of a WiSE is electrolytes in which the salt concentration in water is so high that the salt exceeds the number of aqueous solvent molecules in the system in terms of weight and volume and all water molecules are coordinated with metal cations[30]. These electrolytes have distinctive characteristics, such as improved electrochemical stability, high ionic conductivity, and the capability to function across a broader voltage range, making them highly appealing for energy storage systems. These electrolytes are not well understood due to their high concentration when compared to more dilute electrolyte solutions. Hence, additional investigation and experimentation are required [31].

Measuring the characteristics of electrolytes is essential for determining their appropriateness for different uses, particularly in energy storage systems such as batteries, supercapacitors, and fuel cells. Important characteristics to assess are conductivity, viscosity, and solvation structure. The details of these are elaborated on in Chapter 3.

### 1.4.2. Studies using very concentrated electrolytes and WiSE

Recently Dryfe and co-workers[32] have carried out in depth studies of aqueous solutions of alkali metal halides using KF electrolytes, with concentrations ranging from 0.5 M to 17 M, similar concentrations of LiTFSi used for our studies described in Chapter 6 of this thesis. The properties of the prepared KF electrolytes was studied by using $K_3Fe(CN)_6$ (10 mM) as a dissolved redox species. In the KF electrolytes, the redox chemistry of $K_3Fe(CN)_6$ displays broad oxidation and reduction peaks with a wide peak-to-peak separation that ranges between 220 and 292.5 mV depending on scan rate. They have observed the kinetics of electron transfer are slow when using 0.5 M KF and the kinetics increased as the concentration of KF increased to 5.0 M, suggesting the kinetics of electron transfer processes is heavily dependent on concentration of the electrolytes. Further, another important feature they observed is the CV of the $K_3Fe(CN)_6$ became more reversible when the concentration of the electrolyte has increased to almost 10 M, which is roughly a WiSE and has shown 81 mV for most of the scan rates used. However, the observed peak separation for this reaction is still higher than the ideal value of 59 mV, expected for an electrochemical reversible one electron transfer process.

To further understand the electrochemical properties of these electrolytes, the diffusion coefficient (D) of the $K_3Fe(CN)_6$ was determined. It was observed that the calculated D from the Cottrell equation is in reasonable agreement with the D from analysis of the CV data via the Randles–Sevcik equation. For the lower electrolyte concentrations i.e., from 0.5 to 5.0 M, the calculated diffusion coefficients of $K_3Fe(CN)_6$ from both methods is $2.49 \times 10^{-6}$ $cm^2$ $s^{-1}$, which is in reasonable agreement with the other dilute aqueous solution[33].However, as the electrolyte concentration increased to 10 M which is ideally a WiSE system, there is a decrease in the diffusion coefficient of $K_3Fe(CN)_6$ to $1.94 \times 10^{-7}$ $cm^2$ $s^{-1}$ and decreased further to $1.24 \times 10^{-8}$ $cm^2$ $s^{-1}$ when the KF concentration was increased to 17 M. Interestingly, the decreased diffusion coefficient are similar to those of electroactive solutes dissolved in ionic liquids at room temperature, showing the high viscosity of these WiSE.

The higher salt concentration decreases the diffusivity of the water because a higher proportion of solvent is incorporated into the hydration shell, and it was also hypothesized that the ion transport is decreased due to enhanced ion paring effects at higher concentration[34]. The higher sensitivity of the solute diffusion coefficient observed from KF indicates that a more complex process is inhibiting the flux of the solute and there is potentially higher ion pairing of the ferricyanide due its high charge, and the complex ion-paired structure is responsible for transport to the electrode at high KF concentrations. It was found that the at higher concentrations of KF such as 17 M there is an increased the electrochemical potential window and another notable feature is that it reduces the oxygen transport properties in the electrolyte, which further inhibits the oxygen reduction at cathode.

There have been a number of papers in recent years concerning the structure and properties of the LiTFSI WiSE. Replacement of $Li^+$ with other cations such as $Na^+$ has also been studied, as described below.

Jeon and Cho [35] investigated four main categories of atomic interactions and dynamics involving Li ions, anionic oxygen atoms ($O_T$), and atoms of water molecules ($O_W$) in a LiTFSI WiSE. Molecular dynamics simulation and theoretical analysis were used. The distribution of atomic composition in the first solvation shells of both atoms and water molecules is presented. In addition, the thermodynamic stability of the atom pairs in contact was investigated and their lifetimes were calculated. The results show that lithium ions follow several pathways over a period of less than one millisecond, with distinct solution regions containing high concentrations of water and anions. The ions alternate between a vehicular mechanism and a hopping mechanism, depending on the local solution structure. The stability of the $Li\cdots O_W$ contact pair is relatively higher than that of the $Li\cdots O_T$ contact pair under saturation circumstances. This causes rapid passage of lithium ions through the WiSE.

Borodin et al [36] assessed the ion solvation and transport behaviours in aqueous electrolytes containing LiTFSI using molecular dynamics simulations, small-angle neutron scattering, and several spectroscopy techniques. At salt concentrations

ranging from 10 to 21 mol/kg, they observed that cations became unevenly solvated, resulting in the formation of liquid structures with heterogeneous domains. The presence of nano-heterogeneity in this system efficiently separates cations from the coulombic traps of anions. This creates a three-dimensional percolating network of lithium and water, allowing for the liberation of 40% of the lithium cations. It was proposed that super-concentrated aqueous electrolytes exhibit percolation networks, resulting in a high lithium-transference number. The transference number of an ion in an electrolyte is the fraction of the total current carried by that specific ion. In normal electrolytes, the transport number is not 100% because cations and anions have different sizes and charges, which affects their mobility. Since current depends on ion mobility, no single ion typically carries the entire current. The transference number is crucial for understanding ion transport and designing efficient electrolytes for batteries and fuel cells. A balanced transference number ensures optimal ion transport, minimizing issues like concentration polarization.

A non-lithium cosalt was used in a WISE by Chen et al [37] to alter the configuration of the solvation sheath that surrounds lithium ions. The inclusion of ammonium salt ($Me_3EtN{\cdot}TFSI$) in water significantly increases the solubility of LiTFSI, elevates the molar ratio of salt to water from 0.37 to 1.13, and substantially decreases the water activity in both the overall electrolyte and the $Li^+$-solvation sheath. This aqueous electrolyte solution has a total concentration of 63 m and is composed of 42 m of LiTFSI and 21 m of $Me_3EtN{\cdot}TFSI$. It has a wide operating range of 3.25 V showing the low concentration of free water and electrochemical stability of the solution.

A theoretical study was applied on how to change the properties of WISE solutions for Na-ion batteries with different concentrations [38]. Large-scale quantum molecular dynamics simulations were used to analyse both the structural and dynamical properties. Examination of the movement of $Na^+$ ions shows that the exchange of ligands (solvent/anions) is a process that allows $Na^+$ ions to move in concentrated solutions, serving as an alternate pathway for ion diffusion.

## 1.5 RESEARCH AIM:

As described previously, all-iron aqueous RFBs provide a low-cost, safe solution for energy storage, utilizing the Fe(II)/Fe(0) couple at the anode and the Fe(III)/Fe(II) couple at the cathode. While the simplicity of this battery design is attractive, several fundamental challenges must be overcome to allow full exploitation. These include slow kinetics for the $Fe^{2+}/Fe^{0}$ plating and stripping reaction leading to decreased CE and competing $H_2O$ reduction at the Fe electrode leading to harmful $H_2$ generation.

It has therefore been suggested that the use of concentrated electrolytes will reduce electrochemical reduction of water at the electrode. In concentrated electrolytes most of the water is bound to the cation by solvation, so there is little 'free' uncoordinated water available. It is proposed that a lack of 'free' water will prevent or suppress parasitic side reactions ($H_2$ evolution, pH change and Fe corrosion). We therefore expect concentrated electrolytes improve the CE and cycle life of Fe-RFBs.

The aim of this thesis is to determine how the electrolyte concentration affects the anodic reactions of iron. It also aims to determine any advantages or disadvantages in using very concentrated electrolytes in this application. To study this, we need to address the following research questions:

1- How does the electrolyte concentration affect the solution properties?
2- How does electrolyte concentration affect the rate of Fe oxidation?
3- Is there a limit to stability of the reaction in the concentrated electrolytes?

The structure of this thesis is as follows: The literature on Fe-RFB and some background on electrolytes is summarized in Chapter 1. The main techniques (cyclic voltammetry (CV), Raman and infra-red (IR)) and the viscosity, conductivity measurements used in this research are presented in Chapter 2. In the third chapter, the properties of electrolytes are discussed and the viscosity, conductivity and IR results of different concentrations of lithium sulfate solutions are presented. In Chapter 4, the results of electrochemical measurements of an iron electrode immersed in different concentrations of lithium sulfate after applying a potential are presented. CV was used to understand the oxidation

kinetics of an iron electrode immersed in different concentrations of lithium sulfate. Chronoamperometry was also used to understand the process of dissolving iron over time. In addition to the above, Raman spectroscopy measurements were taken at a certain voltage to determine the type of species present on the surface of the electrode after the oxidation process. In the fifth chapter, the results of IR spectroelectrochemistry of the region near the surface of the electrode in a lithium sulfate solution are presented to understand the changes occurring to the electrolyte and water upon dissolution. The first part of Chapter 6 explores the effect of adding magnesium chloride on dissolution of iron in different concentrations of lithium sulfate. In the second part of Chapter 6, all previous techniques were used to study the water in salt electrolyte (LiTFSI) and then a comparison was made between the results of using LiTFSI and the results of using lithium sulfate on iron dissolution. In Chapter 7 , the overall conclusion for this thesis .

The electrolyte under study in this thesis is $Li_2SO_4$ at concentrations of 0.1 - 2.5 M. The rationale for the choice of $Li_2SO_4$ is firstly that it is a sulfate salt, and iron sulphate is preferred over chloride in Fe-RFB application as being more environmentally acceptable. In this study we add no additional Fe species (e.g. $FeSO_4$) but instead will oxidise Fe metal electrochemically to produce dissolved $Fe^{2+}$. As it is known that $FeSO_4$ has relatively good solubility the use of the sulfate anion in the electrolyte should not interfere with this dissolution process. Out of the alkali metal sulfates, Li sulphate shows higher solubility (up to 2.5 M) compared to Na and K sulfate (solubility 1 M) allowing a larger range of concentrations to be investigated. Moreover, as we briefly compare with use of the water in salt electrolyte LiTFSI, the use of $Li_2SO_4$ acts as a useful baseline study. The other motivation for using a sulfate salt is that the anion is IR active meaning that it is an excellent probe for the IR spectroelectrochemical studies discussed here.

# CHAPTER 2

# METHODOLOGY

## 2.1 Measurements of the transport properties of electrolytes

The properties of the electrolyte play an important role in determining its behavior in a wide range of applications. This section describes some important measurement techniques for determining the transport properties of electrolytes.

### 2.1.1 Electrolytes

Solutions of $Li_2SO_4$ (Sigma Aldrich) were made up in 18 MΩc m deionized water at concentrations ranging from 0.1 – 2.5 mol $dm^{-3}$ (M). We first determined that there is no significant difference between the molarity (M) and molality (m) of $Li_2SO_4$.For example, a solution with molality of 0.1 m $Li_2SO_4$ in 50 g water was prepared. The volume of the total solution was measured after dissolving and was found to not exceed 50 ml. It is the same as the volume of the solution if the molarity was prepared in a volumetric flask 50 ml. This was found to be the case for even the higher molality solutions prepared, so solution molarity (concentration) is reported throughout this thesis.

LiTFSI (Sigma Aldrich) solutions were prepared in 18 MΩ cm of deionized water at concentrations of (0.1 - 1-5 -10 -15 molal) while $MgCl_2$ (Sigma Aldrich) was prepared at concentrations of 4.5 M.

### 2.1.2 Conductivity measurements

Conductivity measurements are a measure of how well a material can conduct electrical current[39]. The current in solution flows due to the migration of ions through the solution when a potential difference is applied. The main electrical property of a solution is its resistance, R, which is expressed in ohms (Ω). Conductance, G, is the inverse of resistance: $G = 1/R$, and is therefore expressed as $\Omega^{-1}$. Conductance of a given solution sample is dependent on its volume, hence experimentally the conductivity ($\kappa$, units Siemens per meter (S $m^{-1}$)) is usually determined, as it allows for normalization with respect to area ($A$) and length ($l$):

$$G = \kappa A \,/\, l. \qquad (2.1)$$

For an electrolyte solution, the ionic conductivity depends on the concentration of ions in the sample, so it is expressed as the molar conductivity, $\Lambda_m$, which is defined for an ideal solution as $\Lambda_m = \kappa/c$ where $c$ is the molar concentration of the added electrolyte. The units of molar conductivity are Siemens square meters per mole ($S\,m^2\,mol^{-1}$). For a fully dissociated electrolyte it is expected therefore that $\kappa$ is proportional to stoichiometric concentration, however this relationship does not hold. Instead, it is found that molar conductivity tends to decrease as concentration increases due to electrostatic interactions between the ions. The presence of oppositely charged ions in solution has the effect of slowing down the migration of ions in response to an electric field and hence the molar conductivity is not independent of concentration[39].

Kohlrausch's law shows that at low concentrations the molar conductivity of the strong electrolyte depends on the square root of the concentration

$$\Lambda_m = \Lambda_m^o - Kc^{1/2} \qquad (2.2)$$

Where $\Lambda_m^o$ is the limiting molar conductivity. This law is only valid up to about 1 x $10^{-3}$ mol $dm^{-3}$ due to the approximations made in the derivation. At higher concentrations ion pairing (as described above) can also play a role as the concentration of ions that are free to move is smaller than the stoichiometric concentration[39].

The electrical conductivity of $Li_2SO_4$ electrolyte at different concentrations was measured using a CDM230 Conductivity Meter with a traditional two-pole cell, where an alternating current is applied between the two electrodes and the resulting voltage is measured and then the resistance of the solution is determined. The standard solution used for calibration in this experiment was 0.1 M KCl and the temperature was 25°C.

### 2.1.3 Viscosity measurements

Viscosity is a measure of a fluid's resistance to flow, and it can be influenced by factors such as concentration, temperature, and the nature of ions in the solution. For higher ionic concentrations where viscosity plays a role, the equation used to describe these relationships is the Stokes–Einstein equation, which shows the

relationship between diffusivity and viscosity[39].

$$D = \frac{k_B\ T}{6\ \pi\ \eta\ r} \qquad (2.3)$$

Where $k_B$ is Boltzmann constant (1.38x10$^{-23}$ J/K), $T$ is temperature in K (298 K), $r$ is the hydrodynamic radius, $\eta$ is viscosity in Pa s and D is diffusion coefficient in cm$^2$ /s.

There are two important concepts in fluid mechanics that describe the flow behavior of fluids:

1- Dynamic viscosity ($\eta$) is a measure of a fluid's internal resistance to shear or flow. Dynamic viscosity unit is Pa s.
2- Kinematic viscosity ($\nu$) is the ratio of dynamic viscosity to fluid density ($\rho$). Kinematic viscosity units are m$^2$/s.

The relationship between dynamic and kinematic viscosity is given by: $\mu = \nu \cdot \rho$

The viscosity of the $Li_2SO_4$ electrolyte prepared was studied by adding 1 mM $K_4Fe(CN)_6$ for each of the different $Li_2SO_4$ concentrations and carrying out cyclic voltammetry (CV) at four scan rates (20, 50,100, 200 mV/s) . The oxidation peak currents of the resulting CV were used to determine the diffusion coefficient D of $Fe(CN)_6^{4-}$ in each solution (see section 3.2.2 for details). The Stokes-Einstein equation(2.3) was then used to determine the viscosity of the solution.

## 2.2 Determination of molecular structure of electrolytes

### 2.2.1 Cyclic voltammetry:

Cyclic voltammetry (CV) is a method in electroanalytical chemistry that can be used to gain information on thermodynamic parameters, such as the redox potential, as well as the kinetics of electrode reactions[40]. In CV, the current is monitored while the potential is swept linearly with time until a switching potential is reached, at which point the sweep is reversed and the potential then returns to its initial value. Figure 2.1 demonstrates that CV necessitates the application of a triangular voltage cycle shape[41]. This entails varying the potential applied to the working electrode within the range of two specific potentials, $E_1$ and $E_2$. Once the potential $E_2$ is attained, the sweeping process is reversed to return to the

initial potential $E_1$, resulting in a potential cycle. In the example shown in figure 1.1, $E_1$ is more positive than $E_2$.

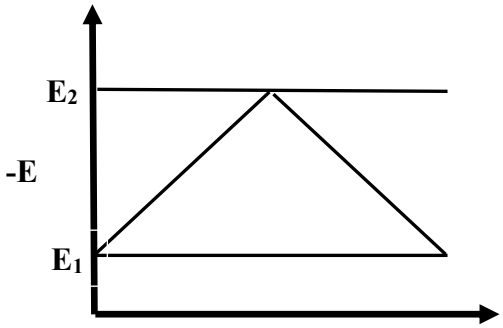


**Figure 2.1** The change of potential with time as a triangular potential cycle, adapted from [41]

Considering the following reversal reaction: $M^+ + e^- \leftrightarrow N$

On sweeping the potential from $E_1$ to $E_2$ (forward scan) the reduction of $M^+$ to N takes place if the reduction potential for the redox couple lies within this potential range. The oxidation process of N, which is formed at the electrode surface during the forward scan, allows reformation of $M^+$ when the voltage is reversed from $E_2$ to $E_1$. A reduction current (by convention negative) is therefore observed during the forward scan and an oxidation current (by convention positive) in the reverse scan. The peaks shown in a CV indicate the locations where the electrochemical reactions, specifically reduction and oxidation, exhibit the highest level of activity. The CV's shape offers valuable information about the kinetics and mechanism of the redox process, including details about reaction reversibility, diffusion coefficients, and the electrochemical behaviour of the species being studied. Figure 2.2 shows the CV for a reversible electron transfer reaction.

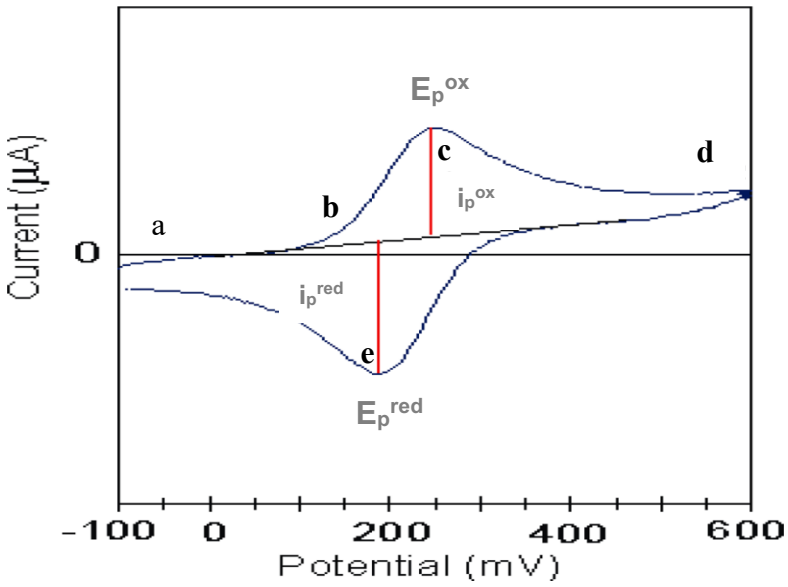


**Figure 2.2** The voltammogram of single electron oxidation-reduction, adapted from [42]

The voltammogram commences at point (a), which represents the potential at which no current is observed, and then the potential is incrementally increased towards more positive potentials. During this occurrence, the potential reaches a specific region (b) when electron transfer from $M^+$ to the electrode takes place, resulting in the production of N. This process is accompanied by the observation of an oxidation current, also known as anodic current. In region (b) the current rises approximately exponentially from zero as the potential increases in the positive direction. The current initially rises because of the large concentration of $M^+$ in the diffusion layer. Additionally, the kinetics of converting $M^+$ to N grow more favourable as the potential gets more positive.

At point (c) the current achieves its peak value, $i_p^{ox}$, accompanied by a matching oxidtion peak potential, ($E_p^{ox}$). At this juncture, the diffusion of new $M^+$ is insufficient to match the rate of electron transfer, resulting in $M^+$ being depleted faster than it can be replenished. Hence, the current observed prior to point (c) is contingent upon the electron transfer rate, whereas the current subsequent to point (c) is constrained by diffusion. Once the voltage reaches point (d), it undergoes a reversal and is then sent back to point (a). When the voltage is reversed, $M^+$ is replenished due to the reduction of N, leading to an reduction current with maximum ($i_p^{red}$). The voltage at point (e) is referred to as the cathodic or reduction peak potential ($E_p^{red}$).

The voltammogram's characteristics depend upon the reversibility of the electrode kinetics of the redox couple. Significant current flows at small overpotentials for reversible couples. At all scan rates at a temperature of 298 K, the forward and reverse current peaks have equal magnitudes and are separated by a potential of 59 mV. This is described by Equation (2.4):

$$\Delta E_p = |E_{pa} - E_{pc}| \approx \frac{2.3\,RT}{\mathrm{n\,F}} \qquad (2.4)$$

The Randles-Ševčík equation is used to define the peak current, $i_p$, which is a crucial aspect of the CV.

$$i_P = 2.69\,x\,10^5 n^{3/2} AC\sqrt{D}\sqrt{\upsilon} \qquad (2.5)$$

Where n is electron stoichiometry, A is electrode area in $cm^2$, C is concentration in $mol/cm^3$, D is diffusion coefficient in $cm^2$ /s and $\upsilon$ is scan rate in V/s.

The CV of a solution species diffusing (as described above and in Chapter 3) will exhibit different characteristics compared to those of a solid/solution reaction (as is the case for the CVs in Chapter 4 and 6 of this thesis) due to inherent disparities in mass transport processes, surface interactions, and reaction kinetics. Mass transfer in solution species is predominantly achieved through diffusion, resulting in the formation of well-defined peaks (symmetrical peaks), due to the influence of the diffusion coefficient. In solid/solution processes, mass transport includes not only diffusion but also the transfer of solid material to or from the electrode surface, which can occur at a slower pace and involve greater complexity. Reactions between solids and solutions frequently result in modifications to the electrode surface, such as the creation of a passivation layer or film. These changes can impact the current response. Furthermore, the peaks will exhibit a wider width and reduced symmetry. The difference in energy between the peaks ($\Delta E_p$) is greater, suggesting a slower rate of reaction.

In a CV experiment, three electrodes form a cell (figure 2.3). In the experiment described in this report the working electrode (WE) usually consists of an iron electrode, which is where the reaction takes place. In Chapter 3 a glassy carbon electrode is used for some experiments to determine viscosity. A platinum counter electrode (CE) completes the circuit, but otherwise no monitoring of the current or the reactions takes place there. In addition, an Ag/AgCl reference

electrode (RE) is used to reference all of the potentials that were measured in this study. In chapters (3 , 4 and 5) $Li_2SO_4$ was used as an electrolyte in electrochemical techniques at different concentrations (0.1, 0.4, 1.0, 1.8, 2.0 , 2.5 M), while in the first part of chapter 6, 4.5 M of magnesium chloride was added to the same concentrations of lithium sulfate. As for the second part of chapter 6 , LiTFSI was used as an electrolyte in electrochemical measurements at different concentrations (0.1, 1.0, 5.0, 10, 15 m).

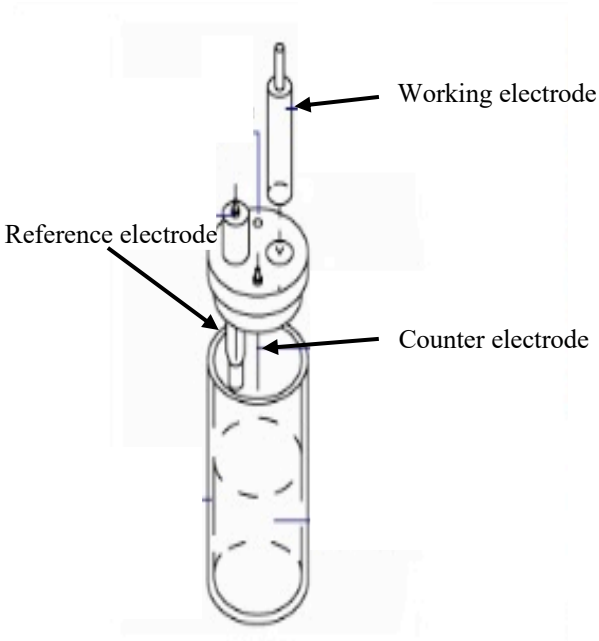


**Figure 2.3**Three electrode cell in cyclic voltammetry[43]

### 2.2.2 Raman spectroscopy:

Raman spectroscopy is widely used to provide information on chemical structures and physical forms and identify substances present from “fingerprint” spectral patterns. The sample can be examined in a wide range of physical states; solid, liquid or gas, in hot or cold state, in bulk as microscopic particles or as surface layer [45].

This type of spectroscopy uses inelastic scattering of photons, known as Raman scattering. It is usually a monochromatic light source such as a laser in the visible, near infrared, or near ultraviolet range. When a laser light interacts with molecular vibrations, phonons, or other excitations in a system, the energy of the laser photons is changed. Information about the vibrational modes of a system can be obtained from the shift in energy [46].

Raman spectroscopy is a similar technique to IR spectroscopy and can be used to determine the structure of water and the ions present in the water. As mentioned before, it is based on inelastic scattering of light, providing information about vibrational and rotational transitions in molecules. The appropriate wavelength must be chosen because it affects the efficiency of dispersion.
Raman spectroscopy can capture stretching and bending vibrations in water molecules.
Similar to infrared spectroscopy, Raman spectroscopy can be used to study the hydration envelopes around ions in water.

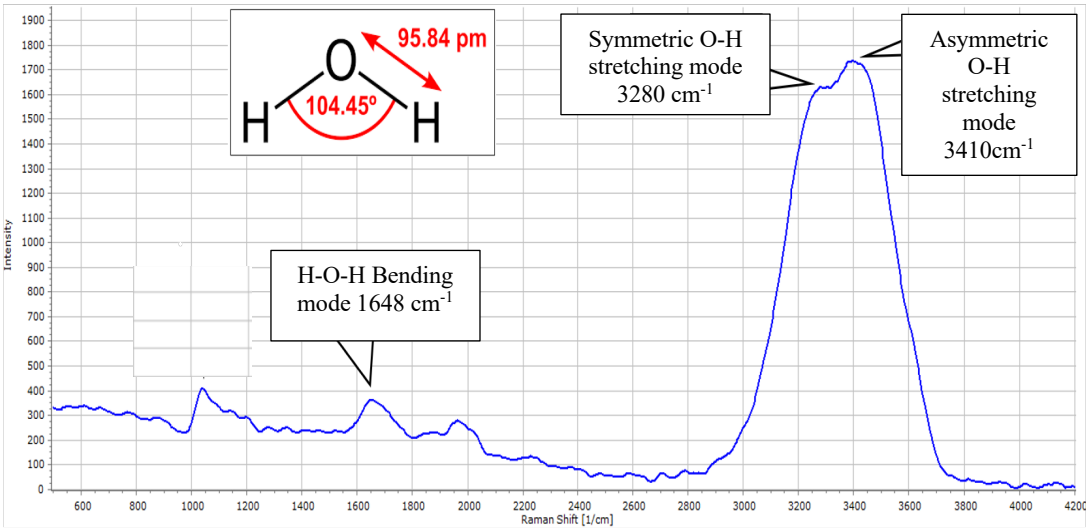


**Figure 2.4** Raman spectrum of water[44]

In figure 2.4, the Raman spectrum shows the vibration bands of water at about 3400 and 3250 $cm^{-1}$, as well as the bending mode at a frequency of about 1650 $cm^{-1}$.

The OH stretch band around 3400 $cm^{-1}$ is often divided into three Gaussian peaks corresponding to hydrogen-bonded water molecules with different donor (D = hydrogen-donating hydrogen bond) and acceptor (A = oxygen-accepting hydrogen bond).

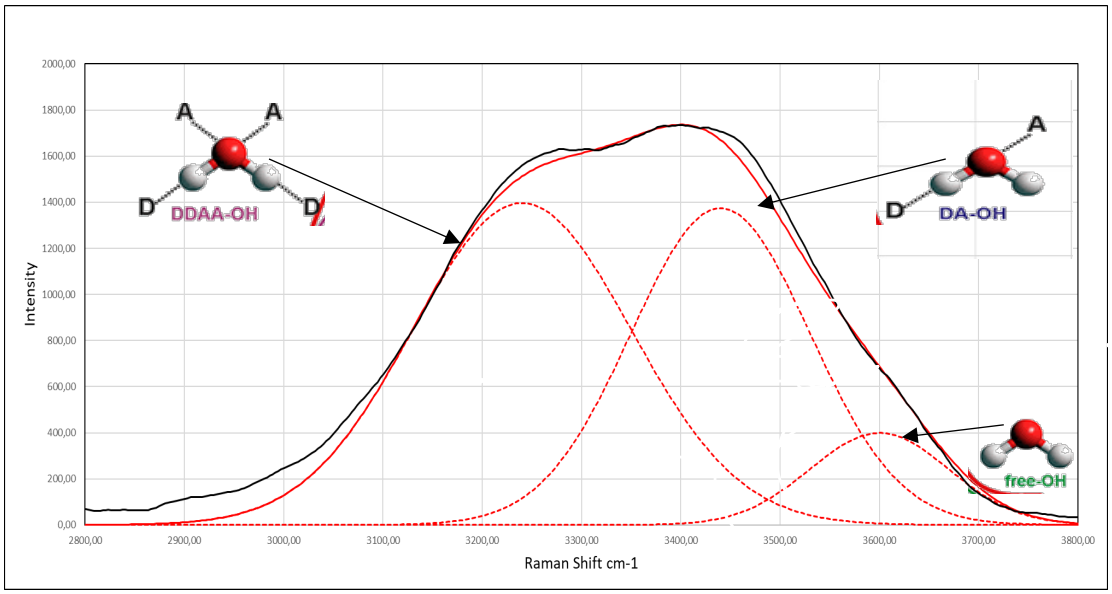


**Figure 2.5** Water O-H stretching band[44]

The three Gaussian curves are shown in figure 2.5, two of which correspond to symmetric and asymmetric vibrations; Another curve centered at higher frequencies is for individually bound $H_2O$ molecules. The two most significant peaks at about 3200 $cm^{-1}$ and 3400 $cm^{-1}$ are most likely due to the predicted greatest DDAA-OH ($H_2O$ with four hydrogen bonds, two donor and two acceptors at about 3200 $cm^{-1}$) and DA-OH ($H_2O$ with two hydrogen bonds, one donor and one acceptor at about 3400 $cm^{-1}$). However, as stated above, some studies believe that treating the water as a 'mixture' of different bonding types is not an accurate representation and that a continuum of behaviours is a better description.

Figure 2.6 illustrates potential transitions that can occur during a single vibration. At 25°C [45], the majority of molecules exist in the lowest vibrational energy state. When photons interact with molecules, the majority of them are elastically scattered, meaning their energy remains unchanged. This phenomenon is known as Rayleigh scattering. During Stokes scattering, photons transfer energy to the molecules, resulting in a decrease in frequency of the emitted radiation. Anti-Stokes scattering refers to the process in which a photon absorbs energy from a molecule, resulting in the emission of radiation with a higher frequency. The Raman shift, which is the difference in energy between the entering and scattered photon, corresponds to the energy difference between the molecule's vibrational energy levels. The identification of the various vibrational modes of a molecule can be accomplished by observing Raman shifts in the spectrum of inelastically scattered light [46],[47].

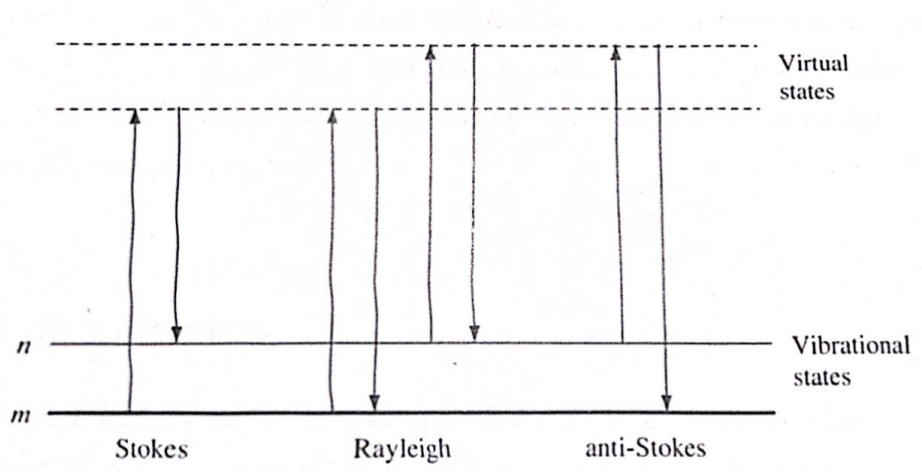


**Figure 2.6** Rayleigh and Raman scattering events with the lowest vibrational energy level,m and excited vibrational energy level, adapted from [45]

A Raman system generally comprises four main components: an excitation source (laser), a sample lighting system and light collection optics, a wavelength selector (filter or spectrophotometer), and a detector. Typically, a sample is illuminated with a laser beam in the ultraviolet (UV), visible (Vis), or near infrared (NIR) spectrum.

The lens collects the scattered light and directs it through an interference filter or spectrophotometer in order to acquire the Raman spectrum of a sample [48]

### 2.2.3 Infrared spectroscopy

Infrared spectroscopy (IR) is a powerful technique that can be used to determine the structure of water and polar polyatomic ions present in the water. IR spectroscopy is based on the interaction of IR radiation with molecules, inducing molecular vibrations, and providing information about the bond force constant, polarity and symmetry of a substance. For a water molecule( figure 2.7), the OH symmetric and asymmetric stretching vibrations result from absorption in the 3000 – 3700 $cm^{-1}$ IR region. H-O-H bending vibrations can also be observed at 1640 $cm^{-1}$.

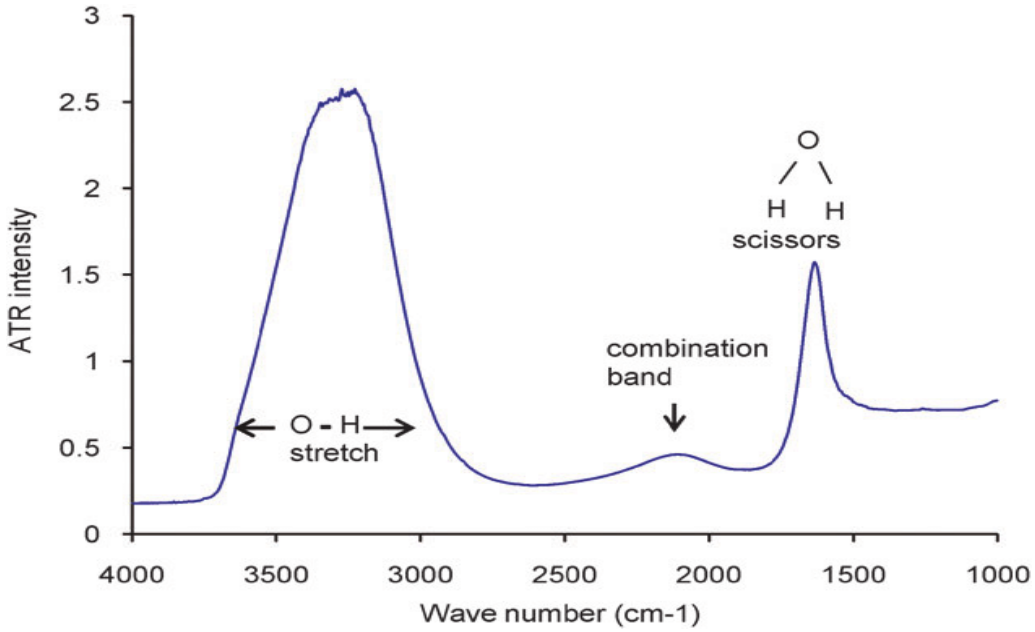


**Figure 2.7** IR spectrum of water, adapted from[49]

The O-H stretching frequencies are dependent on the strength of any hydrogen bonds between neighbouring molecules. Strong hydrogen bonding is associated with lower frequencies (smaller wavenumbers) [50]. According to the standard peak assignments, the strongest hydrogen-bonding results in an O-H absorption peak at 3250 $cm^{-1}$ (most ice-like, each water molecule has four hydrogen bonds to neighbours) and the weakest hydrogen-bonding or nonbonded O−H absorbs at 3600 $cm^{-1}$. Some studies have employed Gaussian curve-fitting to define distinct hydrogen bonding environments; however, many studies have shown that a continuum / continuous distribution of hydrogen bonding environments is more appropriate than the 'mixture' models.

For ions dissolved in water, infrared spectroscopy can also be used to study the water envelopes around the ions in water, as the interaction of ions with water molecules can lead to changes in the frequencies of water vibrations. When studying the effect of adding different ions to the water stretching band, it was found that some appear to strengthen the hydrogen bonds in water, as they shifted the water stretching peak to lower frequencies. Other ions show the opposite effect and shift the absorption peak to higher wavenumbers, suggesting they have weakened hydrogen-bonding compared to pure water. The OH stretch is more sensitive to anions because they interact with the H of water, while cations interact with the lone pairs of the oxygen. The effect of $Li_2SO_4$ on the IR spectrum of water is discussed in detail in section 3.2.3.

In IR spectroscopy, a sample is irradiated with photons and monitored for wavelengths absorbed by the sample. Attenuated total reflectance (ATR) is a sampling technique in which the sample is in contact with an internal reflection element (IRE). The IRE is made from infrared transparent material that has a high refractive index and is used to reflect incident light. It is known that total internal reflectance occurs when the angle of incidence is greater than the critical angle, but only a fraction of the light reaches a few μm into the sample at the reflection point. The beams penetrates a fraction of a wavelength beyond the reflecting surface and when a material that selectively absorbs radiation is in close contact with the reflecting surface, the beam loses energy at the wavelength where the material absorbs[51],[52] .The resultant attenuated radiation is measured and plotted as a function of wavelength by the spectrometer and gives rise to the absorption spectral characteristics of the sample. A schematic of a typical attenuated total reflectance cell is presented in figure 2.8.

In IR spectroscopy, the selection rule is based on changes in the dipole moment of the molecule, and asymmetric vibrations of polar groups result in the most intense absorption bands in the IR spectrum[53]. One of the key advantages of this method is the analysis of small quantities of samples and without sample preparation. Despite its numerous advantages, ATR method has a relatively high sensitivity and susceptibility to the action of environmental factors [54].

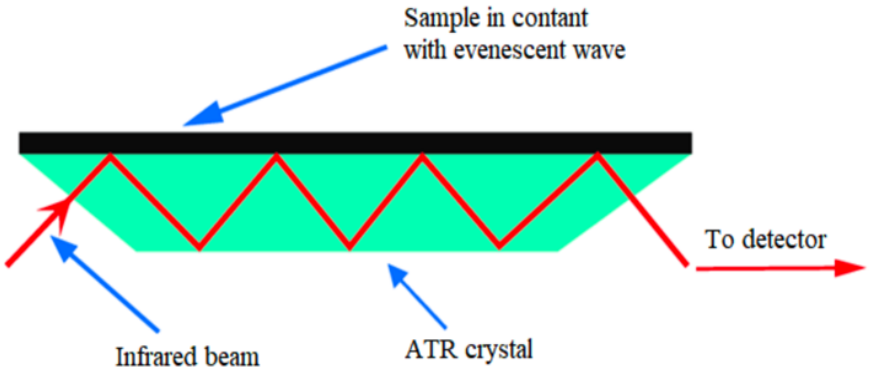


**Figure 2.8** Schematic of a typical attenuated total reflectance cell (taken from[52] )

The depth of penetration in ATR spectroscopy is a function of the wavelength, λ, the refractive index of the crystal, $n_2$, and the angle of incidence radiation, θ. The depth of penetration, $dp$, for a non-absorbing medium is given by the following:

$$dp = (\lambda / n_1) / \{ 2\pi [sin\theta - (n_1 / n_2)^2]^{1/2} \} \qquad (2.6)$$

where $n_1$ is the refractive index of the sample.

The crystals used in ATR cells are made from materials that have low solubility in water and are of a very high refractive index. Such materials include zinc selenide (ZnSe), germanium (Ge), thallium-iodide (KRS-5) and diamond [51].

In order to conduct the in-situ IR spectroelectrochemical studies (figure 2.9), The three electrodes used for the cyclic voltammetry were also used for in a cell located directly above the ATR prism. The IR spectra were measured using a Bruker Tensor 27 spectrometer equipped with a DLaTGS detector operating at room temperature. The spectroscopy was performed at a resolution of 4 $cm^{-1}$ using the OPUS collection programme. The Attenuated Total Reflectance (ATR) mode was employed, with a diamond crystal serving as the internal reflection element (prism).

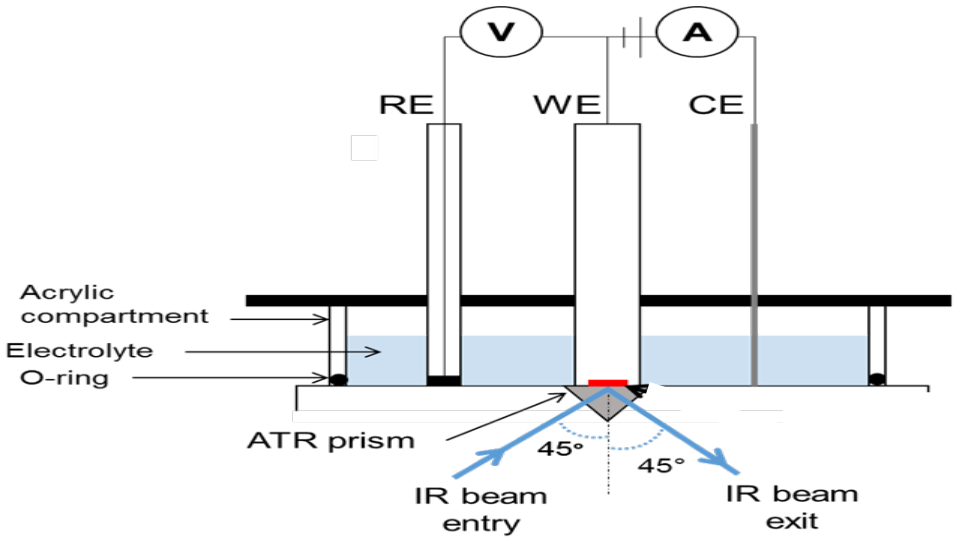


**Figure 2.9** Scheme in situ ATR IR experiment.

The electrochemical cell was placed on top of the spectrometer and clamped in place using a Y-shaped metal holder. The metal holder served the purpose of providing support for the electrochemical cell and maintaining the electrodes in stable locations to prevent any contact between them. The Fe electrode, serving as the working electrode, was covered with Teflon and subsequently prepared by sanding the exposed base with sandpaper and cleaning it with distilled water prior to usage. Ag/AgCl functioned as the reference electrode, while a platinum wire, coiled at the end, was employed as the counter electrode. Prior to insertion into the electrochemical cell, the reference and counter electrodes were cleansed with distilled water and subsequently dried. The electrochemical cell houses electrolytes ($Li_2SO_4$ or $Li_2SO_4$ with $MgCl_2$ or LiTFSI ) at varying quantities. The FTIR spectra were acquired using the entire range of wavenumbers in the mid-infrared region, specifically from 4000 to 400 $cm^{-1}$.

To carry out the spectroelectrochemistry experiments, a spectrum is first recorded without any potential applied at the Fe working electrode. This spectrum acts as the background spectrum. Potential is then applied to the electrode and subsequent spectra measured continuously. The IR spectra presented are therefore difference spectra. These spectra measure changes in the solution species in the region of solution just between the ATR prism and the Fe surface. The experiments were repeated in the same way for all of the different concentration of $Li_2SO_4$.

# CHAPTER 3

# CHARACTERISATION OF AQUEOUS $Li_2SO_4$ SOLUTIONS AT DIFFERENT CONCENTRATIONS

This Chapter presents results of conductivity and viscosity measurements as well as the results of infrared measurements of lithium sulfate solutions at different concentrations. Some characteristics of electrolytes and the dissolution process will also be highlighted. Measurements of viscosity, conductivity, and infrared spectra provide valuable insight into the properties and behaviour of electrolyte solutions.Viscosity measurements are used to determine how a solution's viscosity varies with concentration, in order to understand dissolution behaviour and how molecules interact within a solution. In addition, conductivity measurements with concentration provide information about ion movement, ionic pairing, and the solution structure. Lastly, studying infrared spectroscopy of electrolytes can contribute to an understanding of their chemical properties. Infrared absorption bands can be used to study the interaction between ions and solvent molecules, as well as ion-ion interactions. Therefore, they provide information about changes in water and electrolytes structure. Using the information about the electrolytes obtained from these three methods, we can in later chapters interpret the extent of the effect of electrolyte concentration on the kinetics of iron plating and stripping, as well as the changes that occur at the potentials where iron dissolves.

## 3.1 Introduction to aqueous electrolytes and their properties

### 3.1.1 Structure and properties of water

Water is a simple molecule with the molecular formula $H_2O$. It consists of one oxygen atom bonded to two hydrogen atoms. The water molecule is characterized by its polar properties as a result of the difference in electrical charge between its two ends. This is because the oxygen atom has a greater ability to attract electrons compared to hydrogen atoms, and therefore the oxygen atom gains a partial negative charge with a partial positive charge on the hydrogen atoms. The molecule adopts a bent structure due to the presence of two lone pairs of electrons on the oxygen atom. The H−O−H bond angle is about $105^{o}$. Each hydrogen atom is strongly attracted to the lone pair of electrons on the oxygen atom of a neighbouring water molecule. These are called hydrogen bonds and because each oxygen atom has two lone pairs, it can form hydrogen

bonds with hydrogen atoms in two other separate molecules. Hence overall in bulk water each water molecule can form four hydrogen bonds to its nearest neighbours in a tetrahedral arrangement (figure 3.1).

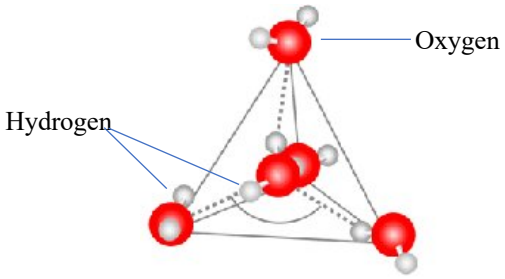


**Figure 3.1** Tetrahedral ordering of the H-bonding in water, adapted from[55]

The radial distribution[39] function expresses the average relative positions of molecules in a liquid, g(r). The function is defined as $g(r)^2\ r\ dr$, which means the probability of finding a molecule in the dr range at a distance r from another molecule. In a crystal, the molecules are in specific locations, so the crystals have long-range order. When the crystal melts, long-range order is lost. In a liquid, near the first particle, the nearest neighboring molecules may remain in their original relative positions, even if they are displaced by other new molecules, as the new particles may adopt the vacated positions. So, it is still possible to detect a sphere of the nearest neighboring molecules at a distance $r_1$, and perhaps beyond them a sphere of the nearest molecules at a distance $r_2$. So, the radial distribution function in the fluid (in the short-range regime) is relatively ordered over short distances, with a peak at $r_1$, and a smaller peak at $r_2$.

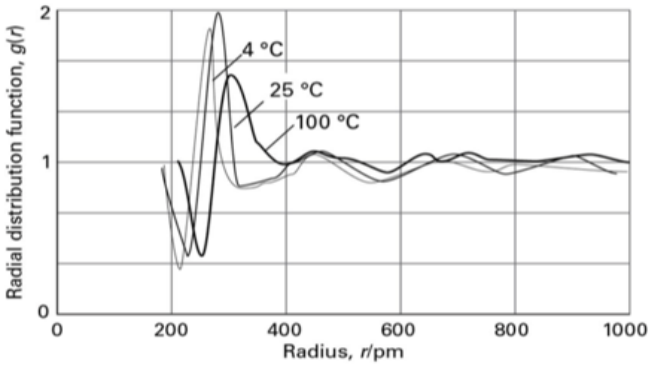


**Figure 3.2** The radial distribution function of the oxygen atoms in liquid water at three temperatures, adapted from[39]

In the figure 3.2, the radial distribution of oxygen atoms in liquid water is depicted. It was found that any $H_2O$ molecule is surrounded by other molecules at the corners of the tetrahedron. At 100°C, intermolecular interactions (especially hydrogen bonds) are still strong enough to retain the basic structure.

Permittivity ($\varepsilon$) is a property of a material that describes how it responds to an applied electric field[39]. Relative permittivity ($\varepsilon_r$) is the ratio of the permittivity of a substance to the permittivity of a vacuum ($\varepsilon_0$). Hence $\varepsilon_r = \varepsilon/\varepsilon_0$. The relative permittivity of a substance is measured by comparing the capacitance of a capacitor with and without the substance present between the plates (C and $C_0$, respectively) and using $\varepsilon_r = C/C_0$. For instance, water has a relative permittivity of 78 at 25 °C. The relative permittivity of a substance is large if its molecules are polar or highly polarizable. The quantitative relation between the relative permittivity and the electric properties of the molecules is obtained by considering the polarization of a medium. The relative permittivity can have a very significant effect on the strength of the interactions between ions in solution. Water has a very high permittivity. This means that it has high solvation energy for most ions. Water reduces the force of attraction between the ions, and then water molecules surround the ions to form the electrolyte.

### 3.1.2. Dissolution of ions in water

Dissolution is the interaction of a solvent with dissolved molecules (solute). Ionized and uncharged molecules interact strongly with the solvent, and the strength and nature of this interaction affects many properties of the solute and the solvent. In the process of dissolution of ionic substances, the solute ions are surrounded by a concentric shell of solvent molecules, and thus, dissolution is the process of reorganization of solvent and solute molecules into solvation complexes. Dissolution involves the formation of a non-covalent interaction—usually, hydrogen bonding, van der Waals forces or electrostatic (Coulombic) interaction —and in the case of water[39], the process is referred to as hydration. Water, being a polar molecule with a bent shape and possessing a high dipole moment, is an excellent solvent for many ionic compounds due to its ability to interact with and dissolve charged species.

As shown in figure 3.3, the first hydration shell, made up of water molecules, immediately surrounds the ion. The interactions here between water molecules and ions are strong as according to Coulomb's law the electric field of an ion decreases as a function of the inverse square of distance from the ion. The ion electric field therefore has a strong effect on the orientation of the water molecules. The oxygen atoms in the water molecules are oriented toward the cation, with the partially negative oxygen facing the positively charged cation. The hydrogen atoms in the water molecules are oriented toward the anion, with the partially positive hydrogen facing the negatively charged anion. In the second hydration shell, the interactions of water molecules with ions are weaker compared to those in the first layer. They may still be under the influence of the ion electric field but can also be more easily reorientated and exchanged with other water molecules. Beyond the second hydration shell, the water molecules have properties similar to pure water devoid of dissolved ions. The dissolution process is particularly crucial for understanding the behavior of electrolyte solutions.

.

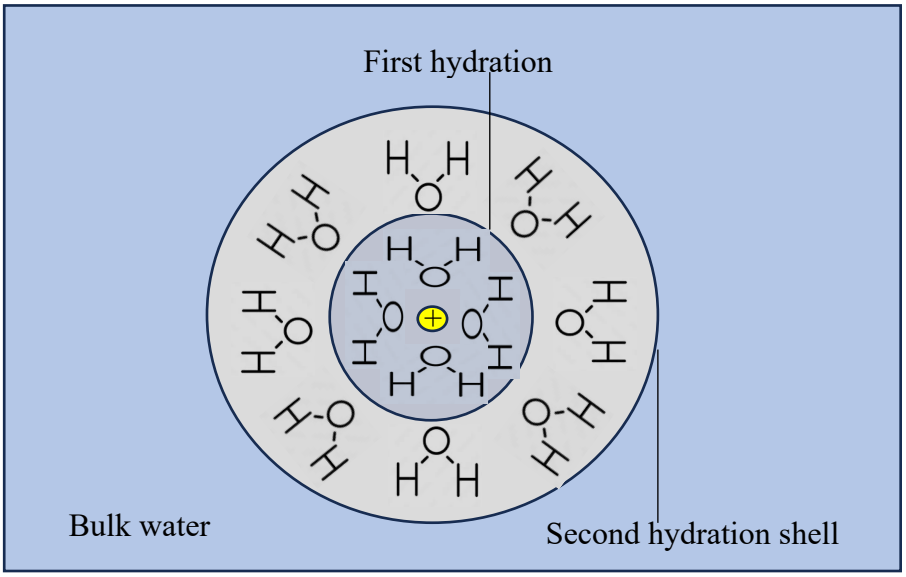


**Figure 3.3** Schematic diagram to show a first hydration shell, a second hydration water shell, and bulk water surrounding the ion.

In order to understand the behavior and properties of an electrolyte, we must understand the ion pair structures that form between the solvated ions and water. When the ions are completely dissolved, water molecules completely surround the electrolyte ions. Water molecules therefore separate the electrolyte's cations from its anions. This condition is called solvent separated ion pairs (SSIPs) and

often occurs at dilute concentrations (figure 3.4). When the electrolyte concentration increases, the water concentration decreases. This results in direct contact between the cations and anions of the electrolyte without a large number of intervening water molecules. This is what we call contact ion pairs (CIPs). In some cases, electrolyte cations and anions form larger aggregates and structures in solution (cation-anion groups (AGGs))[56] with fewer free water molecules. The presence of SSIPs, CIPs and AGGs ion pairs significantly affects the conductivity and viscosity of the electrolyte.

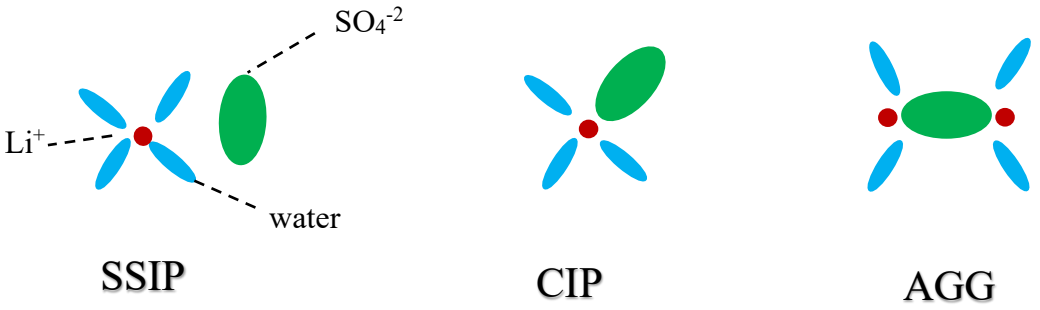


**Figure 3.4** Three general forms of interactions between solvent and ions in dilute and concentrated electrolyte, adapted from[56]

## 3.2 Results and Discussion

### 3.2.1 Conductivity

The relationship between measured conductivity ($\kappa$) and concentration is plotted in figure 3.5, for various electrolyte concentrations (0.1, 0.4, 1.0, 1.8, 2.0, 2.5 M $Li_2SO_4$) and the values obtained are shown in Table 3.1.

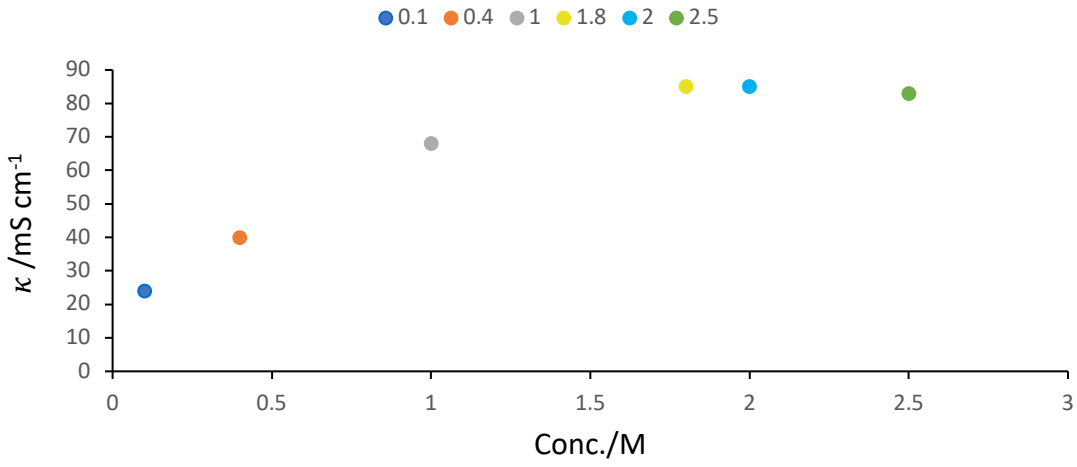


**Figure 3.5** The relationship between conductivity ($\kappa$) of different concentrations of $Li_2SO_4$ with concentrations at 25°C.

The conductivity value started with 24 mS $cm^{-1}$ at 0.1 M and then increased steadily to about 40 and 68 mS $cm^{-1}$ at 0.4 and 1.0 M, respectively. After that, there was a gradual increase for the conductivity from 1.0 M to 1.8 M until its value levelled off and stayed at 85 mS $cm^{-1}$ at the remaining higher concentrations.

**Table 3.1** Conductivity for different concentrations of $Li_2SO_4$ electrolyte at 25°C.

| Concentration / M | $\kappa_1$ mScm$^{-1}$ | $\kappa_2$ mScm$^{-1}$ | $\kappa_3$ mScm$^{-1}$ | $\kappa_{average}$ / mScm$^{-1}$ | error |
|---|---|---|---|---|---|
| 0.1 | 20.78 | 25.7 | 26.3 | 24 | +/- 3 |
| 0.4 | 42 .3 | 38.4 | 39.6 | 40 | +/- 2 |
| 1.0 | 71.9 | 65.4 | 68.1 | 68 | +/- 2 |
| 1.8 | 87.6 | 81.4 | 84.8 | 85 | +/- 1 |
| 2.0 | 87.0 | 81.5 | 85.1 | 85 | +/- 1 |
| 2.5 | 85.8 | 80.5 | 83.8 | 83 | +/- 1 |

It can be seen that initially to 1.8 M the conductivity values gradually increase as the concentration increases, as the number of charged ions that carry the current increase. When the concentration of electrolytes increases beyond 1.8 M it might be expected that conductivity should continue to increase. However, the conductivity remains relatively constant. This suggests at these concentrations ion mobility is decreased and this prevents further increase in conductivity. It also indicates the potential formation of ion pairs due to the much higher concentration of ions compared to the water present. It is known that ion pairs do not move so effectively in response to an electric field as they are less charged than free ions (they may have a small dipole). Therefore, conductivity decreases because it largely measures the movement of free ions.(there are similar results to this research but with different electrolytes).

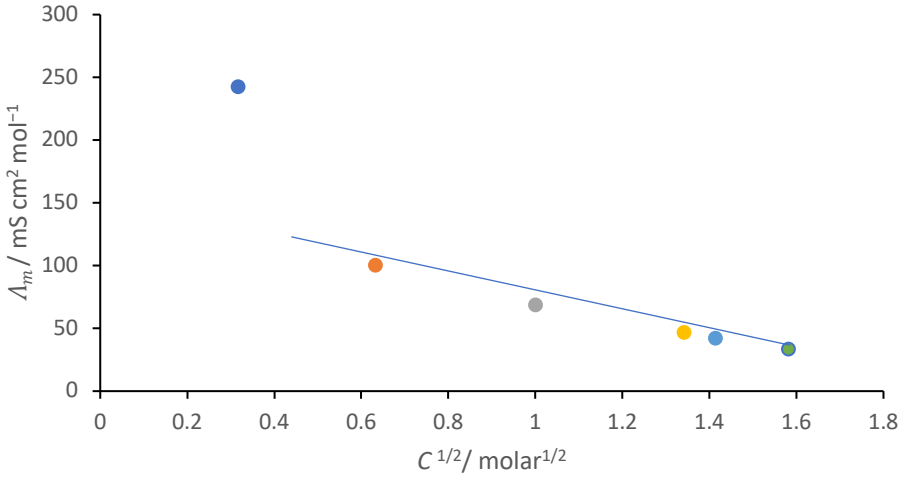


**Figure 3.6** The relationship between molar conductivity ($\Lambda_m$) of different concentrations of $Li_2SO_4$ with the square root of molar concentrations at 25°C.

In figure 3.6, the molar conductivity ($\Lambda_m$), of different concentrations of $Li_2SO_4$ is shown. The molar conductivity of square root of 0.1 M $Li_2SO_4$ reached its maximum value at 243 mS cm$^2$ mol$^{-1}$. Then it decreased dramatically to nearly 100 mS cm$^2$ mol$^{-1}$ at square root of 0.4 M. There was a gradual decrease in the molar conductivity of square root of 1.0 and 1.8 M by about 68 and 47 mS cm$^2$ mol$^{-1}$, respectively. However, at high concentrations, the change in molar conductivity values was slight, as its value decreases to 42 and 33 mS cm$^2$ mol$^{-1}$ at the square root of the concentration of 2 and 2.5 M, respectively.

At low concentrations of 0.1, 0.4 and 1 M, the molar conductivity decreases clearly due to electrostatic interactions between the ions. The number of charged ions in the solution increases, which slows down the movement of ions in response to the electric field.

At higher concentrations, the interaction between ions due to ion pairing increases, and thus the concentration of free-moving ions could be lower than expected. This makes the effect of high concentrations on molar conductivity not as straightforward to explain as at lower concentrations. Increased solution viscosity may also reduce the ion mobility as determined in the next section.

### 3.2.2 Viscosity

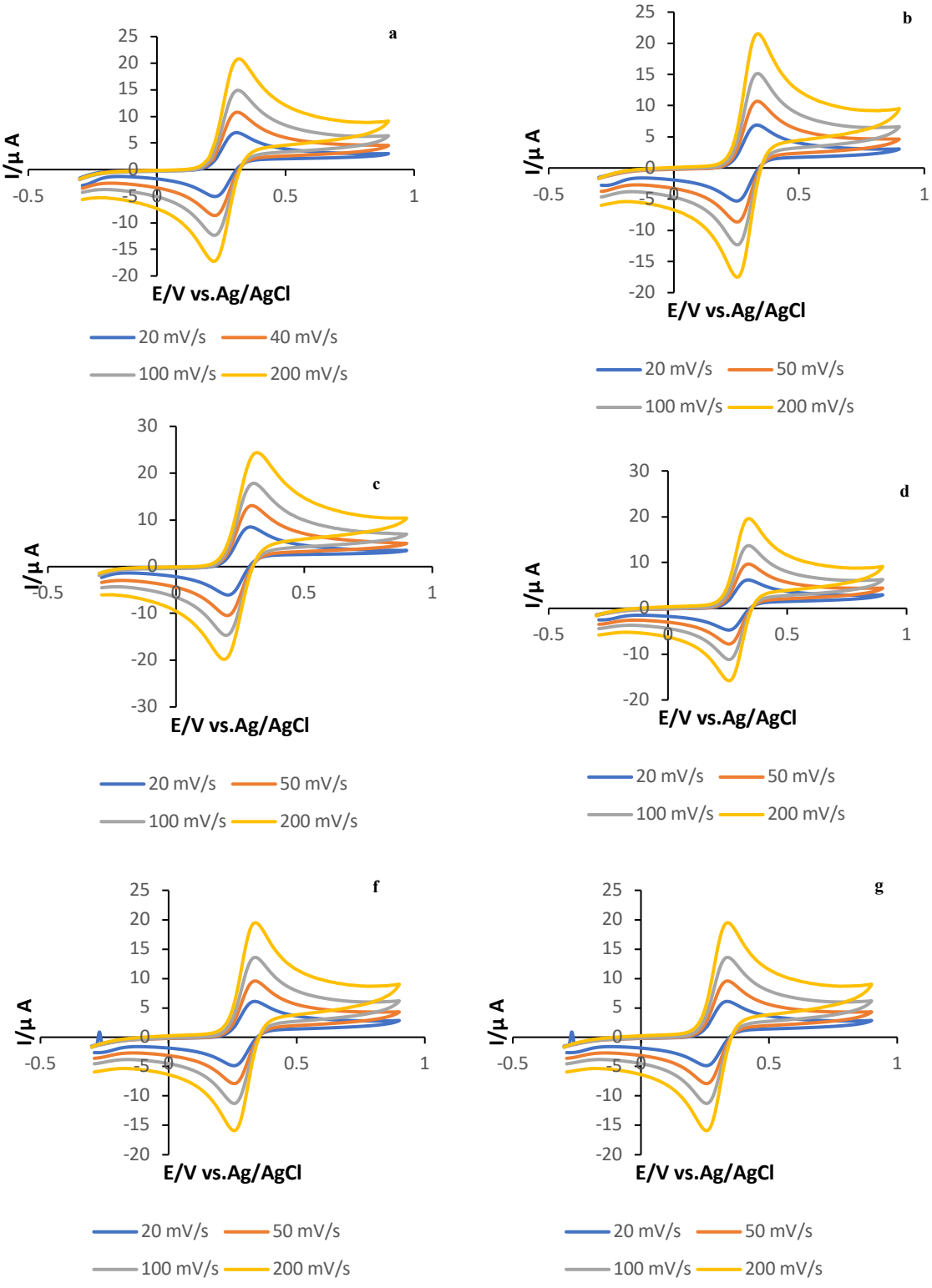


**Figure 3.7** Cyclic voltammetry at different scan rate of 1.5 mm radius Glassy Carbon in 1mM $K_3Fe(CN)_6$ with a) 0.1M b) 0.4M c) 1.0M d) 1.8 M e) 2.0 M f) 2.5 M $Li_2SO_4$.

**Table 3.2** $i_p^{ox}$ determined from cyclic voltammetry for 1 mM $K_3Fe(CN)_6$ in different concentrations of $Li_2SO_4$ at four different scan rates (20, 50, 100, 200 $mVs^{-1}$)

| $\upsilon$ $mVs^{-1}$ | $\sqrt{\upsilon}$ $(Vs^{-1})^{1/2}$ | $i_p^{ox} x10^{-6}/A$ | | | | | |
|---|---|---|---|---|---|---|---|
| | | 0.1 M | 0.4 M | 1.0 M | 1.8 M | 2.0 M | 2.5 M |
| 20 | 0.14 | 8.48 | 6.88 | 6.94 | 6.18 | 6.08 | 6.01 |
| 50 | 0.22 | 13.0 | 10.7 | 10.8 | 9.66 | 9.41 | 8.99 |
| 100 | 0.31 | 17.8 | 15.1 | 14.9 | 13.7 | 13.4 | 12.4 |
| 200 | 0.44 | 24.3 | 21.5 | 20.8 | 19.6 | 19.2 | 17.6 |

The viscosity of the electrolytes was studied by determining the diffusion coefficient, D, of $Fe(CN)_6^{4-}$ dissolved in each electrode using cyclic voltammetry at four scan rates (20, 50,100, 200 mV/s). Figure 3.7,a shows the CV of 1 mM of $K_4Fe(CN)_6$ with 0.1 M $Li_2SO_4$ at different scan rates at a glassy carbon electrode. The scan started from -0.3 V and was scanned towards 0.9 V. As can be seen in the first scan at 20 mV/s (in blue), the oxidation current initially appears at 0.15 V and flows continuously until it reaches its peak at 0.25 V. The oxidation process can be assigned as:

$$Fe(CN)_6^{-4} = Fe(CN)_6^{-3} + e^- \qquad (3.1)$$

On reversing the scan a reduction current for the reverse reaction appears at 0.35 V. As scanning continues at different scan rates, the peak currents $i_P$ increase with increase in scan rate, as described by the Randles - Sevcik equation (2.5) for reversible electrochemical reactions.

The peak current values for 1 mM $Fe(CN)_6^{4-}$ in different concentrations of $Li_2SO_4$ are summarized in Table 3.2. It can be seen that the $i_p^{ox}$ value decreases significantly as the concentration of $Li_2SO_4$ increased from 0.1 M to 2.5 M, indicating that the diffusion coefficient becomes smaller as the electrolyte concentration increases. A plot of $i_p^{ox}$ against $\sqrt{\upsilon}$ allows D to be calculated from the gradient:

$$Gradient = 2.69x10^5 n^{3/2} AC\sqrt{D} \qquad (3.2)$$

The plot is shown in Figure 3.8

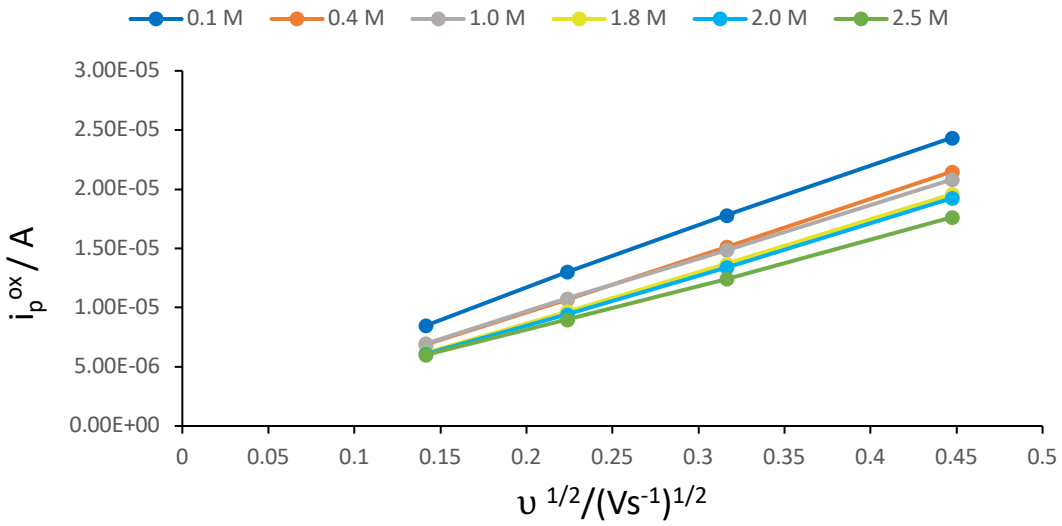


**Figure 3.8** A plot of peak oxidation current versus the square root of (20,50,100,200 $mVs^{-1}$) scan rates of $K_4Fe(CN)_6$ in different concentrations of $Li_2SO_4$ using Randles - Sevcik equation.

In these experiments, the electrode area $A = \pi r^2 = \pi(0.15)^2 = 0.07$ $cm^2$

So, as an example calculation *D* for $Fe(CN)_6^{-4}$ in 0.1 M $Li_2SO_4$ is:

$5.17x10^{-5} = 2.69x10^5 \times 1 \times 0.07 \times 0.000001\sqrt{D}$

$5.17x10^{-5} = 0.01883\sqrt{D}$

$2.745 \times 10^{-3} = \sqrt{D}$

$D = 7.5 \times 10^{-6}$ $cm^2$ $s^{-1}$

The values for D in the other concentrations of $Li_2SO_4$ electrolyte were calculated in the same way and are summarized in Table 3.3.The values are plotted against concentration of electrolyte in Figure 3.9,a.

**Table 3.3** The viscosity and diffusion coefficient data of $Fe(CN)_6^{-4}$ in different concentrations of $Li_2SO_4$.

| C<br>M | slope | $\sqrt{D}$ | D x$10^{-6}$<br>$cm^2s^{-1}$ | D x$10^{-10}$<br>$m^2s^{-1}$ | η<br>m Ps |
|---|---|---|---|---|---|
| 0.1 | 5.17E-05 | 0.0027 | 7.55 | 7.55 | 0.68 |
| 0.4 | 4.78E-05 | 0.0025 | 6.44 | 6.44 | 0.80 |
| 1.0 | 4.52E-05 | 0.0024 | 5.77 | 5.77 | 0.89 |
| 1.8 | 4.38E-05 | 0.0023 | 5.42 | 5.42 | 0.95 |
| 2.0 | 4.31E-05 | 0.0021 | 4.59 | 4.59 | 0.98 |
| 2.5 | 3.80E-05 | 0.0020 | 4.07 | 4.07 | 1.2 |

The viscosity values $\eta$ of the different solutions were calculated using the Stokes–Einstein equation (3.3), as shown for the 0.1 M $Li_2SO_4$ solution:

$$\eta = \frac{k_B\ T}{6\ \pi\ D\ r} \qquad (3.3)$$

$$\eta = \frac{1.38 \text{ x } 10^{-23} \text{x } 298}{6 \text{ x } 3.14 \text{ x } 7.55 \text{ x } 10^{-10} \text{ x } 4.22 \text{ x } 10^{-10}}$$

$\eta = 0.00068$ Pa s = 0.68 mPa s

Where the hydrodynamic radius of $Fe(CN)_6^{-4}$ r = 0.422 nm [57]

The calculated values for all of the solutions are shown in Table 3.3. They are also plotted as a function of electrolyte concentration in Figure 3.9, b.

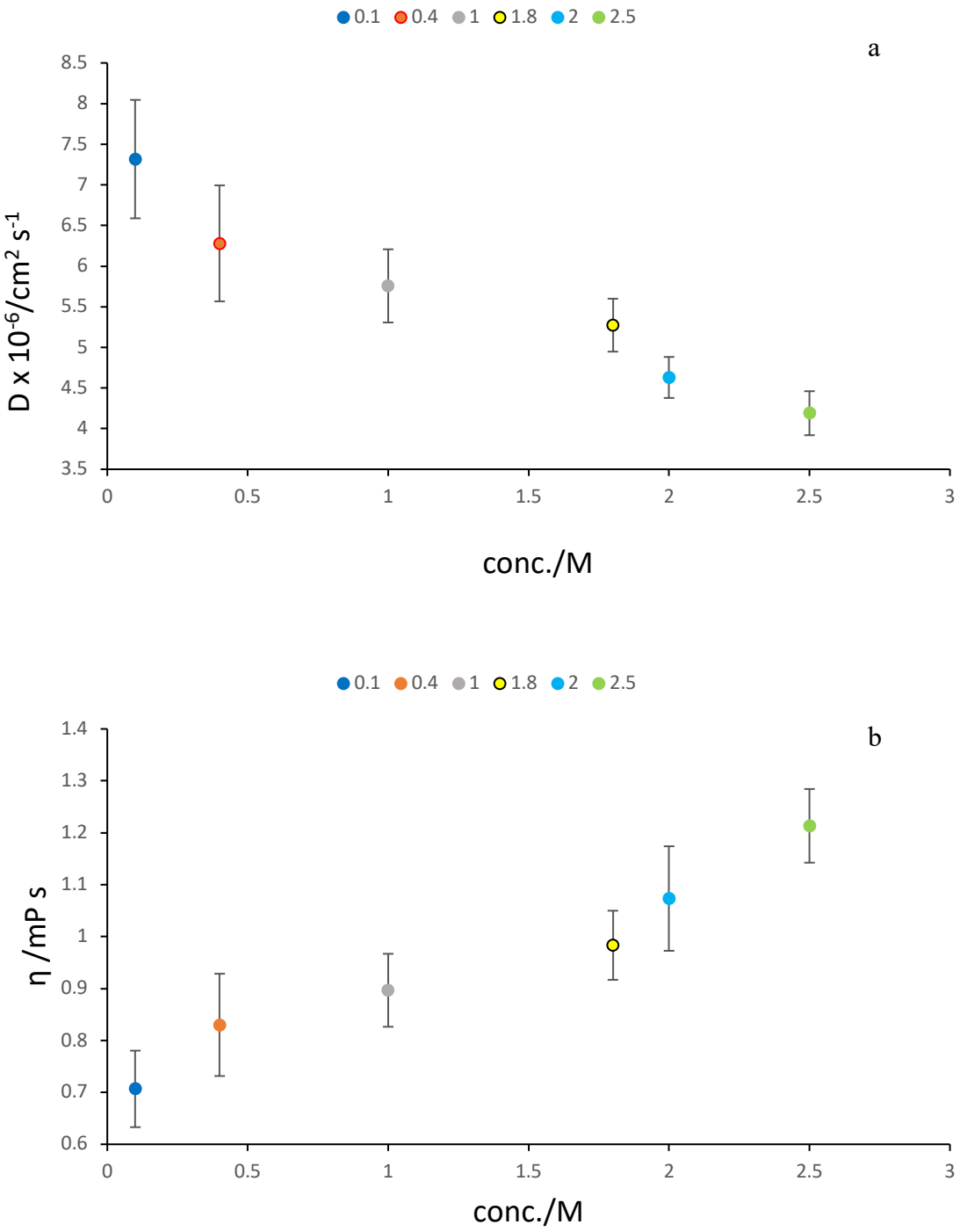


**Figure 3.9** The effect of concentrations of $Li_2SO_4$ on (a) diffusion coefficient of $Fe(CN)_6^{4-}$ determined using Randles - Sevcik equation; (b) solution viscosity determined by using the Stokes–Einstein equation.

For the low electrolyte concentrations (0.1 and 0.4 M) the calculated diffusion coefficients for $Fe(CN)_6^{4-}$ of 7.55 x $10^{-6}$ and 6.44 x $10^{-6}$ $cm^2s^{-1}$ are very close to values of D for this species in previous study [58]. But the values of the diffusion coefficients for the higher concentrations are new as they have not been measured before.

The Randles – Sevcik equation(2.5) assumes fully reversible kinetics, however some of the CVs in figure 3.7 show evidence of increasing peak separation ($\Delta E_p$) with increasing scan rates that is indicative of quasireversible kinetics. In table 6, the $\Delta E_p$ values extracted from Figure 3.7 are shown. It gives us information about the oxidation and reduction kinetics that occur on the surface of the electrode. The values of $\Delta E_p$ at 0.1 M and 2.5 M indicate that the reaction was rather slow under these conditions but is fast and reversible in the other solutions. The reason for the slower kinetics at 0.1 M and 2.5 M is unclear (and beyond the scope of this work) but suggest that the values for D determined for concentration of 0.1 M and 2.5 M could be slightly underestimated. However the trends and general conclusions remain unaffected.

**Table 3.4** $\Delta E_p$ determined from cyclic voltammetry for 1 mM $K_3Fe(CN)_6$ in different concentrations of $Li_2SO_4$ at four different scan rates (20, 50, 100, 200 $mVs^{-1}$).

| $\upsilon$ / $mVs^{-1}$ | $\sqrt{\upsilon}$/ $(Vs^{-1})^{1/2}$ | $\Delta E_p/mV$ | | | | | |
|---|---|---|---|---|---|---|---|
| | | 0.1 M | 0.4 M | 1.0 M | 1.8 M | 2.0 M | 2.5 M |
| 20 | 0.14 | 80 | 80 | 80 | 80 | 90 | 90 |
| 50 | 0.22 | 100 | 90 | 90 | 80 | 90 | 90 |
| 100 | 0.31 | 100 | 90 | 90 | 80 | 90 | 100 |
| 200 | 0.44 | 130 | 90 | 90 | 80 | 90 | 120 |

In figure 3.9.a, it was found that the relationship between the diffusion coefficient (D) and the concentration is inverse. That is, the value of D decreases with increasing concentration. D records the highest value at 0.1 M (7.55 $x10^{-6}$ $cm^2$ $s^{-1}$). Then the value began to decrease with increasing concentration until it reached the lowest value at 2.5 M by 4.07 $x10^{-6}$ $cm^2$ $s^{-1}$.

On the other hand, the relationship between viscosity and concentration is direct, as shown in figure 3.9, b. The viscosity value was lowest at 0.1 M (0.68 mPa s). Then the viscosity values began to increase with increasing concentration until it reached the highest value at 2.5 M. From figure 3.9 a,b we notice that the effect of concentration on the viscosity in the 0.1 and 0.4 M diluted solutions is small. As the values obtained are both close to the viscosity of pure water, which at 25

°C is 0.89 mPa s, while in concentrated solutions we find that as the concentration increases, the viscosity increases, and the diffusion rate decreases.

### 3.2.3 IR Spectroscopy:

The IR difference spectra for different concentrations of $Li_2SO_4$ are shown in Figure 3.10 (region 1400 – 800 $cm^{-1}$) and Figure 3.12 (3900 – 2500 $cm^{-1}$).

In order to begin the IR experiment, air is taken as background, then $H_2O$ is placed on the ATR prism and its spectrum is taken. All spectra are measured for different concentrations of $Li_2SO_4$ after taking air as background. The IR spectra presented in this chapter are difference spectra, where the spectrum of water has been subtracted from the spectra of lithium sulfate solution spectra with its different concentrations. This is removed any contribution from bulk water. The changes in $H_2O$ absorption due to interaction with $Li^+$ and $SO_4^{2-}$ are highlighted.

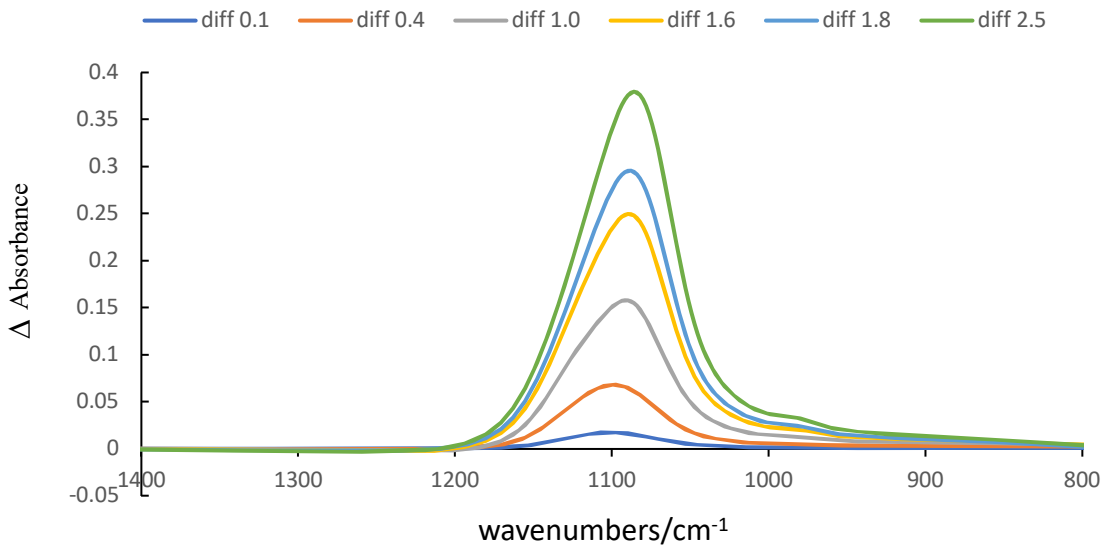


**Figure 3.10** Infrared spectrum of $Li_2SO_4$ at different concentrations at region 1400 – 800 $cm^{-1}$.

In Figure 3.10, a sharp symmetrical peak appears at 1095 $cm^{-1}$ for 0.1 and 0.4 M $Li_2SO_4$ resulting from the asymmetrical IR stretching mode of $SO_4^{2-}$. As the concentration of $Li_2SO_4$ increases from 1.0 M to 2.5 M, the frequency of the $SO_4^{2-}$ stretch maximum shifts from 1095 $cm^{-1}$ to 1081 $cm^{-1}$. The peak also becomes less symmetric, with a broadening to the higher wavenumber side of the peak. In addition, a new absorption feature starts to emerge at 980 $cm^{-1}$ that increases in intensity with ion concentration.

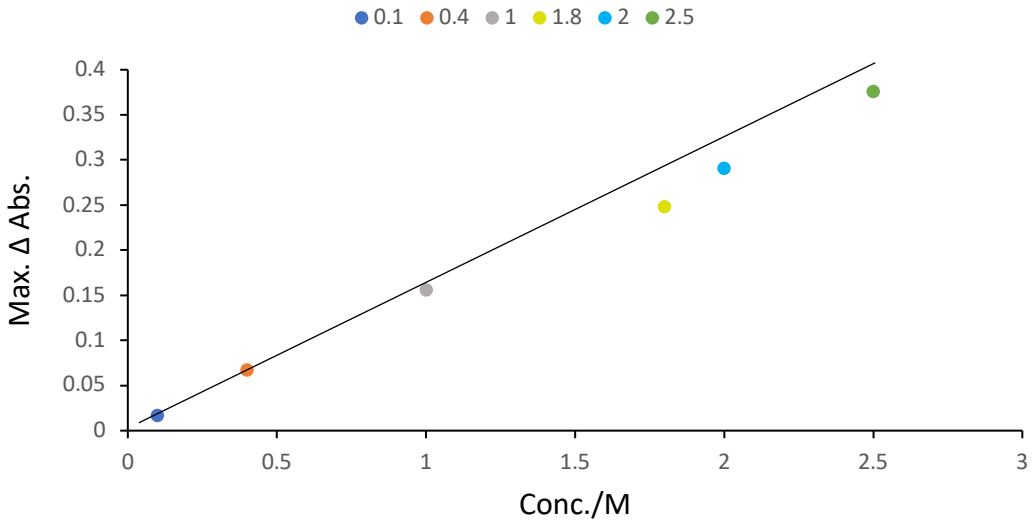


**Figure 3.11** The relationship between the maximum infrared absorption of sulfate at different concentrations of $Li_2SO_4$ with concentrations at region 1400 – 800 $cm^{-1}$.The line is a guide to the eye to show that the peak maximum is linear with concentration of $Li_2SO_4$ at concentrations up to 1 M.

The maximum absorption of the sulphate peak for different concentrations of lithium sulfate with time are plotted in Figure 3.11. There was an obvious increase in the maximum sulfate peak from 0.017 at 0.1 M to 0.379 at 2.5 M. The line passing through the origin represents the linear increase of the sulfate band intensity with concentration. This line passes through the data points up to 1.0 M but for higher concentration the data points lie slightly below the line. This small deviation may be due to increasing asymmetry of the peak at the higher concentration.

Table 3.5, shows the wavenumbers at which the maximum absorbance occurs at different concentrations of $Li_2SO_4$. It also shows the full width at half maximum (FWHM) values for each spectrum.Where a narrower FWHM indicates a sharper peak. There is not a significant change in the FWHM with concentration.

**Table 3.5** Max wavenumbers and FWHM determined from IR spectrum for different concentrations of $Li_2SO_4$ .

| Conc./M | Max wavenumber/$cm^{-1}$ | FWHM/$cm^{-1}$ |
|---|---|---|
| 0.1 | 1095 | 73.28 |
| 0.4 | 1095 | 71.36 |
| 1.0 | 1087 | 71.36 |
| 1.8 | 1083 | 71.36 |
| 2.0 | 1083 | 71.36 |
| 2.5 | 1081 | 71.36 |

The unmodified (isolated) sulfate ion has tetrahedral symmetry and expected vibrational modes at 1050-1250 $cm^{-1}$ (asymmetric stretching) and 980 $cm^{-1}$ (symmetric stretching). Since symmetric expansion does not lead to any change in the dipole, it is inactive in the IR spectrum. However, asymmetric expansion is very active in the IR which is the band we observe at 1095 $cm^{-1}$ in 0.1 M $Li_2SO_4$. This asymmetric stretch has a triplet degeneracy but if the sulfate loses its symmetry, this degeneracy will be lost, and the infrared band will show evidence of splitting and broadening. Looking at figure 23, we find that there is some broadening (a shoulder) to the peak for the spectrum of 1 M $Li_2SO_4$. This indicates a loss of symmetry of the sulfate ion at 1 M and above due to its interactions with the surrounding ions[59]. One or more oxygen atoms react strongly with neighboring ions, such as lithium, and thus lose equivalence with the other oxygen atoms. This leads to asymmetry of the infrared band of the sulfate ion.

The feature that begins to appear at 980 $cm^{-1}$ is at the wavenumber where inactive infrared symmetric stretching is expected. Some studies have reported weak absorption in this region due to coupling of molecular vibrations between neighboring molecules and the mode may also become somewhat infrared permissible if molecular interactions cause a dipole change associated with this vibration due to symmetry distortion. The appearance of this feature at 1 M and

above again suggests increased intermolecular interactions between the sulphate ion and other species in solution.

Another important point that may explain the loss of symmetry of the sulfate ion is the strong Stark effect [60] resulting from the interaction of $SO_4^{-2}$ with its surrounding environment. The shift in the stretching frequency of $SO_4^{-2}$ from 1095 $cm^{-1}$ at 0.1 M to 1081 $cm^{-1}$ at 2.5 M can be related to the electric field generated by other ions in the solution.

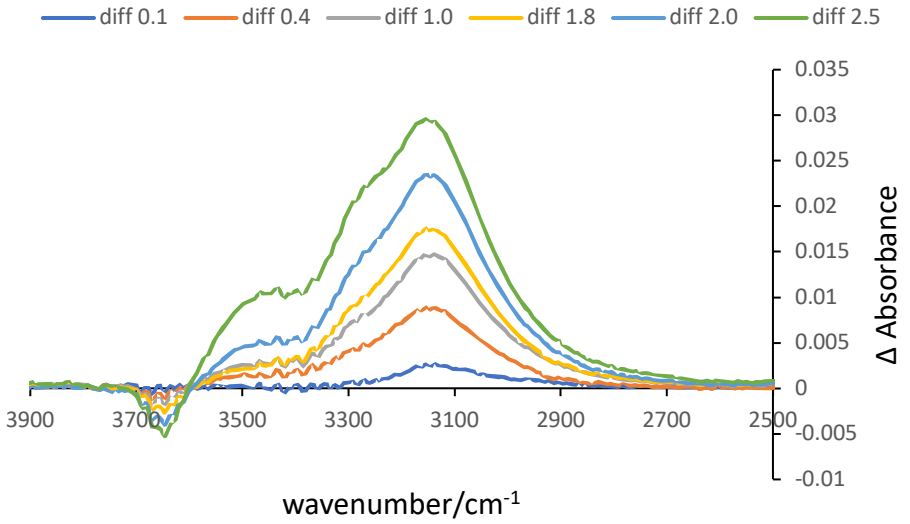


**Figure 3.12** Infrared spectrum of $Li_2SO_4$ at different concentrations at region 4000 – 2500 $cm^{-1}$.

Figure 3.12 shows the difference IR spectra for different concentrations of $Li_2SO_4$ solution at wavenumbers from 2700 to 3700 $cm^{-1}$ corresponding to changes in the absorption for the water symmetric and antisymmetric stretching modes. It was observed that a negative band appeared at 3643 $cm^{-1}$ and the higher the ion concentration, the greater intensity of the peak in the negative direction. At 3445 $cm^{-1}$ a broad positive shoulder appears, the intensity of which increases from 0.1 M to 2.5 M. In addition, a sharp positive peak appears at 3147 $cm^{-1}$ and its intensity increases from 0.1 M to 2.5 M. This peak is asymmetric in shape, with a shoulder to the higher wavenumber side, centered at about 3275 $cm^{-1}$.

Ionic hydration explains the increase in band intensity in the negative direction at 3643 $cm^{-1}$ with increasing concentration in Figure 3.12. Absorption in this region is usually associated with water with few or no hydrogen bonds to neighbours, as

discussed earlier. The loss of absorption at this wavenumber suggests that the small lithium cations with high charge density interact strongly with these 'free' water molecules. In contrast, the increase in absorption to the lower wavenumbers suggests increased hydrogen bonding between water molecules, caused by the presence of the ions. This is because there is increased association between the water molecules within the hydration shell of the Li cation[50].

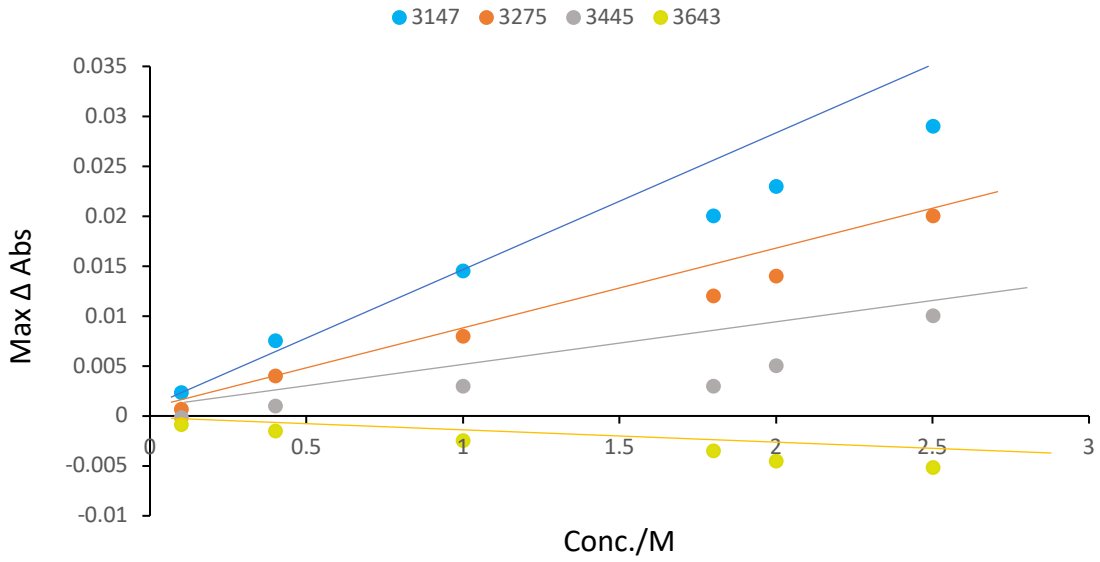


**Figure 3.13** Relationship between maximum band intensity at 4 wavenumbers with different concentrations of lithium sulfate.

When plotting the relationship between the maximum absorption with different concentrations of $Li_2SO_4$ at four wavenumbers, as shown in Figure 3.13, we find that the increase in band intensity with concentration is non-linear. Regarding the three bands for three wavenumbers, they followed a similar positive upward trend. There was a slight increase in absorption from 0.1 M to 1.8 M, followed by a less steep increase at concentrations above 1.8 M.

In contrast, the band at 3643 $cm^{-1}$ showed a negative trend at all concentrations. At 0.1 M, the absorption started at -0.0009, then the value continued to decrease slightly until 1.8 M. Then the absorption intensity gradually decreased to -0.004 and -0.0052 at 2 and 2.5 M, respectively.

The difference spectra of different ions (including $Li_2SO_4$) in water have been studied in detail previously [50] .By comparing different solutions, the authors were able to determine the contribution that each ion makes to the IR spectrum of water. Previous studies show that sulfate has little effect on the water stretching band, so the changes to the water bands on addition of $Li_2SO_4$ can be attributed to $Li^+$ solvation alone. In the paper the researchers determined the effect of addition of $Li^+$ to a concentration of 2 M and as $Li_2SO_4$ has two mols of $Li^+$ per mol of salt this is the equivalent of up to 1 M $Li_2SO_4$. We can therefore compare the results in this chapter for concentrations up to 1 M $Li_2SO_4$ with the results in the paper.

Figure 3.14 d,e, shows the difference in IR spectra for concentrations from 0.1 to 1 M of LiCl and $Li_2SO_4$ at wavenumbers from 0 to 3800 $cm^{-1}$ taken from the reference paper[50]. A sharp positive peak appears at 3170 $cm^{-1}$ for both solutions, which increases in intensity with increasing solution concentration. Both also show a negative peak at 3600 $cm^{-1}$, and its intensity increases in the negative direction with increasing concentration. The broad positive shoulder appears only in the lithium sulfate spectra, the intensity of which also increases with increasing concentration. Our results for $Li_2SO_4$ are in board agreement with this study.

Intensity of the 3170 $cm^{-1}$ band for lithium sulfate and chloride solutions were calculated to evaluate differences in band intensities for the two solutions (Figure 3.14,f). We note that the band intensity shifts downward from the linear trend at higher concentrations of $Li_2SO_4$ solution (0.5 - 1 M). This was attributed as due to the formation of SSIP ion pairs at these higher concentrations and to the high ability of ions to hydrate (this will be explained in detail below). In contrast the intensity of the 3170 $cm^{-1}$ band for LiCl showed a linear increase in intensity showing the ions fully hydrated even at higher concentrations with no evidence of ion pairing.

The results of the paper are consistent with the results of this research from 0 to 1 M of $Li_2SO_4$ at 3147 $cm^{-1}$ but results at concentrations above 1 M are new and have not been measured before. We find (see Figure 3.13) that the band intensity deviates from the linear trend with increasing $Li^+$ concentration.

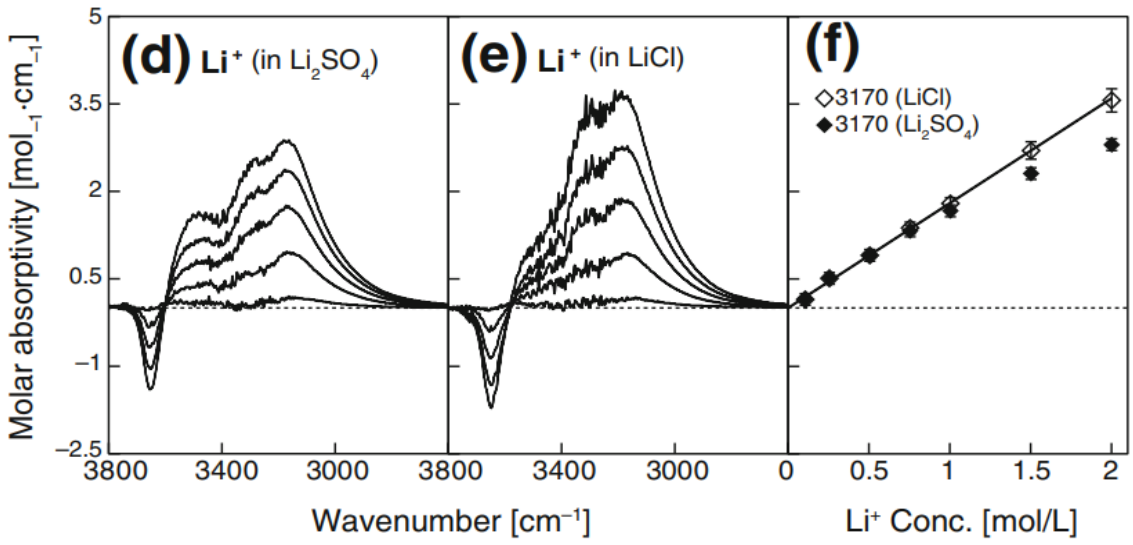


**Figure 3.14** Spectral comparisons of the effects of $Li^+$ extracted from the spectra of $Li_2SO_4$ solutions (d) and those of LiCl solutions (e). intensities (f) of the band maxima at 3,170 $cm^{-1}$ observed in d and e as a function of the $Li^+$ concentration, adapted from[50]

The deviation from linearity is because the effect of $Li_2SO_4$ on water stops being additive when concentration above 1 M $Li^+$ (0.5 M $Li_2SO_4$) are reached due to increased interactions between sulfate and lithium. There are two reasons that may explain this, the first of which is the formation of weak ion pairs (double-solvent-separated ion pair (2SIP) and solvent-shared ion pair (SIP)).

Initially, $Li^+$ (aq) and $SO_4^{-2}$ (aq) are proposed to form double-solvent-separated ion pairs (2SIPs), retaining virtually all of their hydration sheaths. Afterwards, solvent shared ion pairs (SIPs) are formed after the loss of intervening water molecules. These changes are summarized as follows,[61] :

$$Li^+_{aq} + SO^{2-}_{aq} \Leftrightarrow [Li^+.OH_2.OH_2.SO_4^{2-}]aq \Leftrightarrow [Li^+.OH_2.SO_4^{2-}]aq \qquad (3.4)$$

Free ions 2SIP SIP

The second reason is that sulfate and lithium ions are strongly hydrating ions, so they work to trap the freedom of motion of the water molecules. This effect can go beyond the first hydration layer into several layers of surrounding water. Thus, lithium strengthens the hydrogen bonding structure in the surrounding water.

### 3.3 Conclusion

The results of this study showed that electrolyte concentration affects the properties of electrolyte. Using conductivity measurements , it was observed that the conductivity of the electrolyte solution increases from lower concentration to 1.8 M with an increase in charged ions, then the conductivity stabilizes and does not change with increasing concentration. This is due to the immobility of ions as their concentration increases and the formation of ion pairs that do not move, which leads to stable conductivity.

As for the viscosity, it was found to increase significantly with increasing concentration due to the absence of free water, as most of the ions are bound to water. There is therefore more friction between the molecules in solution so the solution has less fluidity. At concentrations above 1.8 M the viscosity is very high and may suggest that even greater interactions between neighbouring molecules is taking place, for example ion pairing. The increased viscosity might also be a reason why conductivity does not increase further at high concentration, as mobility of species in the electrolyte is severely decreased.

In situ infrared data shows that there are changes in the structure of water and electrolytes with increasing concentration. The results showed that from the lowest concentration of $Li_2SO_4$ up to 1.8 M, the ions are somewhat independent of each other. When higher concentrations are reached, ionic interaction between sulfate and lithium occurs. This can be seen through the loss of symmetry of the sulphate leading to shifting, splitting and broadening of the sulphate asymmetric stretching band. Sulfate and lithium cations also work to trap the freedom of water due to their high solvating ability. This can be seen through changes to the water stretching bands that suggest changes in hydrogen-bonding. The changes were not linear with concentration indicating that at high concentration there is not full solvation of each ion and that ion pairing takes place.

Taking all of the information from the conductivity, viscosity and IR spectroscopy together suggests that up to about 1.0 M or 1.8 M the ions are relatively separately solvated and can move independently. As concentration increases there is more evidence that the ions being able to interact with each other and

are less fully solvated as there is insufficient free water available. In the next Chapters these solutions are used to study the kinetics of Fe dissolution and understanding of the solutions gained here will be used to explain the result.

# CHAPTER 4

# ELECTROCHEMICAL STUDIES OF THE DISSOLUTION OF IRON IN CONCENTRATED ELECTROLYTES

This chapter presents the results of two types of electrochemical measurements. First, the results of cyclic voltammetry measurements for the $Fe^0/Fe^{2+}$ redox reaction in different concentrations of lithium sulfate. Cyclic voltammetry was used to dissolve metal iron to form solvated Fe(II) in order to study the effect of electrolyte concentration on the dissolution rate of the iron electrode and try to understand the kinetics of the oxidation reaction that occurs. Secondly, the chronoamperometry method was applied to an iron electrode after it was immersed in different concentrations of lithium sulfate. That also helps us, in addition to cyclic voltammetry, understand the reaction kinetics of dissolved iron ions in this electrolyte.

The results of Raman spectroscopy of the iron electrode after being held at a certain potential are also presented. Raman spectroscopy of the iron electrode after oxidation used to see what species forms on the surface of the electrode, and whether there are competing interactions with the aqueous electrolyte. This may also be affected by the electrolyte concentration.

## 4.1. Previous studies of iron anodic dissolution

A number of studies have focused on studying the electrochemical dissolution of iron in different media, as discussed below. Most of the studies rely upon the mechanism proposed by Bockris and co-workers for interpretation of results.

Bockris et al suggested that iron dissolution in acidic media occurs through a sequential mechanism (non-catalytic mechanism)[62]. An adsorbing intermediate (FeOH) is formed in the initial step. The rate determining step is to discharge this intermediate and is referred to as (rds).

$$Fe^0 + H_2O \Leftrightarrow FeOH + H^+ + 2e^- \qquad (4.1)$$

$$FeOH \Leftrightarrow FeOH^+ + e^- \ (rds). \qquad (4.2)$$

$$FeOH^+ + H^+ \Leftrightarrow Fe^{2+} + H_2O. \qquad (4.3)$$

Hilbert *et al* [63]demonstrated the existence of two different mechanisms for the anodic decomposition of iron, which are a catalytic mechanism (Heusler) and a

noncatalytic mechanism (Bockris). Electron micrography was used to determine the atomic model of the two mechanisms. Both mechanisms have been shown to depend on the surface activity of the deposited iron through X-ray measurements and electrochemical experiments.

Podesta and Arvia[64] investigated the anodic dissolution of iron in sodium sulphate, sulphuric acid and ferrous sulphate by potentiostatic and galvanostatic techniques. The outcomes show that the most likely value of the Tafel slope at pH from 0 to 5 is 2.3 (2RT/3F) for the anodic reaction. The results were interpreted using the study of Bockris *et al*., who provided a comprehensive analysis of the kinetics of iron dissolution. These results are consistent with Bockris' theorem which states that the maximum overpotential should give a Tafel line with slope of RT/F.

Russell and Newman[65] precipitated ferrous sulphate crystals on the surface of the iron electrode in the form of a porous layer during anodic oxidation of an iron electrode. When the iron electrode was immersed in sulfuric acid solution, the dissolution rate of iron at the anode increased to the point of saturation. When the concentration of ferrous ions exceeds the saturation concentration of $FeSO_4$, ferrous crystals are deposited on the electrode surface. A mathematical formula was developed to study the deposited layer. Due to a decrease in ferrous ions adjacent to the electrode surface, the salt layer's thickness decreases over time.

Foroulis [66]used galvanostatic techniques to study the mechanism of iron oxidation at the anode in oxygenated and deoxygenated water. Another method was also used that depends on determining the anodic partial potential-current curve. The anodic Tafel slope was approximately 2.3RT/F in deaerated water and oxygenated water containing 0.25 mmol $O_2$/L. But in water with higher dissolved oxygen concentrations, the Tafel slope became about 2.3x(2/3) RT/F. The hypothesized results for the dissolution mechanisms in which the adsorbed Fe(OH) (Bockris mechanism) is involved were consistent with the results obtained for deoxygenated water and water containing 0.25 mmol $O_2$/liter. The results were interpreted for water with an oxygen content exceeding 0.25 mmol $O_2$/liter, on the basis of the hypothesis that there is a competition between dissolution and the formation of a passivation layer on iron.

The effect of hydrogen adsorption on the anodic dissolution of iron in acidic sulfate solution was studied by impedance spectroscopy[67]. It was found that when the amount of adsorbed hydrogen increased, the adsorption rate constants for dissolved iron decreased. This resulted in a decrease in the number of molecules adsorbed on the iron surface, and the solubility of the iron electrode decreased accordingly.

The type of iron and any impurities have been found to affect the anodic dissolution rate. Anodes containing different types of iron, such as white cast iron (WCI), gray cast iron (GCI), and pure iron, have been studied and their ability to produce ferrate (VI) in 10 M NaOH solution[68]. It was found that pure iron has the least electrochemical activity by using cyclic voltammetry and potentiodynamic polarization techniques. X-ray diffraction results of reaction products on WCI and GCI showed the presence of silicon in their outer layer in the form of iron(II) oxide and silicon(III) oxide-hydroxide.

It has also been shown that complexing ions in the electrolyte can affect the anodic dissolution rate. The effect of citric acid and pH on the anodic dissolution of iron were studied by Chu and Wan[69]. The results showed that the relationship between iron solubility and citric acid concentration is direct. The dissolution rate increases with increasing citric acid concentration due to the chelating bond between citrate ions and ferrous ions.

The anodic behavior of iron in sodium acetate solution at different concentrations (0.1-1.0 M) and near-neutral pH was studied using cyclic voltammetry[70]. The results showed that the acetate concentration affects the anodic behavior of iron, which indicates that it participates in the dissolution process or participates in the passivation process.

There are many studies on iron dissolution in addition to the above that highlight the importance of the electrolyte on the rate of reaction. This supports the need to study different electrolytes and the effect of their concentration as described in this chapter.

## 4.2. Experimental methods

Cyclic voltammetry was performed using a cell with three electrodes, an iron electrode (working electrode, WE), a platinum counter electrode (CE) and an Ag/AgCl reference electrode (RE) that were immersed in different electrolyte concentrations (0.1, 0.4, 1.0, 1.8, 2.0, 2.5 M $Li_2SO_4$). The potential window was chosen from -1.3 V to 0.1 V and then back to -1.3 V based on electrolyte stability. The potentiostat used in the experiment is EmStat3+ with the use of a program PSTrace 5 on the computer. The WE was Fe wire (purity 99.99%) from Alfa Aesar, 1 mm diameter. The iron electrode, which was 3 cm long, was prepared before the experiment by covering it with Teflon tape, leaving only the end of the electrode exposed (base is 1 mm diameter). The electrode was first cleaned with sandpaper, then washed with distilled water and dried.

In chronoamperometry, the current was measured for an iron electrode immersed in different concentrations of $Li_2SO_4$ for 750 s to observe steady-state current values. A potential of -0.4 V was applied because this is the potential at which the redox response begins in the CV measurements.

To prepare electrodes for investigation using Raman spectroscopy, chronoamperometry was initially applied to the iron electrode with different concentrations of $Li_2SO_4$ at -0.1 V which is the potential at which the oxidation process reaches its peak in CV measurements. Then Raman spectra of this electrode were recorded for 20 scans over the wavelength range 100 – 1300 $cm^{-1}$. A Renishaw inVia Raman Microscope with 514.5 nm laser was used, with WiRE2 spectral acquisition wizard.

## 4.3 Results and Discussion

### 4.3.1 Cyclic voltammetry of Fe electrode in $Li_2SO_4$ electrolyte

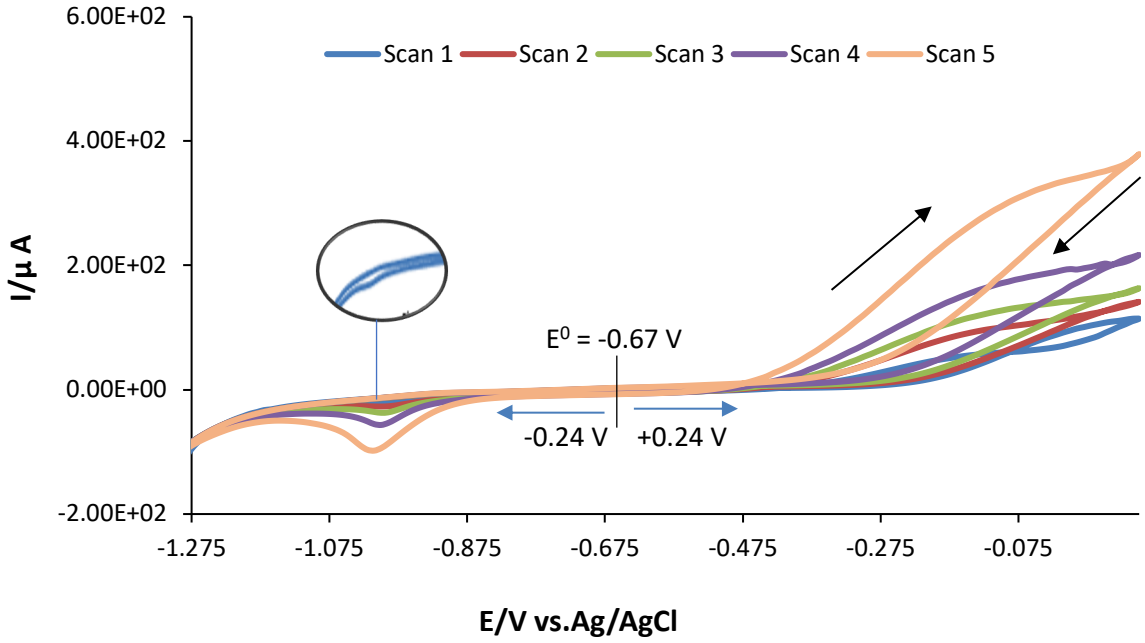


**Figure 4.1** Cyclic voltammetry at 0.05 $Vs^{-1}$ of iron electrode in 0.1 M $Li_2SO_4$.

In figure 4.1, cyclic voltammetry (CV) of an iron electrode in 0.1 M $Li_2SO_4$ is shown over 5 consecutive scans. The scan started from -1.3 V and was scanned towards 0.1 V. In the first scan (in blue), the oxidation current initially appears at -0.4 V and flows continuously until it reaches its maximum value at 0.1 V. The oxidation process can be expressed by equation (1.11).

On reversing the scan, oxidation current continues to flow in the range of 0.1 V to -0.4 V but does not follow the current of the forward scan i.e., it shows hysteresis. Then reduction current begins to be observed forming a small peak at -0.97 V attributed to the reaction in equation (1.9).

As scanning continues, the current increases, for example in the fifth scan (in orange), oxidation takes place at the same potential as the first scan (-0.4 V), but the current is greater. In addition, the current shows even more hysteresis during the oxidation reaction than the first scan, as well as a significant increase in the

reduction peak current. However, the potential of the reduction peak does not change much with repeated scanning.

Potentials at which currents flow in a CV can provide important information about the thermodynamics and kinetics of the redox reaction under investigation. The redox system reaches equilibrium quickly when the electron transfer kinetics are fast, but it will take a long time if the electron transfer kinetics are slow. As the standard potential for the reaction in equation (1.9) is $E^0$ = -0.44V vs SHE which is equivalent to -0.67 V vs Ag/AgCl, if the kinetics are fast, it is expected that oxidation and reduction will take place at -0.67 V as shown in figure 4.1. But note the oxidation starts at -0.4 V and the reduction starts at -0.88 V, so there is an overpotential of 0.24 V for both oxidation and reduction. This indicates that the kinetics are very slow.

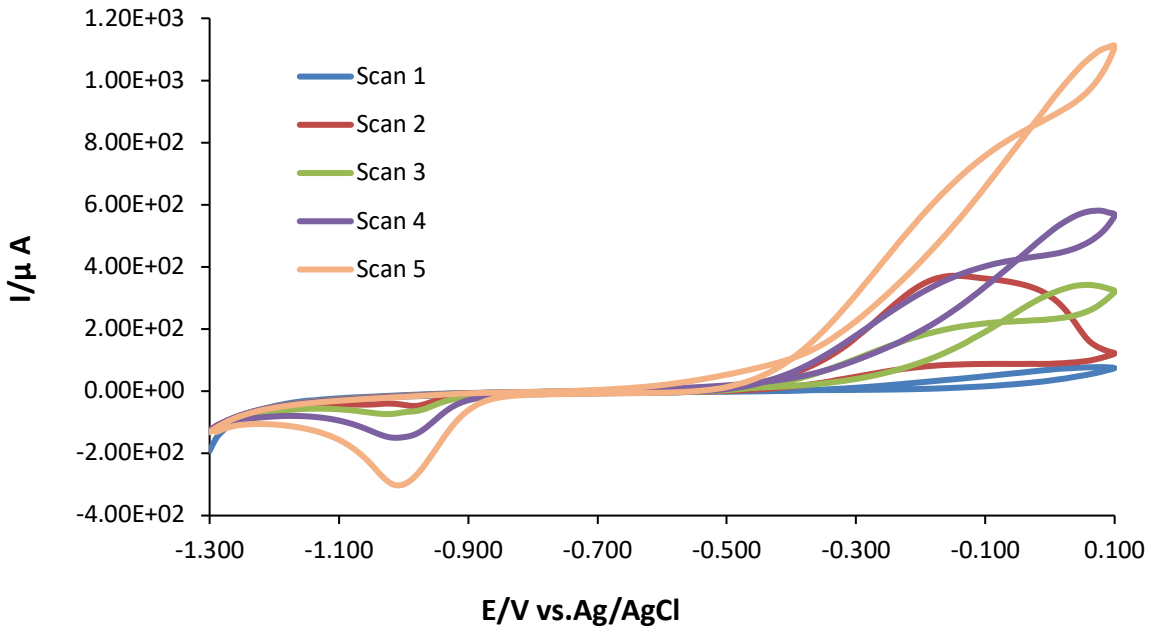


**Figure 4.2** Cyclic voltammetry at 0.05 $Vs^{-1}$ of iron electrode in 0.4 M $Li_2SO_4$.

In contrast, figure 4.2, illustrates different cyclic voltammetry results for an iron electrode in 0.4 M $Li_2SO_4$. In all scans, the oxidation starts to take place at -0.5 V. This is a more negative potential than oxidation was observed in 0.1 M $Li_2SO_4$. The current increases rapidly with scanning until it reaches a value higher than that observed for the lower concentration in figure 1 at 0.1 V. In addition, it is noted that the oxidation current shows more pronounced hysteresis and differs from the shape observed at a concentration of 0.1 M. The reduction peak at -0.99

V is formed for all scans when the scan is reversed. The height of the reduction peak increases with the number of scans for the same concentration, and has higher currents than the peak recorded at a concentration of 0.1 M.

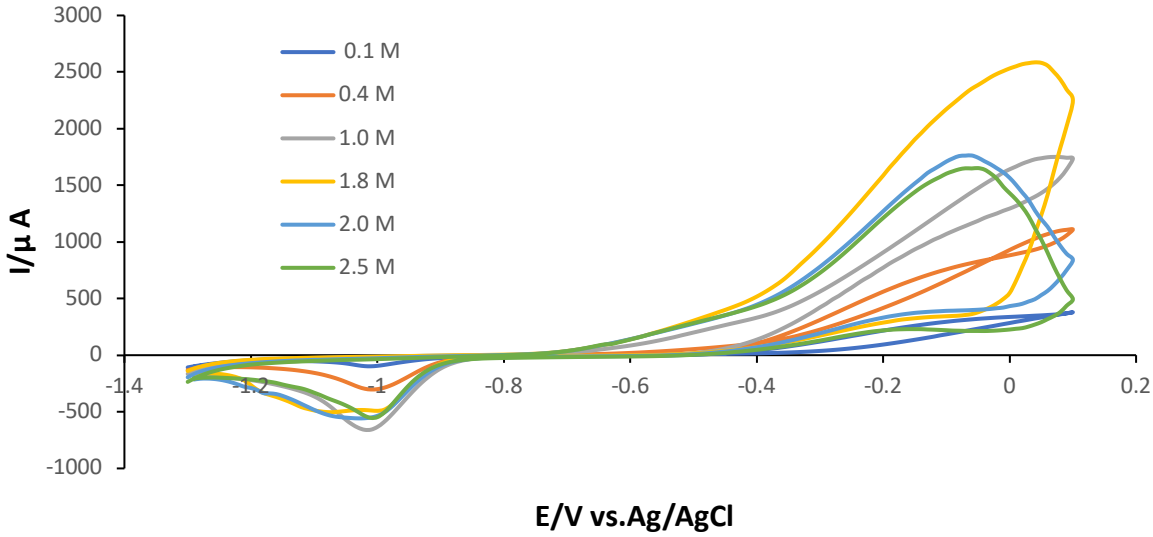


**Figure 4.3** Scan 5 of iron electrode in different concentration of $Li_2SO_4$ (0.1 M, 0.4 M, 1.0 M, 1.8 M, 2.0 M, 2.5 M) at scan rate 0.05 $Vs^{-1}$

To demonstrate the overall effect of electrolyte concentration on the Fe redox response, figure 4.3, shows an overlay of scan 5 for different concentrations of $Li_2SO_4$. As shown earlier, at a concentration of 0.1 M, the oxidation begins at -0.4 V and proceeds continuously until it reaches its maximum value at 0.1 V. At a concentration of 0.4 M, oxidation begins at -0.5 V. This is a more negative potential than the oxidation observed at 0.1 M. The reduction peak is formed at -0.97 and -0.99 V when the scan is reversed for concentrations of 0.1 M and 0.4 M, respectively, and the peak at concentration 0.4 is larger than that at concentration 0.1 M. At 1.0 M, we find that the oxidation process begins at -0.66 V, and this is a more negative potential than the oxidation observed at 0.4 M. The current increases rapidly and flows continuously until it reaches a value higher than that observed for the previous lower concentrations. In addition, there is a significant increase in the reduction peak current.

At 1.8 M, the oxidation current starts at -0.68 V and then reaches its highest value at 0.05 V. A broad reduction peak at -0.99 V is formed when the scan is reversed but is lower in height than the peak recorded at 1.0 M. At 2.0 and 2.5 M, the rate of iron dissolution (current) is lower than the rate at 1.8 M. The current starts at -

0.7 V and then decreases from its value at the concentration of 1.8 M until it reaches a peak. At 1.8M, 2.0 M and 2.5 M the oxidation response can be seen to be a peak, where current rapidly falls after reaching a maximum. This is different from the oxidation response seen at lower concentrations, where the current continued to increase until the potential was reversed. When the current stops increasing and drops very rapidly, this can often indicate that a competing reaction occurs that blocks the electrode surface and stops dissolution. This reaction will be discussed in detail later, but some research papers have suggested the formation of oxide or hydroxide layer occurs or the precipitation of a sulphate salt on the electrode surface.

To analyze the results in figure 4.3, the Pourbaix diagram (figure 1.3), which determines the direction of electrochemical processes and the equilibrium state of the metal in water at a given electrode potential and pH value, was used. Considering additional reactions involving sulfate ions ($SO_4^{2-}$) and their interaction with the Fe-$H_2O$ system.

According to the Pourbaix diagram, where pH = 7.4 (see red line), oxidation of Fe is predicted to occur at approximately -0.4 V, and iron is easily oxidized (equation 1.11) .

At 0.1 V, several reactions are expected to occur:

$Fe^{2+}$ oxidizes forming ferrous oxide. This oxide forms as a passivation layer on the electrode, suppressing the oxidation process and explaining the inhibited oxidation current.

$$2Fe^{2+} + 3H_2O \rightarrow Fe_2O_3 + 6H^+ + 2e^- \quad (4.4)$$

Or magnetite may form as a protective layer affected by the interaction of sulfate ions with iron.

$$Fe \leftrightarrow Fe_3O_4 \quad (4.5)$$

Ferrous ions in solution can form soluble complexes with sulfate ions.

$$Fe^{2+} + SO_4^{2-} \leftrightarrow FeSO_4 \quad (4.6)$$

Ferrous sulfate (hydrous forms such as $FeSO_4 \cdot 7H_2O$) can also precipitate.

$$Fe^{2+} + SO_4^{2-} + nH_2O \leftrightarrow FeSO_4 . nH_2O \text{ (solid).} \quad (4.7)$$

The Pourbaix diagram thus predicts that the formation of a passivation layer or precipitation will occur in the potential range used in CV experiments at pH = 7.4 However, the figure 4.3 shows that the oxide layer or precipitate on the electrode can form more readily in concentrated electrolytes than dilute electrolytes.

Figure 4.4 shows the fall in dissolution rate more clearly, as current for Fe oxidation at -0.4 V has been plotted against concentration of the $Li_2SO_4$ electrolyte. This shows an initial increase in the current as concentration of electrolyte is increased from 0.1 to 1.8 M, followed by a decrease and levelling off at higher electrolyte concentrations.

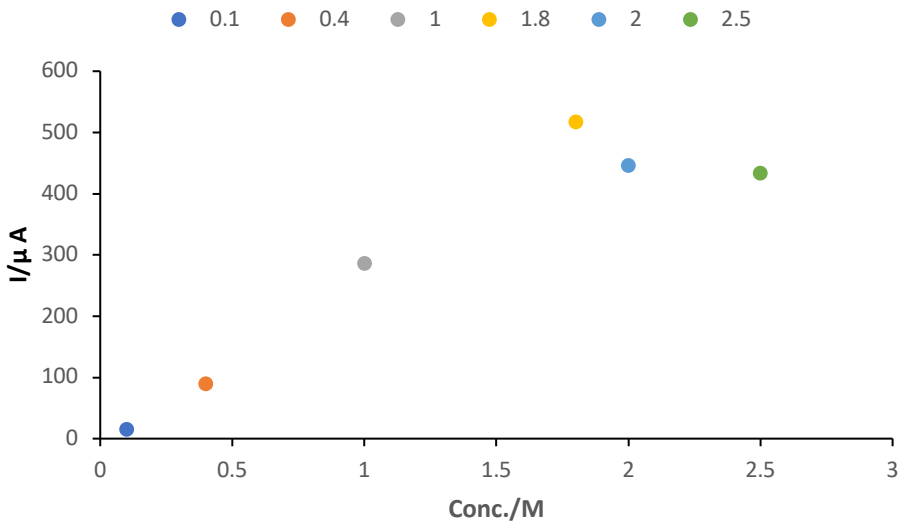


**Figure 4.4**The relationship between maximum current from scan 5 at -0.4 V with concentrations of $Li_2SO_4$.

As the onset potential for oxidation is indicative of the kinetics of electron transfer, we can see that as concentration of $Li_2SO_4$ increases, the kinetics of $Fe \rightarrow Fe^{2+} + 2e^-$ becomes faster and oxidation becomes easier as it starts at a more negative potential. The increase in oxidation current from 0.1 to 1.8 M also indicates that the rate of $Fe \rightarrow Fe^{2+} + 2e^-$ becomes faster. However, at concentrations of 2 M and above the maximum current achieved begins to fall, indicating that the kinetics for the reaction have reached a maximum or that other processes are limiting the rate of reaction. This is investigated further using chronoamperometry in the next section.

### 4.3.2 Chronoamperometry of Fe electrode in $Li_2SO_4$ electrolytes

A chronoamperometry method involves applying a potential to a working electrode and measuring the current flowing through that electrode over time. For the measurements shown in figure 4.5, the iron electrode was placed in different concentrations of $Li_2SO_4$ and a potential of -0.4 V applied because this is the voltage at which the oxidation response begins in the CV measurements, and current was measured for 750 seconds.

With 0.1 M $Li_2SO_4$, the current increased slowly at the beginning of the experiment, then stabilized over a period of 200 to 300 seconds and then gradually increased until it reached its maximum current at 750 seconds. The maximum current at 750 s increases with electrolyte concentration for 0.4 and 1.0 and 1.8 M $Li_2SO_4$. The current achieved in 1.8 M $Li_2SO_4$ is approximately 1.4 times that at 0.1 M $Li_2SO_4$. On the other hand, when moving to high concentrations of 2 and 2.5 M, the current records lower values than at a concentration of 1.8 M at 750 seconds.

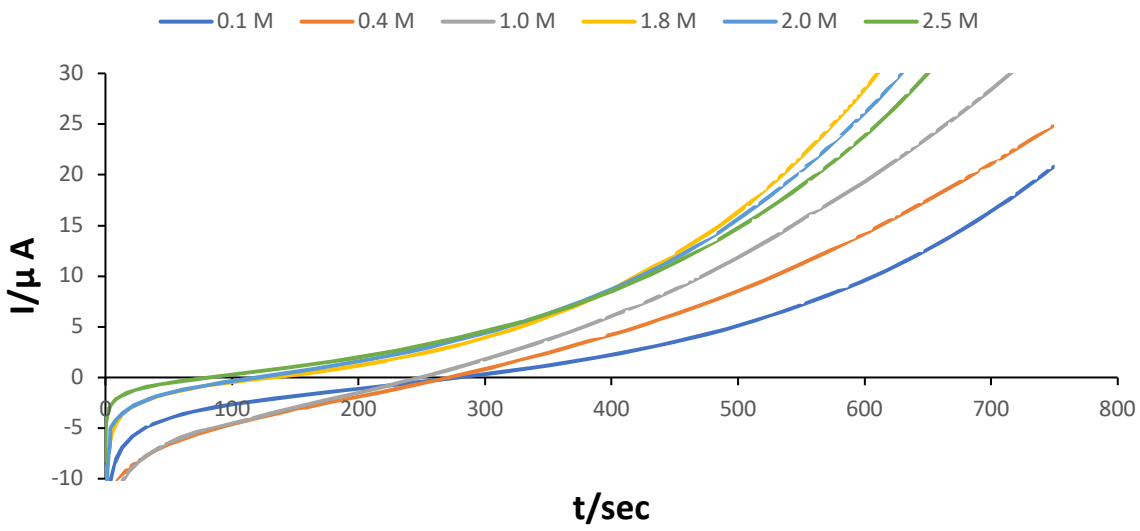


**Figure 4.5** Chronoamperometry performed at - 0.4 V of iron electrode in different concentrations of $Li_2SO_4$

### 4.3.3 Discussion of CV and chronoamperometry results and relation to solution conductivity and viscosity properties

Upon comparing the results of cyclic voltammetry and chronoamperometry of lithium sulphate solutions with various concentrations, we found that when the concentration of $Li_2SO_4$ increases from 0.1 to 1.8 M in both methods, iron dissolution becomes faster and the current increases according to reaction in equation (1.11).

The dissolution of iron and the value of the current decreases at 2.0 M and above. CV also indicates that the current has become passivated, and that there are potentially competing reactions in the medium that reduce the reaction rate.

CV and chronoamperometry results will now be compared with electrolyte properties such as conductivity and viscosity (introduced in Chapter 3) to gain a better understanding of the results.

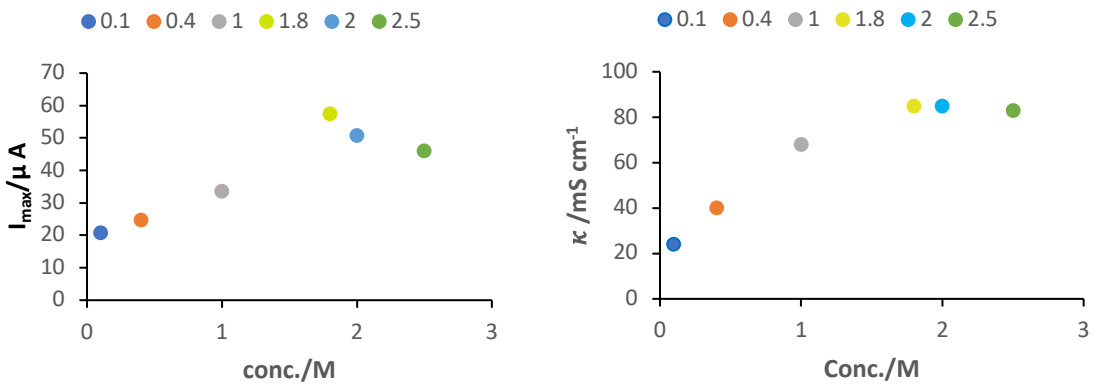


**Figure 4.6** The relationship between a) max current of Fe dissolution (from CV scan 5) in different concentrations of $Li_2SO_4$ b) conductivity of $Li_2SO_4$ as a function of concentration (from Chapter 3).

Figure (4.6,a) shows that the maximum current increases with increasing concentration until it reaches its maximum value at 1.8 M. Thereafter, the maximum current decreases with increasing concentration up to 2.0 M and above. Figure (4.6,b) shows that the conductivity increases gradually from 0.1 to 1.8 M, after which it stabilizes at 2 and 2.5 M. In other words, when the electrolyte conductivity increases due to the presence of more charged ions, the current due to the dissolving of iron also increases. Hence the increase in conductivity may

aid the dissolution of the iron. When concentrations exceed 1.8 M, there is no change in conductivity values, perhaps due to the presence of more uncharged ion pairs in solution. This could be a reason that the current for iron dissolution does not further increase when the electrolyte concentration is above 2 M. It does not however explain why the current for iron dissolution decreases or why current passivation is observed in the CV response at these concentrations.

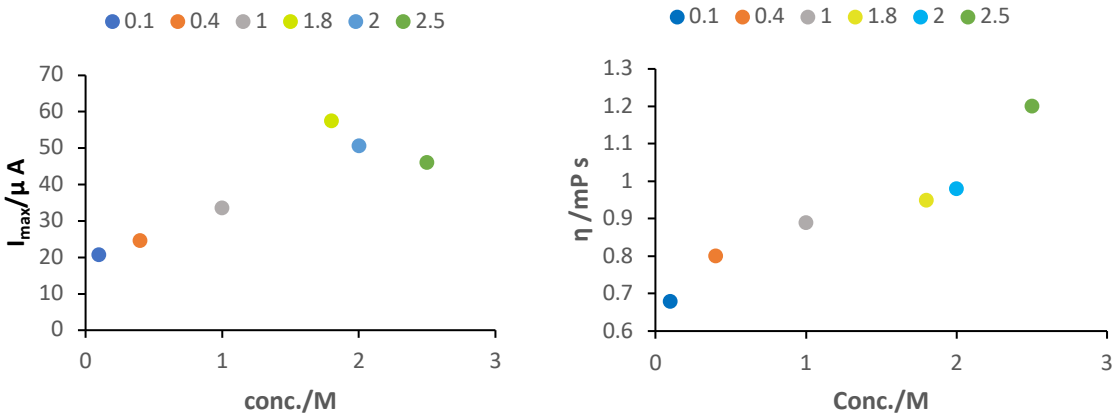


**Figure 4.7** The relationship between a) max current of Fe dissolution (from CV scan 5) in different concentrations of $Li_2SO_4$ b) viscosity of $Li_2SO_4$ as a function of concentration (from Chapter 3).

Figure (4.7,a), again shows the maximum oxidation current for Fe dissolution as a function of electrolyte concentration. The figure (4.7,b) shows the viscosity determined over the same concentration range and shows it increases significantly with increasing concentration from 0.1 to 2.5, where it reaches its maximum value. Increased viscosity usually decreases currents for diffusing species, as they are slowed by increased friction between the solution molecules. In this case, the reacting species is metallic Fe so the reaction rate is less likely to be slowed by the increasing viscosity and that is what is seen up to concentrations of 1.8 M. The diffusion of the Fe(II) product away from the electrode will become more difficult as the viscosity of the solution increases. This could lead to a supersaturation of the solution, with high concentrations of Fe(II) near the electrode surface, leading to precipitation of Fe sulfates, oxides or hydroxides if the solubility limit is reached. This could explain the sudden drop in

the oxidation current and observed passivation. This is explored further in the next section.

The effect of sodium acetate concentration on iron dissolution has been studied previously with some results that are similar to those observed in this work on $Li_2SO_4$. The effect of sodium acetate at a concentration of 1 M on dissolving the iron electrode in an almost neutral aqueous medium with a pH ranging from 5 to 7 was studied [70]. It was found that the acetate concentration affects the anodic behavior of iron, indicating that it participates in the process of iron dissolution through the formation of soluble Fe(II) species or participates in the formation of the passivation layer by binding acetate to iron ions to form a film on the surface. As the acetate concentration increased, the formation of the passivation layer became easier. Using a cyclic voltammetry technique, two anodic peaks were formed during positive scanning. During reverse scanning, the current in the two anodic peaks decreases with increasing pH. These results suggested that competitive processes occur: on the one hand the onset of film formation and on the other hand the dissolution of iron. The results of the research are consistent with the results of this research at a concentration higher than 1.8 M of $Li_2SO_4$ and a pH = 7.4. It was found that the decrease in current indicates the beginning of the formation of the passivation layer, which consists of insoluble species such as iron hydroxide / iron oxyhydroxide.

Another study[65] showed that ferrous sulfate was deposited on the surface of the iron electrode undergoing oxidation in sulphuric acid electrolytes. Precipitation occurs when the concentration of iron ions next to the electrode exceeds the saturation value of ferrous sulfate. The thickness of the deposition layer decreases when all the iron ions are consumed from the solution adjacent to the electrode surface.

### 4.3.4. Raman spectroscopy of the Fe surface after anodic dissolution

The Raman spectroscopy method can provide information about solid oxides or other species present on the surface by comparison with spectra in previous studies. If the passivation discussed above is due to film formation, Raman will help determine the composition of the film.

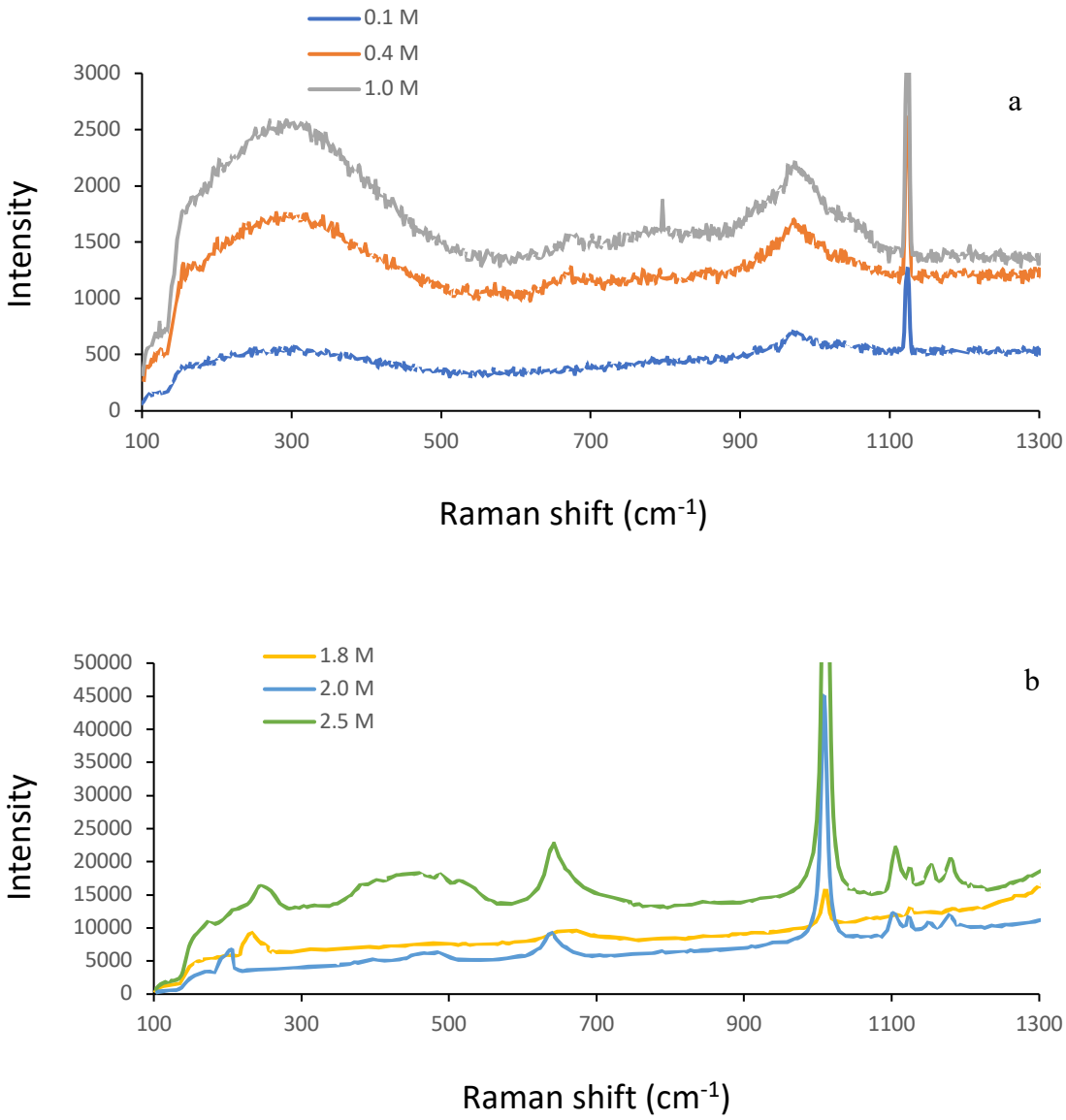


**Figure 4.8** Raman spectrum of iron electrode previously treated by chronoamperometry in a) lower concentrations b) higher concentrations of $Li_2SO_4$ at -0.1 V.

The Raman spectra shown in Figure 4.8 were recorded for the iron electrodes that have previously undergone chronoamperometry at -0.1 V in different concentration $Li_2SO_4$ solutions. This is in order to observe the changes that occur for the electrode at - 0.1 V when the passivation reaction is observed at higher electrolyte concentrations.

In figure (4.8,a) the Raman spectra of iron electrodes in 0.1 M (blue), 0.4 M (orange) and 1.0 M (gray) $Li_2SO_4$ show relatively few features, but there are two small and broad peaks at 285 and 975 $cm^{-1}$. The sharp peak at 1130 $cm^{-1}$ is the result of background interference from room lighting.

In figure (4.8,b) the Raman spectrum after cycling in 1.8 M electrolyte (yellow) shows a slight peak at low wavenumbers of 234 $cm^{-1}$, followed by a sharp peak at 1008 $cm^{-1}$. At high concentrations of 2.0 M (light blue) and 2.5 M (green) electrolyte, the spectra show a small peak at a low wavenumber of 199 and 250 $cm^{-1}$, respectively, followed by two clear peaks at 473 and 640 $cm^{-1}$ for 2 M and 470 and 644 $cm^{-1}$ for 2.5 M. The strong peak appears at 1003 and 1011 $cm^{-1}$ for 2 and 2.5 M respectively, followed by sequential small peaks from 1105 to 1182 $cm^{-1}$.

The results are consistent with the CV results that show the rate of iron dissolution increases and the current resulting from this reaction increases from 0.1 to 1.8 M. There is no indication that the reaction is slowed by the formation of a film on the electrode and indeed Raman spectra for the electrode in lower concentration solutions show very few peaks. At 2.0 and 2.5 M, we noticed the reaction stopped and the current became passive. The formation of a solid species on the electrode from 1.8 M onwards is confirmed by the results of the Raman spectroscopy.

Comparison with literature allows the peaks to be assigned to specific surface species present in the film. As we know, free sulfate $SO_4^{2-}$ has four basic vibration modes and is active in Raman. These modes are $\nu_1$ (983 $cm^{-1}$, symmetric stretching), $\nu_2$ (450 $cm^{-1}$, symmetric bending), $\nu_3$ (1105 $cm^{-1}$, asymmetric stretching) and $\nu_4$ (611 $cm^{-1}$, asymmetric bending) [71]. Table 4.1 summarises the Raman spectrum results from Figure 4.8 above and those of previous studies of iron sulphate materials, which appear to be very similar. This allows us to propose that the passivation film on the iron electrode is likely to be iron sulphate.

The peaks at 976 to 1011 $cm^{-1}$ at all concentrations indicate the symmetric vibrational mode ($\nu_1$) of $SO_4^{2-}$, which gives sharp and intense Raman lines. Some research suggests $\nu_1$ shows a decrease in wavenumber as the number of water molecules associated with the structure increased. This means that the compound hepta-, tetra-, and monohydrates of $FeSO_4$ record the $\nu_1$ peak at the following wavenumbers 976, 990 and 1018 $cm^{-1}$, respectively. This is consistent with the results of this research, as we find that at low concentrations of electrolyte the wavenumber for the sulphate is 975 $cm^{-1}$ and increases until it

reaches 1013 $cm^{-1}$ at higher electrolyte concentrations where there is less water available to incorporate into the solid material.

Peaks were observed for the asymmetric vibrational mode region ($\nu_3$) of $SO_4^{2-}$ at 1105 –1182 $cm^{-1}$, which was split into four Raman lines at concentrations of 2 and 2.5 M. This results from decreased symmetry of the sulphate and indicates a range of bonding environments. Symmetrical $\nu_2$ $SO_4^{2-}$ bending modes appear only at concentrations 2 and 2.5 M at about 470 $cm^{-1}$. As for the asymmetric bending of $\nu_4$ $SO_4^{2-}$, it appears for all concentrations at 640 - 670 $cm^{-1}$ except for the concentration of 0.1 M.

Taken together the Raman peaks show that iron sulfate deposits significantly on the electrode surface where the concentration of $Fe^{2+}$ and $SO_4^{2-}$ are high adjacent to the electrode surface. When the upper limit of iron sulfate saturation is reached, sulfate is deposited on the electrode, thus creating a passivation layer on the surface. There may also be some oxide or hydroxide species deposited on the electrode surface in the higher concentration solutions, but this is not clear from the Raman results. It would be expected that such species are formed at higher potentials than used in this study.

**Table 4.1** Raman bands of some compounds of iron electrode in different concentrations for $Li_2SO_4$ .

| species | Raman spectrum | | | | | | | |
|---|---|---|---|---|---|---|---|---|
| | Absorption wavenumber $cm^{-1}$ | | | | | | | |
| | This work | | | | | | Literature Data | References |
| | 0.1 M | 0.4 M | 1.0 M | 1.8 M | 2.0 M | 2.5 M | | |
| $\nu_1(SO_4)$ | 975 | 975 | 975 | 1008 | 1003 | 1011 | 995-1013<br>976-1018 | [71]<br>[72] |
| $\nu_3(SO_4)$ | 1125 | 1128 | 1128 | 1125 | 1105<br>1125<br>1152<br>1180 | 1105<br>1125<br>1155<br>1182 | 1024-1250<br>1071-1194 | [71]<br>[72] |
| $\nu_2(SO_4)$ | - | - | - | - | 473 | 470 | 438-536<br>423-492 | [71]<br>[72] |
| $\nu_4(SO_4)$ | - | 670 | 670 | 670 | 640 | 644 | 600-624<br>565-661 | [71]<br>[72] |
| F-S | 285 | 285 | 285 | 234 | 199 | 250 | 283 | [73] |

## 4.4 Conclusion

The results of electrochemical measurements and Raman spectroscopy of iron dissolution in different concentrations of lithium sulfate showed great agreement. At lower concentrations (from 0.1 M up to 1.8 M), the iron dissolution rate increases with electrolyte concentration and the reaction is fast, according to the results of the CV and chronoamperometry measurements. The reason is the low viscosity, facilitating the movement of ions due to the lack of friction between them. In addition, to the abundance of water molecules, which helps facilitate the movement of ions. The high conductivity of the solution in this concentration range is also an advantage, allowing the sulphate ions to help the dissolution of $Fe^{2+}$. This result was reinforced by the results of Raman spectroscopy, where weak peaks appeared for electrodes used in this concentration range, indicating that no precipitation occurred on the iron electrode.

At high concentrations (2.0 M and above), the CV results found that the iron dissolution reaction stops, and the current is passive. This was confirmed by the results of chronoamperometry, as the current resulting from the dissolution of the iron decreases with time. Raman spectroscopy results showed that the reason for the decrease in the iron dissolution rate is due to the deposition of iron sulphate on the iron electrode through the recorded peaks of sulphate with different vibrational modes. Through these experiments, it was found that concentrations of $Li_2SO_4$ above 1.8 M hinder the dissolution of iron and therefore are not a good choice to use in applications such as all-iron redox flow cells. At concentrations below 1.8 M there may be some advantages in using higher salt concentrations due to the higher conductivity and not too high viscosity.

# CHAPTER 5

# IN SITU INFRARED SPECTROELECTROCHEMISTRY OF IRON ELECTRODE INTERFACE

This chapter presents the results of infrared (IR) spectroscopy near the surface of an iron electrode with different concentrations of $Li_2SO_4$ electrolyte after applying a potential. The results of IR can give us information about the changes to water and electrolyte structure at potentials at which Fe dissolution takes place. This method is expected to clarify the effect of electrolyte concentration on the kinetics of iron stripping. The infrared results are then compared with the results of cyclic voltammetry and Raman spectroscopy, which were presented in Chapter 4.

## 5.1 Experimental methods

In order to begin the experiment, the electrolyte is placed in the electrochemical cell that was clamped above the ATR prism (see Chapter 2 section 2.2.3 for a diagram and description of the experimental set-up). The electrodes were placed in the cell, with the Fe working electrode being located directly above the prism so that the electrode interface is being probed by the IR evanescent wave. A background spectrum was then recorded. Background spectrum refers to the electrolyte (water with the ion dissolved in it) at the electrode surface but with no applied potential. A potential of -0.4 V was applied and spectra repeatedly measured for 30 min at intervals of 5 min. The spectra reported in this Chapter are difference spectra as they are relative to a background spectrum without the potential applied. Hence, they show how the potential affects the IR spectrum of the electrolyte at the electrode surface.

## 5.2. IR Spectroscopy: Results and Discussion

### 5.2.1. IR difference spectra at -0.4 V

The IR difference spectra in figures 34-37 show the changes in absorbance when potential -0.4 V was applied to Fe electrode in different concentrations of $Li_2SO_4$. As the oxidation process starts at this potential in CV, -0.4 V was selected. It is expected that the iron is undergoing anodic dissolution at this potential but at a

relatively slow rate. This potential is also quite far negative of where the current passivation was observed in the CV experiments in Chapter 4.

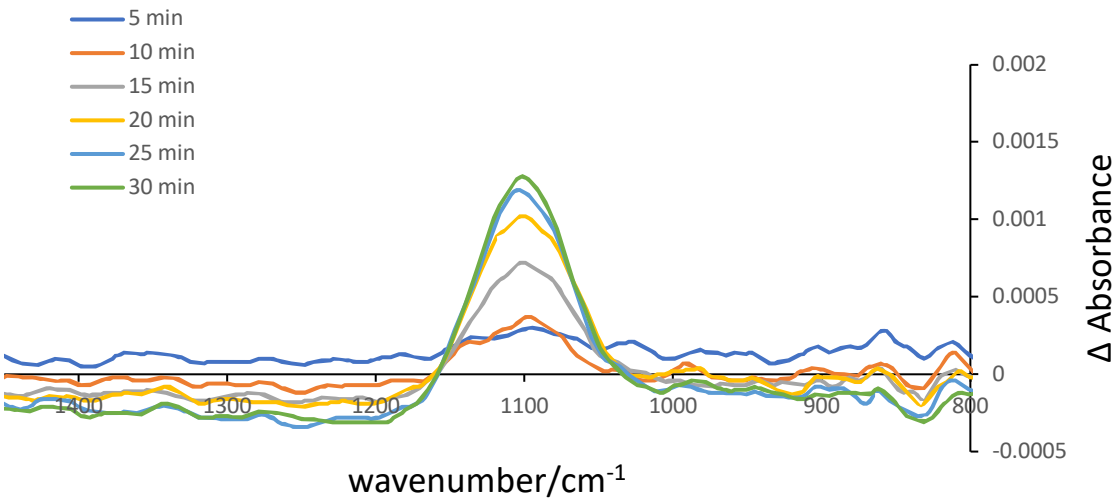


**Figure 5.1** Infrared spectrum of iron electrode in 0.1 M $Li_2SO_4$ at -0.4 V.

The IR difference spectra in figure 5.1 shows the changes in the absorbance peaks when potential -0.4 V was applied to the Fe electrode with a concentration of 0.1 M $Li_2SO_4$ over a period of 30 minutes in the wavenumber ranges from 800 $cm^{-1}$ to 1400 $cm^{-1}$. A small symmetric peak appears at 1093$cm^{-1}$ resulting from the asymmetric infrared stretching mode of $SO_4^{-2}$. The absorption increases with increasing time after application of the potential.

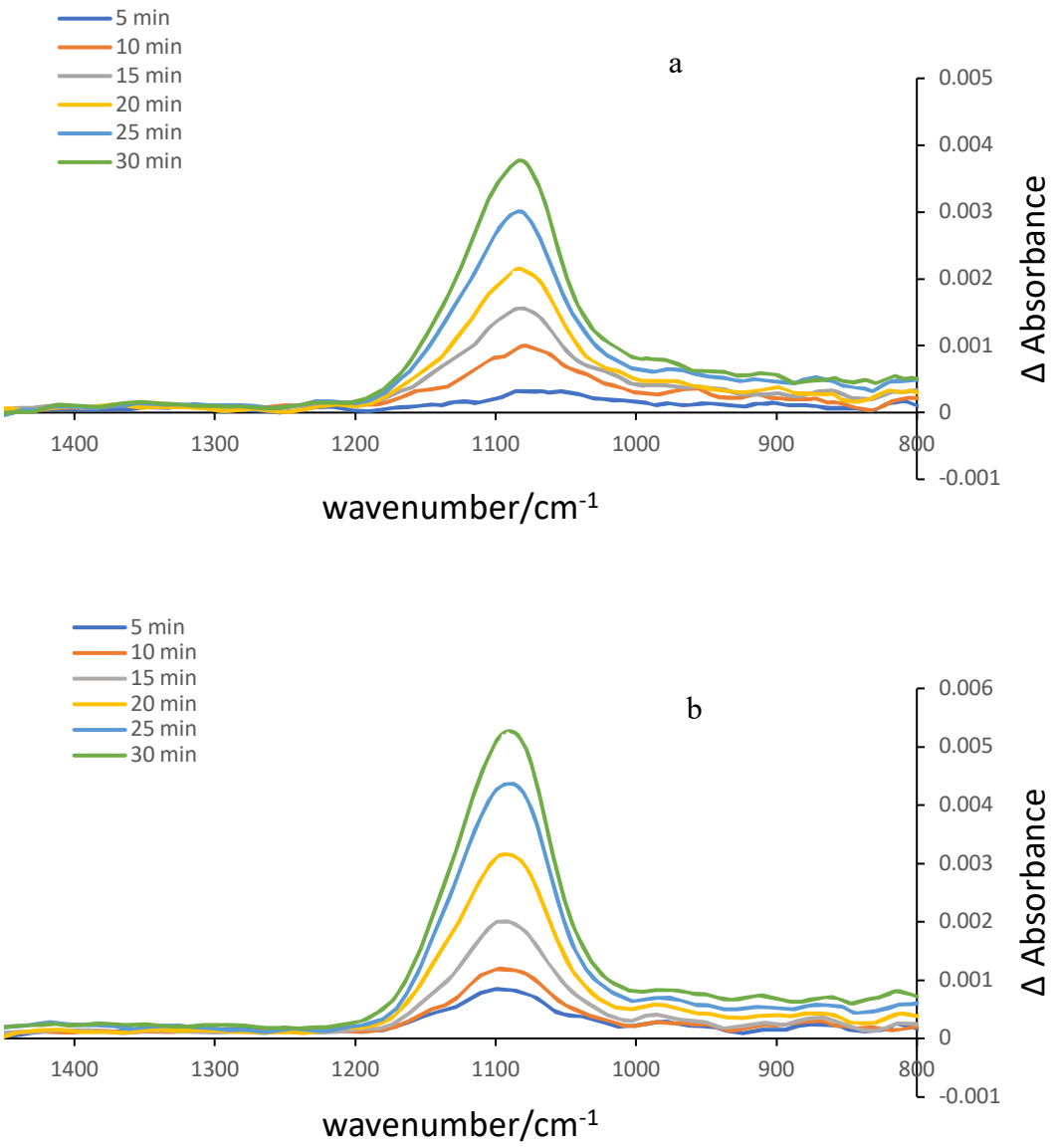


**Figure 5.2** Infrared spectrum of iron electrode in a) 0.4 M b)1.0 M of $Li_2SO_4$ at -0.4 V.

In Figure 5.2 (a,b), the absorption difference spectra of the iron electrode are shown for 0.4 and 1.0 M, respectively. At 1080 $cm^{-1}$ a sharp peak appears for both concentrations, which increases in intensity with increasing time. The absorption intensity at 1.0 M is greater than that at 0.4 M over the same time periods. The peak is less symmetric than observed in 0.1 M electrolyte with some broadening to the higher wavenumber side.

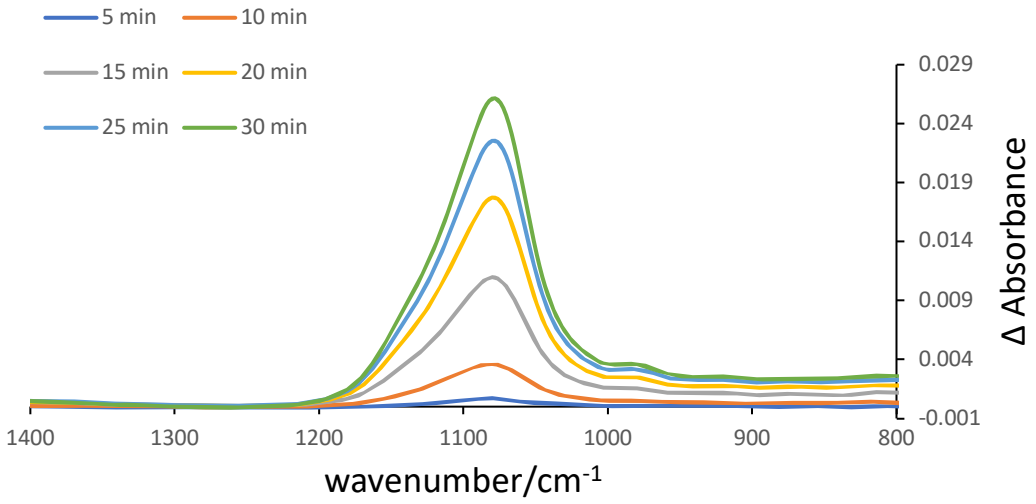


**Figure 5.3** Infrared spectrum of iron electrode in 1.8 M $Li_2SO_4$ at -0.4 V.

Figure 5.3 shows a sharp peak at 1076 $cm^{-1}$ for the experiment using 1.8 M $Li_2SO_4$. The height of this peak increases with. Increasing number of scans. The intensity of this peak at 1.8 M is greater than at lower concentrations. In addition, a new absorption feature starts to emerge at 980 $cm^{-1}$ that increases in intensity with time. The maximum stretching frequency of $SO_4^{-2}$ changes from 1093 - 1080 $cm^{-1}$ at low concentrations to 1076 $cm^{-1}$ at 1.8 M concentration. The peak also becomes even less symmetric, with a significant broadening to the higher wavenumber side of the peak.

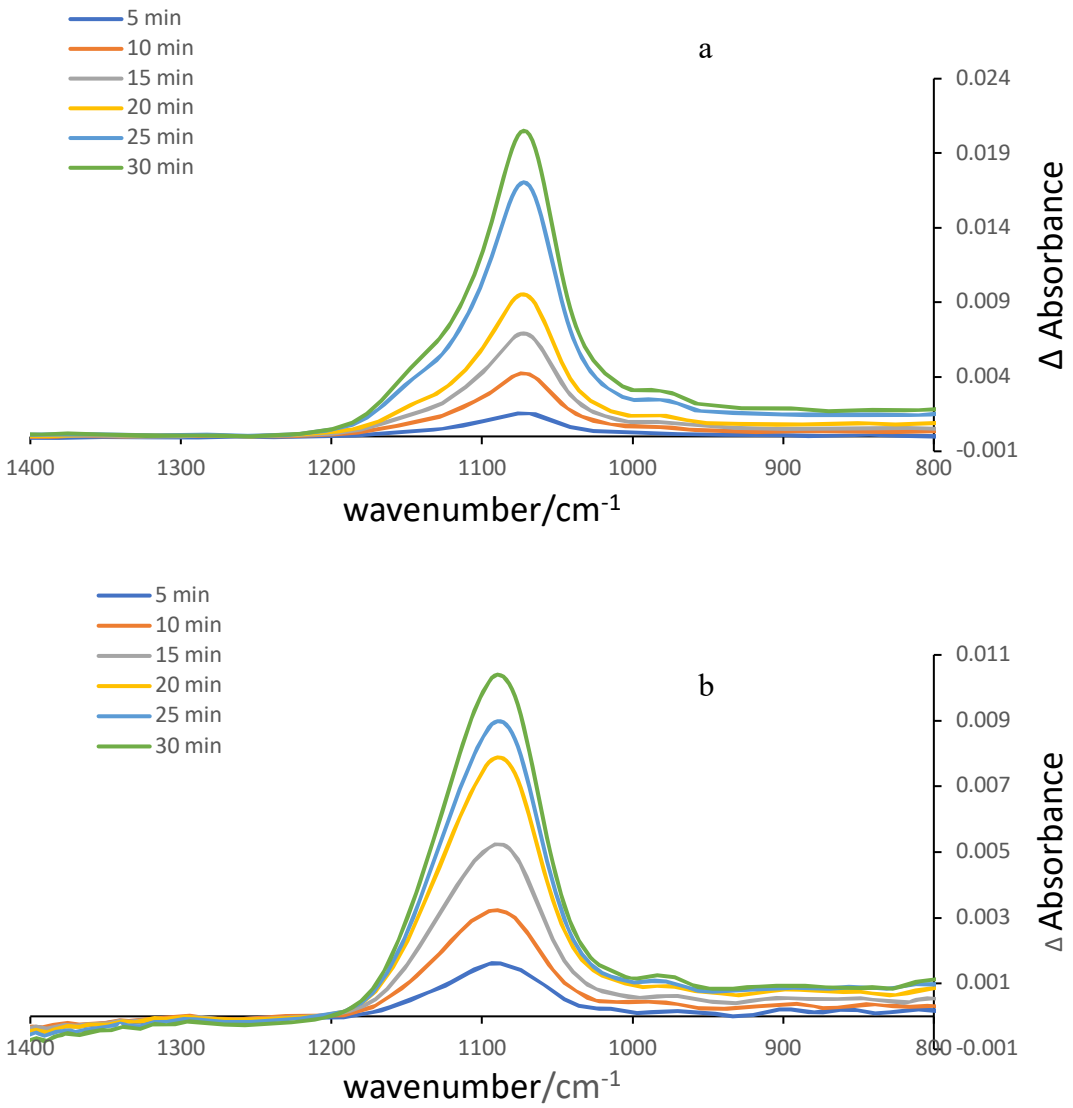


**Figure 5.4** Infrared spectrum of iron electrode in a) 2.0 M b) 2.5 M of $Li_2SO_4$ at -0.4 V.

Figure 5.4(a,b) shows a sharp asymmetric peak at 1076 and 1080 $cm^{-1}$ for concentrations 2 and 2.5 M, respectively, the intensity of which increases with increasing time. There is a very clear shoulder to the higher wavenumber side of the peak for the 2.0 M solution. The peak intensities are smaller for the 2.0 and 2.5 M solutions, compared to the same peak in the 1.8 M solution. In addition, there is a small broad peak at 980 $cm^{-1}$.

The infrared experiments were repeated on a later occasion for the same range of electrolyte concentrations as above and the same trends were observed (see Appendix). Across experiments the intensity of the sulfate absorption peak increases from 0.1 to 1.8 M, then the intensity decreases at

2.0 M and above. The same asymmetry on the peaks was observed as the concentration increased. The absolute values of ΔAbs was different between the two sets of experiments, as this value depends on factors such as position of Fe electrode on the prism and distance between the electrode surface and the prism. It is difficult to locate the electrode in exactly the same position for all experiments. The strength of the IR signal for the instrument can also change depending on background humidity in the instrument and age of the IR source. Hence comparing trends between data sets is more important than determining an average value.

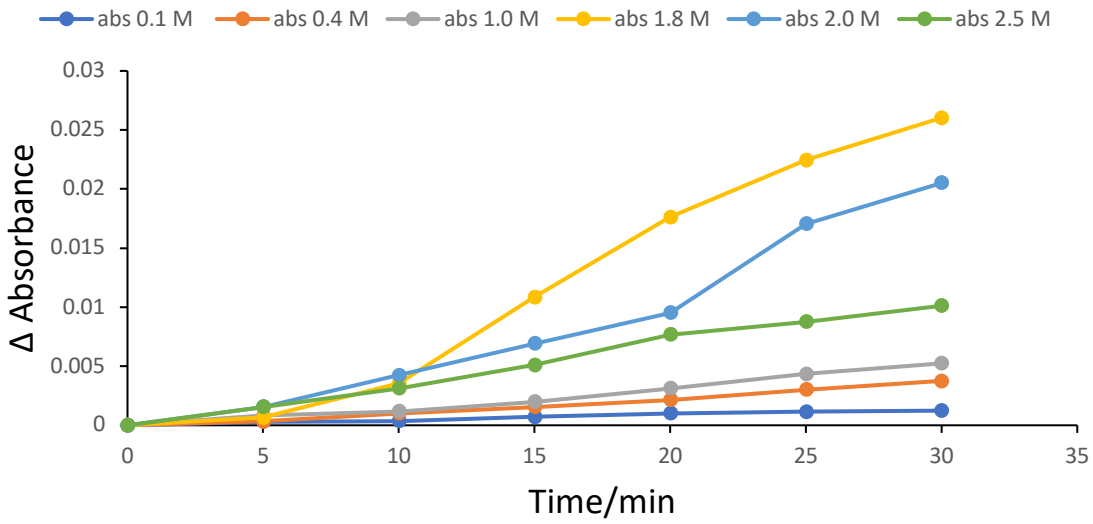


**Figure 5.5** The relationship between the maximum ΔAbsorbance of the asymmetric $SO_4^{2-}$ stretch peak at the iron electrode surface for different concentrations of $Li_2SO_4$ with time.

As shown in Figure 5.5, the relationship between the peak maximum of all spectra was plotted for each concentration against time. At concentrations of 0.1, 0.4 and 1 M, there was a gradual increase in the maximum sulfate peak from 5 to 30 minutes. At a concentration of 1.8 M, a gradual increase occurs from 5 to 10 minutes, followed by a sharper increase after 10 minutes until the end of the time period. At 2 M, there is no difference in peak values from the values at 1.8 M during the first 10 minutes. A gradual decrease occurs over the next ten minutes, followed by a gradual rise in the last ten minutes, but it is less than the values at 1.8 M. There is a gradual decrease in peak values during the first 20 minutes, then their values stabilize during the last 10 minutes.

### 5.2.2 Discussion of IR difference spectra results

Clearly the results show an increase in the concentration of sulphate ions in the region close to the electrode when the -0.4 V potential is applied. The concentration of sulphate increases with time after application of the potential. It is proposed that this is due to the electrode dissolution process (oxidation process), resulting in an increase in $Fe^{2+}$ ions in the solution near the electrode, which attracts $SO_4^{-2}$ ions to neutralise the charge locally. Therefore, the higher the concentration of $Fe^{2+}$ ions near the electrode, the higher the local concentration of sulphate, as the in situ IR technique measures absorption changes in the solution close to the surface of the Fe electrode.

However, at 2.0 and 2.5 M, the concentration of $Fe^{2+}$ and $SO_4^{2-}$ is high near the electrode surface. When the upper limit of iron sulfate saturation is reached, sulfate is deposited on the electrode, thus creating a passivation layer on the surface. The solubility of the iron electrode decreases, and the amount of sulfate ions needed for neutralization decreases. Hence the sulphate peak is smaller for 2.0 M and 2.5 M than at lower concentrations.

In the asymmetric stretching range at 1050-1250 $cm^{-1}$, we notice that with increasing concentration, a broadening of the peak occurs with an increase in the wavenumber due to the interaction of the sulfate ion with the ions surrounding it, which makes it lose its symmetry and loses its degeneracy. This causes the infrared band to become asymmetric and appear split and broadened. There is also a shift in the stretching frequency of $SO_4^{-2}$ from 1093 $cm^{-1}$ at 0.1 M to 1080 $cm^{-1}$ at 2.5 M due to the effect of the electric field resulting from the interaction of $SO_4^{-2}$ with its surrounding highly concentrated ionic environment (Stark effect). A peak also occurs at 980 $cm^{-1}$ and this is the inactive IR symmetric stretching which is now allowed in part due to loss of symmetry as a result of increased intermolecular interactions between the sulfate ion and other species in solution. Taken together these spectral features demonstrate the very strong interactions between the neighbouring ions in these concentrated solutions.

### 5.2.3. IR difference spectra at different applied potentials

In figure 5.6, the infrared difference spectra show the changes in absorption when four different potentials (-0.2, -0.4, -0.6, -1.0 V) are applied to the Fe electrode in 1.4 M $Li_2SO_4$. This experiment was conducted to demonstrate that the increase in sulphate absorption peak (and hence increase in sulphate concentration) is directly related to $Fe^{2+}$ concentration at the electrode surface.

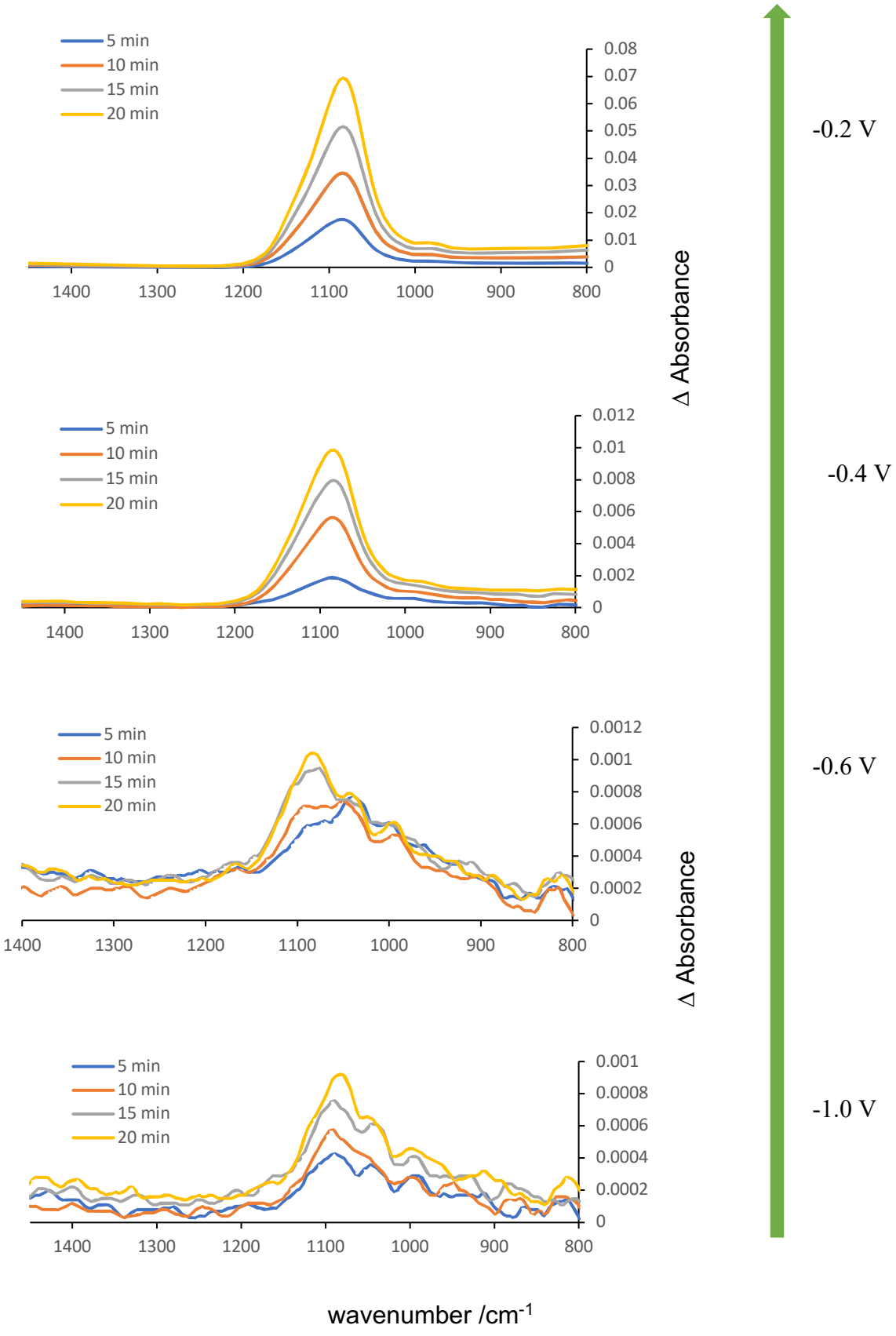


**Figure 5.6** Infrared spectrum of iron electrode in 1.4 M of $Li_2SO_4$ at different potentials.

In general, it can be seen that the sulfate peak increases in height as the potential becomes more positive. After 20 mins at -1.0 V ∆Abs is 0.0009, after 20 mins at -0.6 V Δ Abs is 0.00103, after 20 mins at -0.4 V ΔAbs is 0.00962 and after 20 mins at -0.2 V Δ Abs is 0.0681.

From these values we notice that the changes in absorbance for sulfate at -1.0 V and -0.6 V is very small, as it is ten times smaller than the change in absorption values at -0.4 V. This indicates that at -1.0 V and -0.6 V the amount of sulfate ions close to the surface of the iron electrode is very small. The reason for this is the very low amount of dissolved $Fe^{2+}$ near the electrode surface at these potentials, due to the oxidation reaction and dissolution of the iron not being feasible at this potential. In fact, at -1.0 V the process of reduction of $Fe^{2+}$ to iron occurs (equation (1.9)).

Consequently, the concentration of $Fe^{2+}$ in the solution decreases and the requirement for sulphate as a counter ion decreases. This results in a lack of sulfate ions coming to neutralize the iron ions near the electrode, and thus the absorption peak for sulphate in the IR spectrum is almost negligible.

As we explained previously, at a -0.4 V, the process of oxidation and dissolution of iron into iron ions begins according to the equation (1.11).

The local concentration of sulphate therefore also increases to neutralize the charge. When the potential increases to -0.2 V, the rate of iron dissolution increases, which leads to an increase in interaction with sulfate in the medium. This can be seen by the increase in height of the sulfate peak at this potential.

### 5.3 Conclusion

The IR results show that when -0.4 V is applied to an iron electrode in different concentrations of lithium sulfate, the height of the sulfate peak in the asymmetric stretching region increases with increasing concentration from 0.1 to 1.8 M. This is due to the increase in $Fe^{+2}$ ions resulting from the dissolution of the electrode and thus the increase in $SO_4^{-2}$ ions needed to neutralize the charge. However, at 2.0 M and above, the height of the sulfate peak in the asymmetric stretching

region decreases due to the deposition of iron sulfate on the electrode, thus reducing the solubility of the iron electrode, and then the amount of sulfate ions needed for neutralization decreases.

Some changes were observed at high concentrations of lithium sulfate in the infrared range. First, there is a broadening and splitting of the band, and displacement of the sulfate peak, as well as the appearance of a peak at 980 $cm^{-1}$. This was due to the interaction of the sulfate ion with the surrounding ions, causing the sulfate to lose its symmetry. This is an indication that there are likely ions pairs and other aggregate solution species present at these electrolyte concentrations.

The IR absorption results are consistent with the results of CV and Raman spectroscopy in chapter 4. At lower concentrations, CV results show an increase in the dissolution rate of iron and an increase in the current resulting from this reaction. The Raman spectra of the electrode support this result as very few peaks appear in solutions of low concentration. Through the infrared results, we notice that the sulfate peak is more symmetrical, and the sulfate does not lose its symmetry because the concentration of ions is low and so each ion is separately solvated and does not interact with other ions very strongly.

At high concentrations, the reaction stops and the dissolution rate of iron decreases, according to the CV results. The formation of iron sulphate precipitation on the electrode from 1.8 M and above was confirmed by the results of Raman spectroscopy. The IR results also showed changes in the asymmetric sulfate stretching band due to the loss of sulfate symmetry and the appearance of a new peak in the symmetric stretching region. This shows the existence of interactions between ions in the solution and formation of ion pairs.

All results confirm that the reaction rate increases with increasing electrolyte concentration up to 1.8 M. The electrolyte concentration affects the kinetics of iron plating and stripping, as the reaction becomes slower at high electrolyte concentrations (above 1.8 M) due to the precipitation of $FeSO_4$ due to high ion concentrations.

# CHAPTER 6

## Some preliminary studies using concentrated electrolytes containing additive salts or water in salt electrolytes

This chapter is divided into two parts. The first part shows the effect of adding $MgCl_2$ to the electrolyte on the kinetics of oxidation of an iron electrode immersed in different concentrations of lithium sulfate. The second part studies the effect of using different concentrations of Lithium bis(trifluoromethane) sulfonimide (LiTFSI, a Water in Salt Electrolyte) on the anodic oxidation of iron. Both studies are preliminary and will require additional experimental work to fully understand the effect of the electrolyte in each case. However, the results, with some brief discussion and suggested areas of future research are presented here.

## PART 1

### 6.1. The effect of adding $MgCl_2$ on the behavior of an iron electrode in $Li_2SO_4$ electrolyte

The purpose of adding magnesium chloride to lithium sulfate at its various concentrations is because a previous study[74] has proven that adding magnesium chloride to the $FeCl_2$ electrolyte greatly enhances the performance of Fe batteries and significantly improves the CE of Fe deposition / stripping to 99.1%. The increase in CE is mainly due to the competing water reduction reaction becoming less favourable on addition of high concentrations of $MgCl_2$.

The structure of the electrolyte underwent several major changes after the addition of 4.5 M $MgCl_2$, as $Mg^{2+}$ was strongly bound to water molecules, resulting in a decrease in the number of hydrogen bonds per water molecule. There was also a change in the solvation shell surrounding the dissolved iron species, as the number of water molecules in the first solvation shell of $Fe^{2+}$ decreased, being replaced by chloride, and the average length of the hydrogen bonds increased. The competing reduction of water reaction became more difficult because the water O−H covalent bond became shorter and more rigid.

These changes in electrolyte structure were proposed using the results of Raman spectroscopy and FTIR. In the Raman spectra, upon addition of 4.5 M $MgCl_2$, the

two water bands (3600 and 3200 $cm^{-1}$) were removed, suggesting reduced H-bonds per water. For the FTIR results, there is a suppression of the 3200 $cm^{-1}$ band in the OH stretching region. The intensity of the O−H−O bending vibration peak at 1600 $cm^{-1}$ also increases with increasing $Mg^{2+}$ concentration, which also indicates the presence of a weak H-bond.

The high concentration of $Cl^-$ enhances the process of deposition and iron stripping, but the authors of this paper judged its effect is superficial. $Cl^-$ absorbs preferentially on the electrode but has little effect on the bulk structure of the water. These surface effects of $Cl^-$ were proposed as less important that the effect of $Mg^{2+}$ on the water.

The study also proved that the best results were when using a concentration of 4.5 M magnesium chloride for $FeCl_2$. Based on the results of this study, the same salt at the same concentration was used as an additive for the lithium sulphate electrolyte in the experiments reported in this chapter.

First, the results of CV measurements for different concentrations of lithium sulfate after the addition of 4.5 M $MgCl_2$ are presented. As in Chapter 4, CV was used to electrochemically dissolve metallic iron to form solution iron(II) species so that we could study the effect of salt addition on the dissolution rate of the iron electrode. Secondly, the results of IR spectroscopy of the electrode /electrolyte interface of an iron electrode with applied voltage, with different concentrations of $Li_2SO_4$ after adding 4.5 M $MgCl_2$ will be presented. The IR results provide information about the changes induced by $MgCl_2$ in the electrolyte structure at the potentials at which iron dissolution occurs. The IR results are then compared with the results of CV, as well as the IR results for a lithium sulfate solution without the addition of magnesium chloride, which were presented in Chapter 5.

### 6.1.1 Experimental methods

The same experimental steps were carried out as described in Chapter 4 for CV, Raman and IR spectroscopy, with the addition of 4.5 M $MgCl_2$ to each of the six concentrations of $Li_2SO_4$.

### 6.1.2 Result and Discussion:

#### 6.1.2.1 Cyclic voltammetry of Fe electrode in $Li_2SO_4$ electrolyte after adding 4.5 M $MgCl_2$

Experiments were performed using an iron electrode adding 4.5 M $MgCl_2$ to different concentrations of electrolyte (over the range of 0.1 M to 2.5 M $Li_2SO_4$). The same potential window (-1.3 V to 0.1 V and then returned to -1.3 V) was used as in Chapter 4.

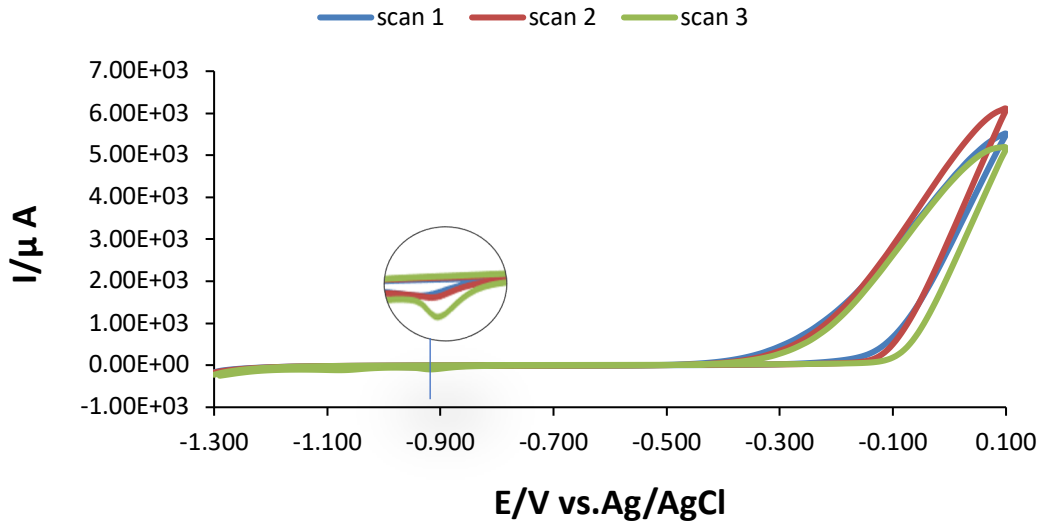


**Figure 6.1** Cyclic voltammetry at 0.05 $Vs^{-1}$ of iron electrode in 0.1 M $Li_2SO_4$ with 4.5 M $MgCl_2$.

In figure 6.1, CV of an iron electrode in 0.1 M $Li_2SO_4$ with 4.5 M $MgCl_2$ is shown. As can be seen in the first scan (in blue), the oxidation current initially appears at -0.3 V and flows continuously until it reaches its maximum value at 0.1 V. As before, the oxidation process can be expressed by equation (1.11).

On reversing the scan, oxidation current continues to flow in the range of 0.1 V to -0.32 V, and then reduction current begins to appear forming a small peak (see figure inset) at -0.92 V attributed to the reaction in equation (1.9).

In the second scan (in red), oxidation takes place at -0.32 V as the first scan, and the current slightly increased. In addition, the reduction peak is similar the previous scan. The third scan (in green) shows a similar response to the first scan; however ,the oxidation current is now slightly lower than the second scan, but there is an increase in the reduction peak current at -0.92 V.

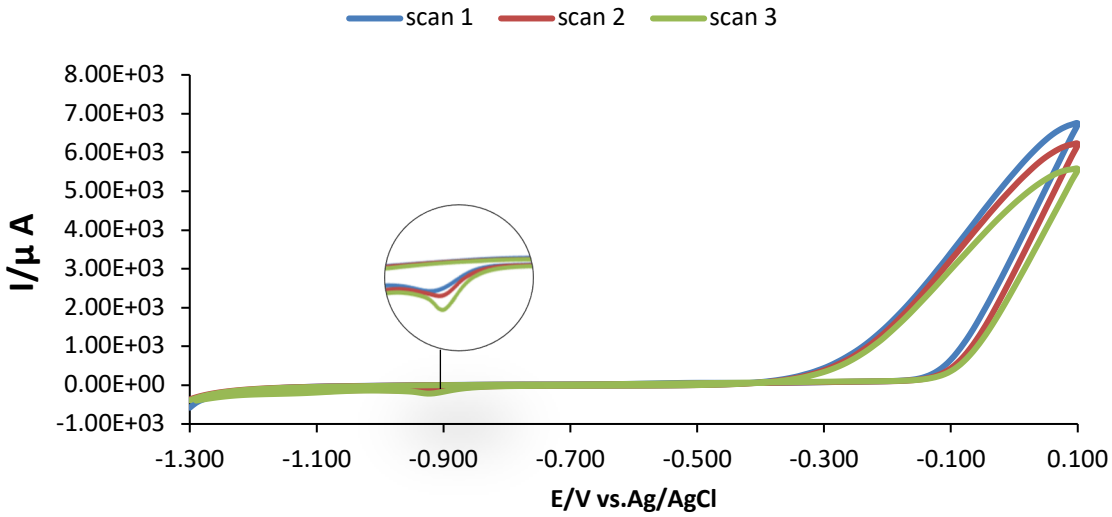


**Figure 6.2** Cyclic voltammetry at 0.05 $Vs^{-1}$ of iron electrode in 0.4 M $Li_2SO_4$ with 4.5 M $MgCl_2$.

In contrast, figure 6.2, illustrates CV results for an iron electrode in 0.4 M $Li_2SO_4$ with 4.5 M $MgCl_2$. In three scans, the oxidation starts to take place at -0.3 V, as was observed in 0.1 M $Li_2SO_4$. The oxidation current again increases rapidly until it reaches a value higher than that observed for the lower concentration in Figure 6.1 at 0.1 V and then decreases as the number of scans increases. It is noted that the oxidation current response is similar in shape to the current observed at a concentration of 0.1 M. The reduction peak at -0.92 V is formed for three scans when the scan is reversed. The height of the peak increases with the number of scans for the same concentration, and is greater than the peak recorded at a concentration of 0.1 M.

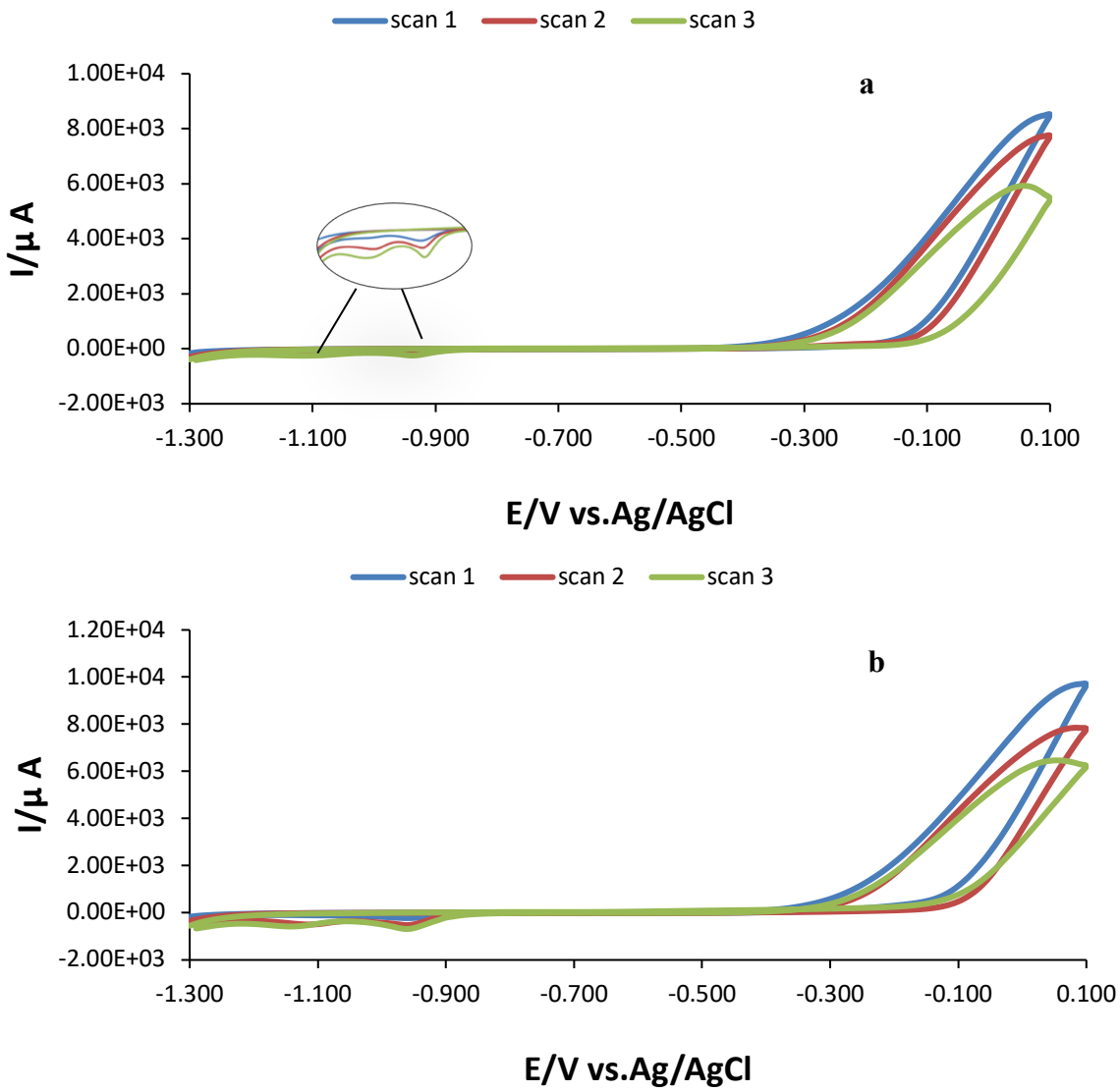


**Figure 6.3** Cyclic voltammetry at 0.05 $Vs^{-1}$ of iron electrode in a) 1.0 M and b) 1.8 M $Li_2SO_4$ with 4.5 M $MgCl_2$.

In Figure 6.3, the CV of the iron electrode in 4.5 M $MgCl_2$ with 1.0 M and 1.8 M $Li_2SO_4$, respectively, is shown over 3 consecutive scans each. The oxidation current again initially appears at -0.3 V and flows continuously until it reached a value higher than that observed for lower concentrations at 0.1 V. On reversing the scan, the oxidation current continues to flow in the range of 0.1 V to -0.3 V, then the reduction current starts to appear, and two peaks are observed at -0.92 and -1.1 V. The presence of two peaks may suggest there is more than one type of dissolved Fe(II) species in the solution under these conditions. As scanning continues, the oxidation current decreases and the reduction peak current increases. The oxidation current in 1.8 M $Li_2SO_4$ is higher than in 1 M.

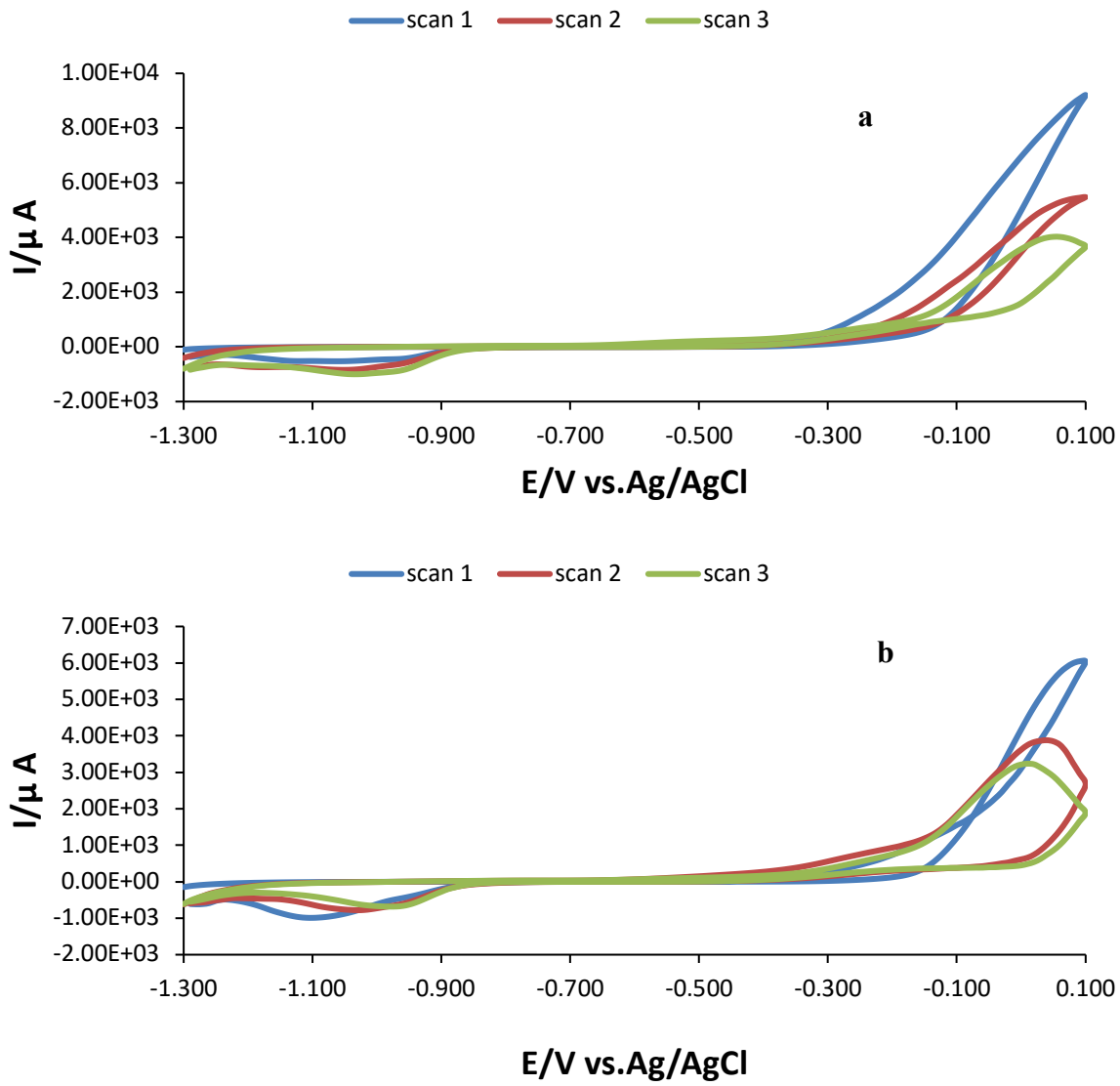


**Figure 6.4** Cyclic voltammetry at 0.05 $Vs^{-1}$ of iron electrode in a) 2.0 M and b) 2.5 M $Li_2SO_4$ with 4.5 M $MgCl_2$.

Figure (6.4,a) shows CV results for 2.0 M $Li_2SO_4$ with 4.5 M $MgCl_2$. In the first scan (in blue), the oxidation current starts at -0.3 V and increases until it reaches a value lower than observed for 1.8 M at 0.1 V. A single broad reduction peak at -1.0 V is formed when the scan is reversed. In the second scan (in red), the oxidation current decreases significantly compared to the first scan for the same concentration and is also lower than that observed for the second scan at the 1.8 M concentration. Moreover, the reduction peak is formed at the same potential as the first scan peak (-1.0 V). The third scan (in green) shows a different appearance from the first and second scans, as the current increases only slightly at -0.3 V, then there is a continuous increase at -0.1 V until it reaches a peak at 0.06 V. In addition, the reduction peak appears at −1.0 V.

Figure (6.4,b) also shows different results of CV of an iron electrode in 2.5 M $Li_2SO_4$. In all scans, oxidation starts at -0.3 V. Oxidation currents reach values lower than those observed for 2.0 M at 0.1 V. In addition, it is observed that the oxidation current shows a more pronounced hysteresis and differs from the shape observed at 2.0 M concentration. A reduction peak is formed at -1.1 V when the scan is reversed. In the second and third scans, initially the oxidation current increases slightly at -0.3 V and then increases gradually until it reaches the highest value at 0.06 and 0.02 V, respectively, and is less than that observed at 2. M. The reduction peak is formed at -1.0 and -0.95 V for the second and third scans, respectively.

By comparing the results of cyclic voltammetry of $Li_2SO_4$ solutions at different concentrations with and without the addition of $MgCl_2$ (Table 6.1), we found that when the additional salt is added, the dissolution of iron becomes faster and the current for the oxidation reaction increases. The iron dissolution and current value decrease at 2.0 M and above, but it is higher than the values at 2.0 and 2.5 M $Li_2SO_4$ without adding $MgCl_2$.

**Table 6.1** The maximum current at third scan for different concentration of $Li_2SO_4$ with and without adding $MgCl_2$

| Conc./M | Maximum current/ μ A | |
|---|---|---|
| | Without $MgCl_2$ | With $MgCl_2$ |
| 0.1 | 163 | 5169 |
| 0.4 | 321 | 5259 |
| 1.0 | 475 | 5449 |
| 1.8 | 1272 | 6219 |
| 2.0 | 1136 | 3672 |
| 2.5 | 926 | 1890 |

The CV of $Li_2SO_4$ without adding $MgCl_2$ at 2.0 M and above (see Figure 4.3 in Chapter 4) indicated that the current became passivated, and a layer was formed on the electrode. When $MgCl_2$ is added at the same concentrations, the current does not rapidly decrease, and the oxidation reaction is not so dramatically

suppressed. These results indicate that when $MgCl_2$ is added to $Li_2SO_4$, it helps improve the kinetics of iron oxidation and helps increase the solubility of iron and prevent formation of the passivating iron sulphide film.

### 6.1.2.2 Raman spectroscopy of the Fe surface after anodic treatment

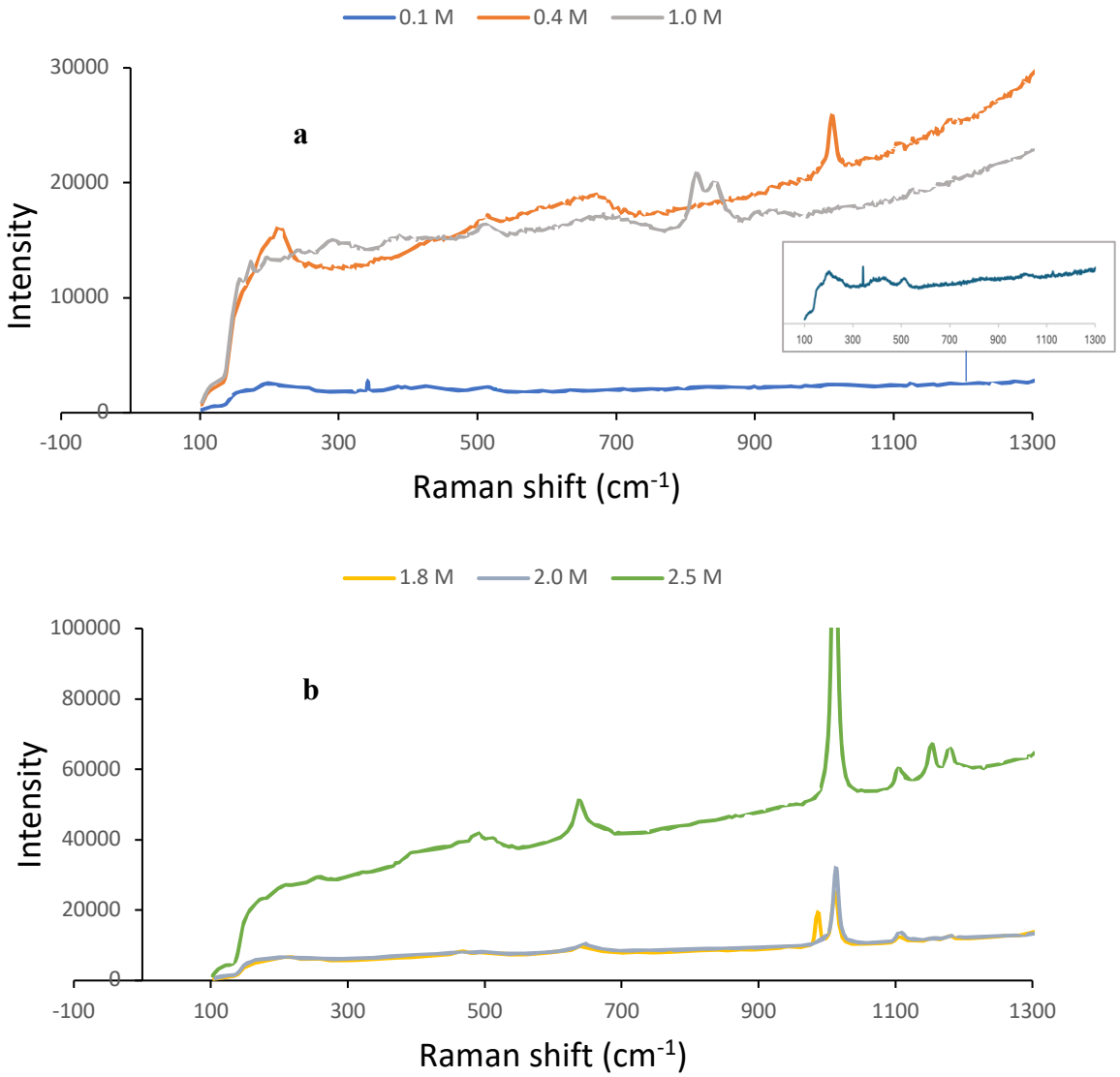


**Figure 6.5** Raman spectrum of iron electrode previously treated by chronoamperometry at 0.2 V in a) lower and b) higher concentrations of $Li_2SO_4$ after adding $MgCl_2$.

The Raman spectra shown in Figure 6.5 were recorded for iron electrodes that had previously been subjected to chronoamperometry at 0.2 V in different concentrations of $Li_2SO_4$ after adding $MgCl_2$. In Figure (6.5,a), the Raman spectra of iron electrodes oxidised in 0.1 M (dark blue), 0.4 M (orange) and 1.0 M (gray)

$Li_2SO_4$ with 4.5 M $MgCl_2$ show relatively few features, but there are two small peaks at 208 and 215 $cm^{-1}$ for 0.1 and 0.4 M, respectively. The 1.0 M treated iron has 2 peaks and one of them looks to be at 820$cm^{-1}$, the second one at 846 $cm^{-1}$. A clear peak also appears at 1014 $cm^{-1}$ for iron treated in 0.4 M $Li_2SO_4$. The sharp peak at 341 $cm^{-1}$ is the result of background interference from room lighting.

In Figure (6.5,b), the Raman spectrum in 1.8 M (yellow) shows a small peak at 649 $cm^{-1}$, followed by two peaks at 984 and 1109 $cm^{-1}$. At high concentrations of 2.0 M (light blue) and 2.5 M (green) $Li_2SO_4$, the spectra show a small peak at low wavenumbers of 472 and 492 $cm^{-1}$, respectively, followed by a small peak at 648 $cm^{-1}$ and a sharp peak at 1014 $cm^{-1}$ for two concentrations. A single peak appears at 1109 $cm^{-1}$ for 2 M and successive small peaks from 1111 to 1185 $cm^{-1}$ for 2.5 M.

The information from the Raman spectra is summarised in Table 6.2 below:

**Table 6.2** Raman bands observed from iron electrode surface after oxidation at 0.2 V in different concentrations for $Li_2SO_4$ after adding 4.5 M of $MgCl_2$.

| species | Raman spectrum | | | | | | | |
|---|---|---|---|---|---|---|---|---|
| | Absorption wavenumber $cm^{-1}$ | | | | | | | |
| | This work | | | | | | Literature Data | References |
| | 0.1 M | 0.4 M | 1.0 M | 1.8 M | 2.0 M | 2.5 M | | |
| $\nu_1(SO_4)$ | 10114 | 1014 | 820<br>846 | 1006 | 1014 | 1014 | 995-1013<br>976-1018 | [71]<br>[72] |
| $\nu_3(SO_4)$ | - | - | - | 1109 | 1109 | 1111<br>1152<br>1185 | 1024-1250<br>1071-1194 | [71]<br>[72] |
| $\nu_2(SO_4)$ | 516 | 516 | 516 | - | 472 | 492 | 438-536<br>423-492 | [71]<br>[72] |
| $\nu_4(SO_4)$ | - | - | - | 649 | 648 | 648 | 600-624<br>565-661 | [71]<br>[72] |
| F-S | 208 | 215 | - | - | - | - | 283 | [73] |

The results are consistent with the CV results showing an increase in the iron dissolution rate and an increase in the current resulting from this reaction from 0.1 to 1.8 M. There is no indication that the reaction is slowed down by the formation of a layer on the electrode, and indeed the Raman spectra of the electrode in low concentration solutions show only very weak peaks associated with surface species. At 2.0 and 2.5 M, we noticed that the current decreases

slightly, but the reaction does not stop. When comparing with the Raman spectra for the same concentrations and without adding $MgCl_2$, we see that some peaks that were present in Chapter 4 (without $MgCl_2$) do not appear now. This indicates that a significant layer is not formed on the electrode from a concentration of 1.8 M onwards.

As we indicated in Chapter 4, and after comparison with the literature (summarised in Table 6.2), the peaks appearing in Raman indicate the four vibrational modes of sulfate that are active in Raman. These modes are $\nu_1$ (983 $cm^{-1}$, symmetric stretching), $\nu_2$ (450 $cm^{-1}$, symmetric bending), $\nu_3$ (1105 $cm^{-1}$, asymmetric stretching) and $\nu_4$ (611 $cm^{-1}$, asymmetric bending)[71]. The peaks at 830 –1014 $cm^{-1}$ at all concentrations indicate the symmetric ($\nu_1$) vibrational mode of $SO_4^{2-}$, which gives sharp Raman lines. A peak of the asymmetric vibration mode region ($\nu_3$) of $SO_4^{-2}$ was observed at 1109 $cm^{-1}$ for concentrations 1.8 and 2 M, and peaks at 1111-1185 $cm^{-1}$, which were divided into three Raman lines at 2.5 M concentration. The splitting of the lines results from decreased symmetry of the sulphate and indicates a range of bonding environments. Symmetric bending modes $\nu_2$ $SO_4^{2-}$ appear for all concentrations at about 472 - 516 $cm^{-1}$ except 1.8 M. As for the asymmetric bending of $\nu_4$ for $SO_4^{2-}$, it appears only for concentrations from 1.8 to 2.5 M at 648 - 649 $cm^{-1}$.

Taken together, the Raman peaks show that the deposition of iron sulphate on the electrode surface increases when the concentration of $Fe^{2+}$ and $SO_4^{2-}$ is highest near the electrode surface. However, compared to the conditions in Chapter 4, the solution does not so readily reach the upper limit of iron sulfate saturation. Therefore, a thick passivation layer does not form on the surface as happened for solutions without the addition of $MgCl_2$. As discussed further below, this may be mitigated by competition between sulfate ions and chloride ions near the electrode surface.

#### 6.1.2.3 IR difference spectra at -0.3 V:

The IR difference spectra in figures 6.6-6.8 show the changes in absorbance when potential -0.3 V was applied to the Fe electrode in different concentrations of $Li_2SO_4$ after adding 4.5 M $MgCl_2$. As the oxidation process starts at this potential in CV, -0.3 V was selected. The results in Chapter 5 used a potential of

-0.4 V, as that is the potential at which oxidation started in those electrolyte conditions. The results presented here should therefore be relatively comparable to those in Chapter 5.

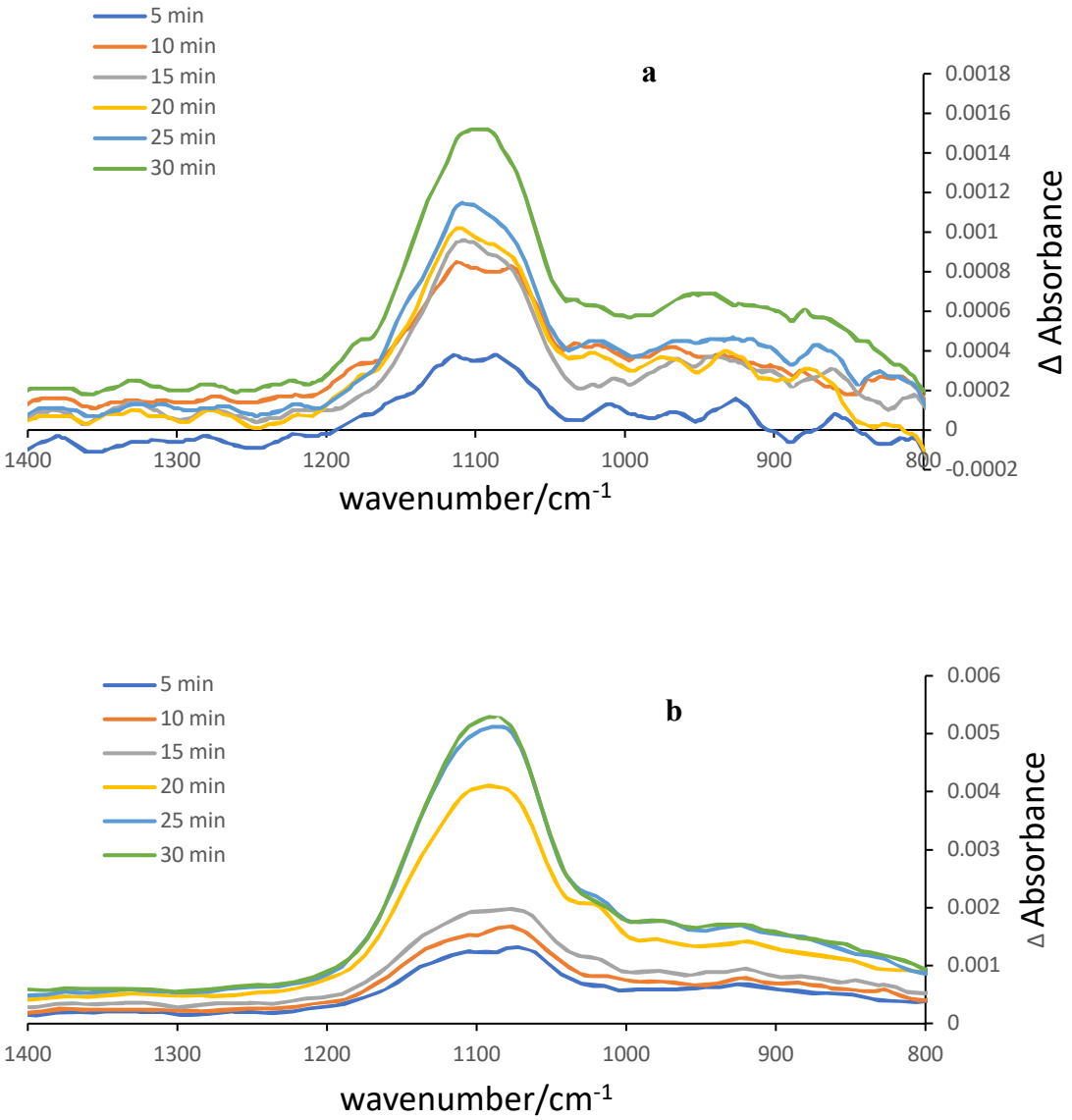


**Figure 6.6** Infrared difference spectra of iron electrode in a) 0.1 and b) 0.4 M $Li_2SO_4$ with 4.5 M $MgCl_2$ at -0.3 V.

The IR difference spectra in Figure 6.6(a,b) show the changes in the absorption peaks when -0.3 V was applied to the iron electrode at 0.1 and 0.4 M $Li_2SO_4$, respectively, after adding 4.5 M $MgCl_2$ to both, over a period of 30 min, in the wavelength range 800 $cm^{-1}$ to 1400 $cm^{-1}$. A small, almost symmetrical peak appears at 1093-1090 $cm^{-1}$ for both concentrations resulting from the asymmetric IR stretching mode of $SO_4^{2-}$. The intensity of absorption increases with increasing

time after application of the potential. The absorption intensity at 0.4 M is greater than that at 0.1 M over the same time periods.

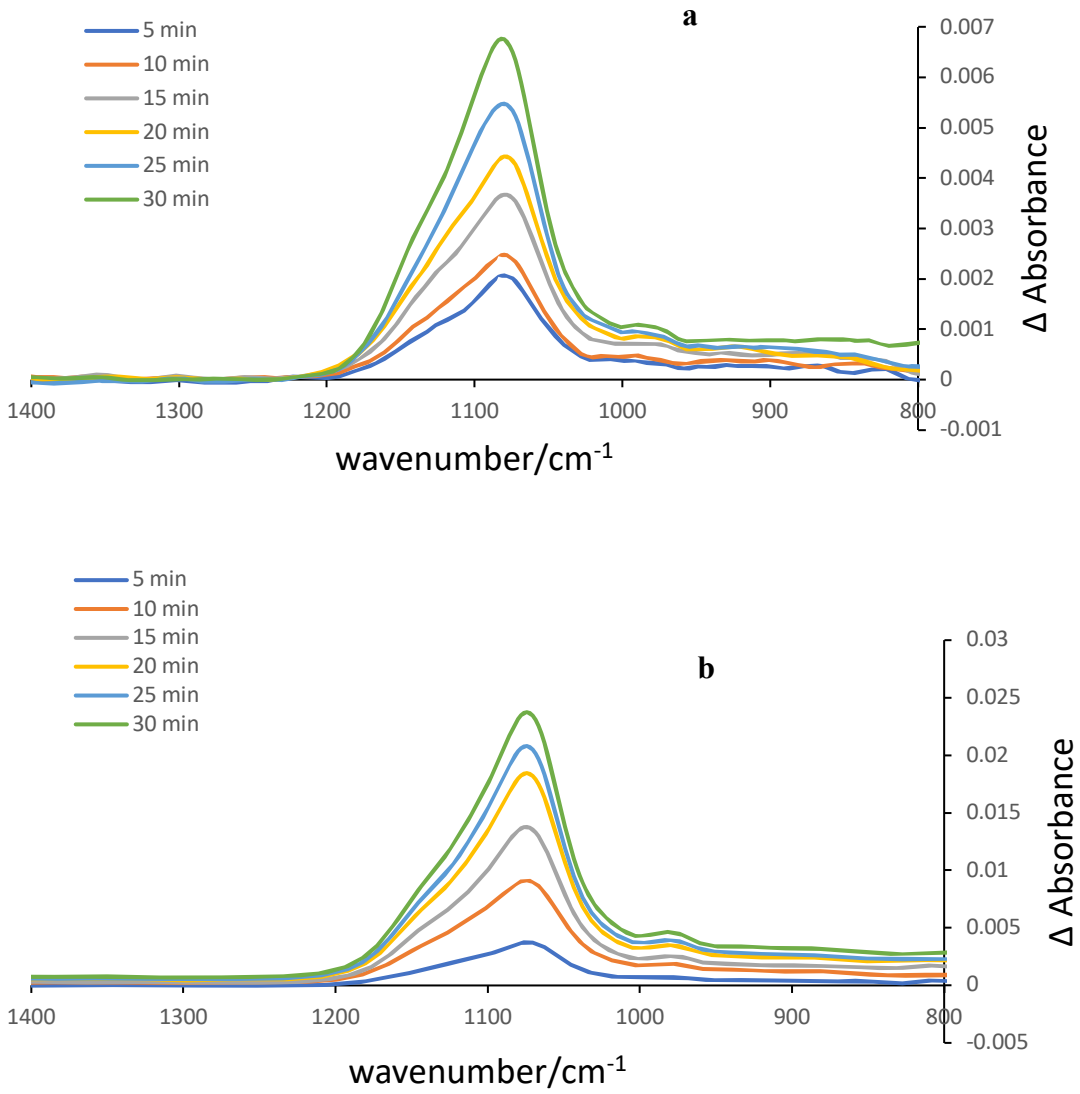


**Figure 6.7** Infrared difference spectra of iron electrode in a) 1.0 and b) 1.8 M $Li_2SO_4$ with 4.5 M $MgCl_2$ at -0.3 V.

Figure 6.7(a,b) shows a sharp peak at 1076 and 1070 $cm^{-1}$ for 1.0 and 1.8 M $Li_2SO_4$ after adding $MgCl_2$ to both. The height of this peak increases with increasing time. The intensity of the peak at 1.8 M is larger than that at 1.0 M and larger than the concentrations in figure 6.6. In addition, the peak at 980 $cm^{-1}$ is more pronounced at these two concentrations and its intensity increases with time. The maximum stretching frequency of $SO_4^{-2}$ changes from 1093 - 1090 $cm^{-1}$ at low concentrations to 1076 -1070 $cm^{-1}$ at 1.0 and 1.8 M. The peak also becomes less symmetrical, with significant amplitude with a higher wavenumber than the peak.

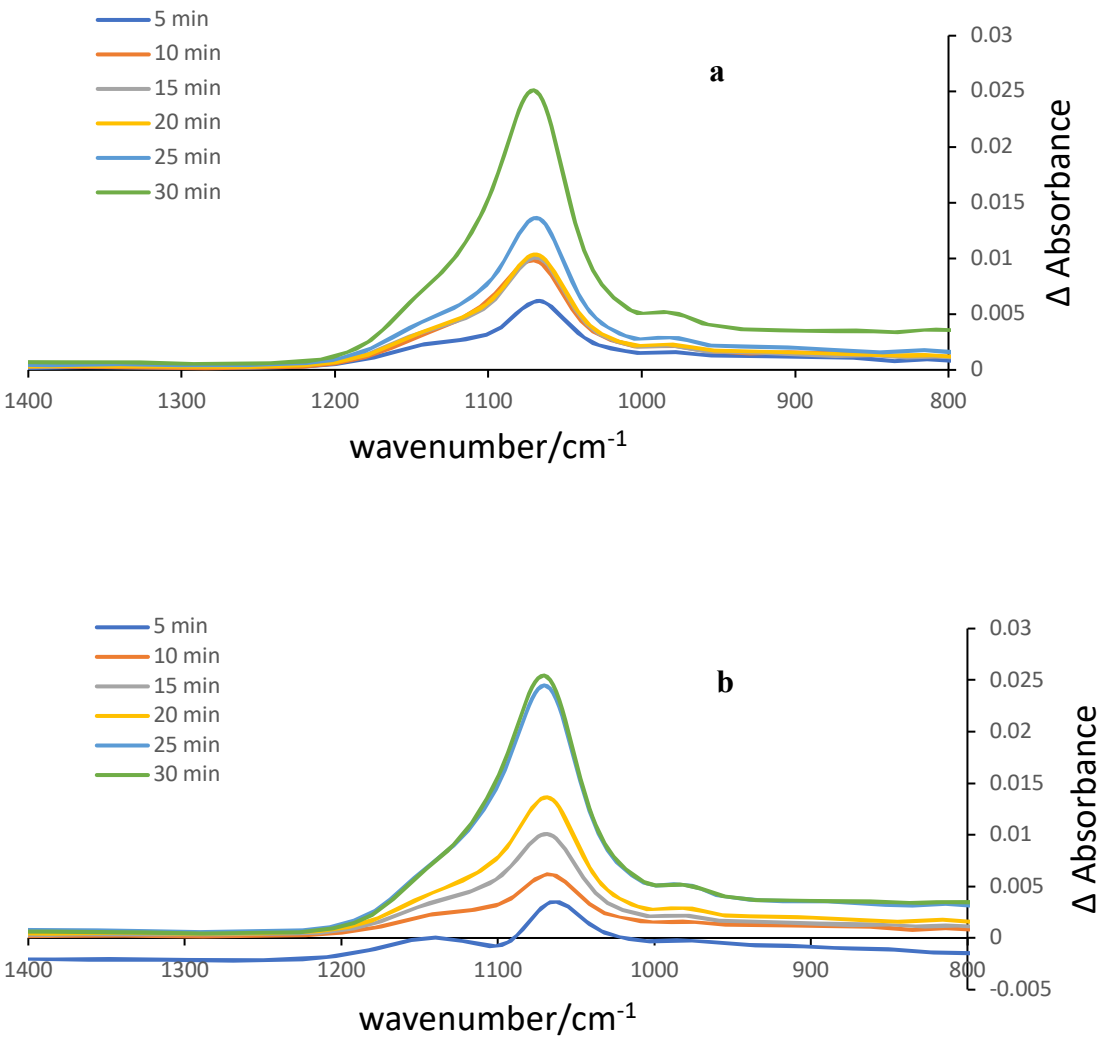


**Figure 6.8** Infrared difference spectra of iron electrode in a) 2 and b) 2.5 M $Li_2SO_4$ with 4.5 M $MgCl_2$ at -0.3 V.

Figure 6.8(a,b) shows a sharp asymmetric peak at 1064 $cm^{-1}$ for the 2.0 and 2.5 M solutions, which increases in intensity with increasing time. There is a very clear shoulder on the upper wavenumber side of the peak for both concentrations. The peak intensity for 2.0 and 2.5 M is close to the peak intensity for 1.8 M. In addition, there is a small, broad peak with a position of 980 $cm^{-1}$.

The results showed that when -0.3 V was applied to an Fe electrode in different concentrations of lithium sulfate after adding a high concentration of $MgCl_2$ salt, the concentration of sulfate ions in the region probed by IR increased with increasing electrolyte concentration. The reason, as mentioned in Chapter 5, is likely to be that the rate of iron dissolution increases with increasing electrolyte

concentration, which causes more $Fe^{+2}$ ions in the solution near the electrode, attracting more $SO_4^{2-}$ ions to neutralize the charge locally.

A higher peak intensity is observed at high concentrations from 1.8 to 2.5 M, in contrast to what it was without the addition of salt (see Chapter 5). This may be partly due to the presence of high concentrations of $Mg^{2+}$ and $Cl^-$ ions that increase solution conductivity and hence increase the rate of the dissolution process. With reference to the study discussed previously[74] our results are consistent with a change in the hydration shell of $Fe^{2+}$ when $MgCl_2$ was included in the solution, as the number of water molecules decreased, and in return, chloride ions increased in the solvation sphere of iron (ion pairing). Thus, there are fewer sulfate ions needed to neutralize the iron ions that are produced, as $Cl^-$ can pair with $Fe^{2+}$. This results in the iron sulfate not reaching the saturation point, so a passivation layer does not form on the surface of the electrode. Therefore, the intensity of absorption of free sulfate ions increases at concentrations of 2 M and above as the dissolution process continues and is not passivated.

We also notice that at low concentrations (0.4 M $Li_2SO_4$), sulfate loses its symmetry in the asymmetric stretching range at 1050 -1250 $cm^{-1}$ due to the addition of magnesium chloride. Results in Chapter 5 showed that the sulphate peak remained more symmetrical at this concentration in the absence of $MgCl_2$. We propose that increasing the number of ions in the solution led to an increase in the interaction and collision of sulfate with the surrounding ions ($Mg^{2+}$, $Cl^-$, $Li^+$ and $Fe^{2+}$), which leads to a broadening and splitting of the peak as the sulfate bonds are not all equivalent. There is also a shift in the stretching frequency of $SO_4^{2-}$ from 1093 $cm^{-1}$ at 0.1 M to 1064 $cm^{-1}$ at 2.5 M, which indicates an enhanced ionic atmosphere (Stark shift) and the peak at 980 $cm^{-1}$ appears due to the loss of sulfate symmetry.

### 6.1.3 Discussion, conclusion and future work

Based on the positive effects reported in a previous study[74] magnesium chloride was added to different concentrations of lithium sulphate with the aim of improving the efficiency of the iron electrode in dissolving. The results of cyclic voltammetry of different concentrations of $Li_2SO_4$ solutions after adding $MgCl_2$ showed that the dissolution of iron became faster and the oxidation current

increased from 0.1 to 1.8 M. The solubility of iron decreases at 2 M and above compared to the concentration of 0.1 to 1.8 M but is higher than the values at 2 and 2.5 M without the addition of $MgCl_2$. That is, the solubility of iron at 2 and 2.5 M improved, and the deposition of a layer of iron sulphate on the electrode was prevented after adding $MgCl_2$. This result is consistent with the result of the paper, which stated that the performance of the iron electrode improves in dissolution and precipitation with the addition of salt. The IR results agree with the results of CV and Raman spectroscopy experiments. Through the IR results, we notice that the sulfate peak loses its symmetry at lower concentrations than without the $MgCl_2$ additive. This is because increasing the number of ions in the solution led to an increase in the interaction of sulfate with the surrounding ions, which leads to the broadening and splitting of the peak.

At high concentrations (2 M and 2.5 M), the reaction continues and does not stop, with the iron dissolution rate decreasing slightly, according to the CV results. From the Raman results, the spectra showed fewer vibrational peaks for sulfate compared to the absorption spectra for the same high concentrations without the addition of magnesium chloride. This indicates that the iron sulphate concentration near the electrode does not reach the saturation point. As discussed above this may be due to the different solvation sphere structures for Fe(II) in the solution, with more $Cl^-$ in the solvation sphere.

All results confirm that the iron dissolution reaction rate increases when magnesium chloride is added to different concentrations of the electrolyte. $Mg^{2+}$ improves the kinetics of iron plating and stripping, such that the reaction becomes faster at all electrolyte concentrations compared to the same concentrations of electrolyte but without the addition of $MgCl_2$. Further experiments are needed to show the actual role of each ion in the solution and the role of water, chloride and sulphate in the solvation sphere of Fe(II). Examination of the water stretching region in the IR spectra is likely to provide more information on this.

# PART 2

## 6.2. Fe dissolution in the water in salt electrolyte LiTFSI

This section presents the results of electrochemical measurements as well as in situ spectroelectrochemistry using different concentrations of LiTFSI as electrolyte. CV was used to oxidise metallic iron to form dissolved iron (II) so that we could study the effect of electrolyte concentration on the dissolution rate of the iron electrode and try to understand the kinetics of the oxidation reaction that occurs. The second type of electrochemical measurement is the chronoamperometry measurement, which was applied to the iron electrode after being immersed in different concentrations of LiTFSI. Raman spectroscopy of the iron electrode also carried out after oxidation to see what species appear on the surface of the electrode, and whether there are competing interactions with the aqueous electrolyte. The results of in situ IR will also be presented, to determine changes in solution species at the iron electrode at different concentrations of LiTFSI and at a certain potential.

A Water in Salt Electrolyte (WiSE) is defined as a solution where salt content by mass and volume is greater than water content[75]. These solutions can contain salt up to very high molality e.g. LiTFSI has a solubility of 21 molal (mols of salt per kg water) compared to 3-4 molal for $Li_2SO_4$. In these salts there is very little 'free' water that is unbound to ions; most is coordinated to $Li^+$. There is a large degree of ion pairing and aggregate formation in these electrolytes and nanodomains where the anions and cations form complex structures within the solution. These solutions are still relatively novel and under-explored.

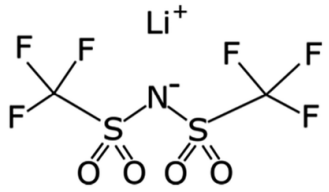


**Figure 6.9** chemical structure of LiTFSI, adapted from[76]

### 6.2.1 Experimental methods

CV was performed using a cell with three electrodes, an iron electrode (working electrode, WE), a platinum counter electrode (CE) and an Ag/AgCl reference electrode (RE) that were immersed in different electrolyte concentrations (0.1, 1.0, 5.0, 10 ,15 molal LiTFSI). The potential window was chosen from -1.3 V to 0.3 V and then back to -1.3 V.

In chronoamperometry, the current was measured for an iron electrode immersed in different concentrations of LiTFSI for 750 s. A potential of 0.2 V was applied because this is the potential at which the redox response peaks in CV measurements.

In Raman spectroscopy, chronoamperometry was initially applied to the iron electrode with different concentrations of LiTFSI at 0.2 V which is the potential at which the oxidation process reaches its peak in CV measurements. Then Raman spectra of this electrode were recorded for 20 scans using a laser wavelength of 514.5 nm.

For IR spectroscopy, LiTFSI electrolyte is placed in the cell and the spectrum is taken as background. Upon measuring all the spectra for different concentrations of LiTFSI, 0.2 V is applied and the change in the resulting spectra from the background spectrum are determined. Hence the IR spectra presented in this report are difference spectra.

### 6.2.2 Result and Discussion:

#### 6.2.2.1 Cyclic voltammetry of Fe electrode in LiTFSI electrolyte

In this study, experiments using an iron working electrode were performed with varying electrolyte concentrations (0.1, 1.0, 5, 10,15 m LiTFSI).

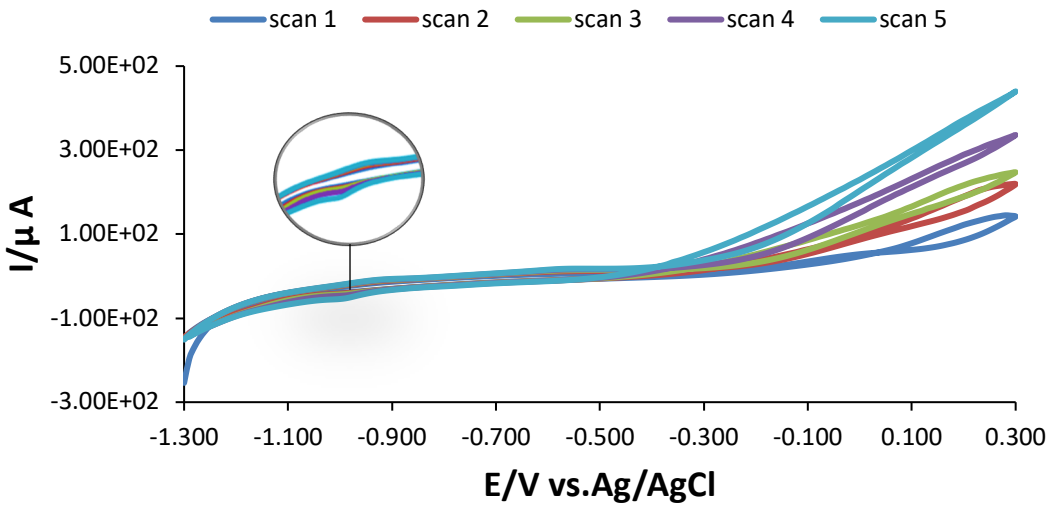


**Figure 6.10** Cyclic voltammetry at 0.05 $Vs^{-1}$ of iron electrode in 0.1 m LiTFSI.

In figure 6.10, CV of an iron electrode in 0.1 m LiTFSI is shown over 5 consecutive scans. The scan started from -1.3 V and was scanned towards 0.3 V. In the first scan (in blue), the oxidation current initially appears at -0.3 V and flows continuously until it reaches its maximum value at 0.3 V. On reversing the scan, oxidation current continues to flow in the range of 0.3 V to -0.3 V but does not follow the current of the forward scan, it shows hysteresis. Then reduction current begins to be observed forming a small peak at -0.98 V. As scanning continues, the current increases. In addition, small increase in the reduction peak current is observed at same potential.

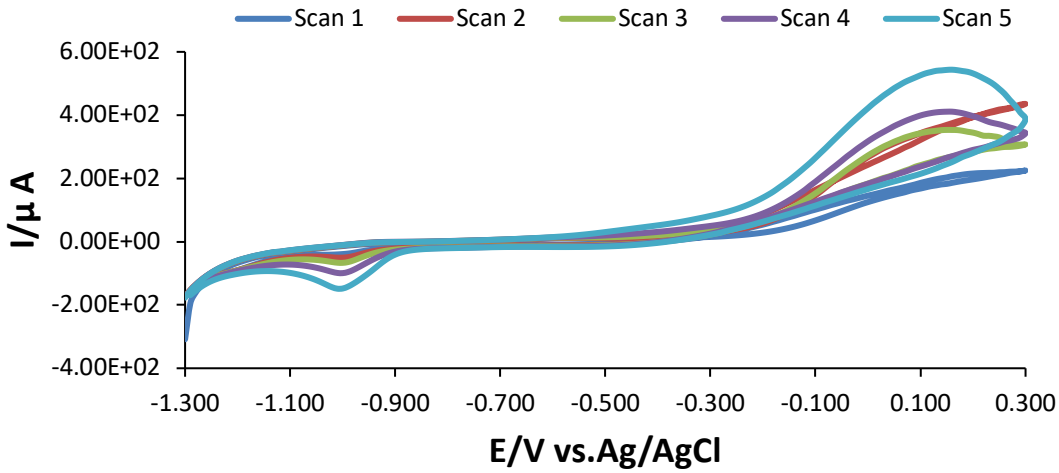


**Figure 6.11** Cyclic voltammetry at 0.05 $Vs^{-1}$ of iron electrode in 1.0 m LiTFSI.

In contrast, figure 6.11 shows different results of cyclic voltammetry of an iron electrode in a 1.0 m LiTFSI. In all scans, oxidation starts at -0.3 V as observed in

0.1 m LiTFSI. The current increases rapidly with scan number until it reaches a value higher than that observed for the lower concentration in figure 6.10 at 0.3 V. In addition, it is noted that the oxidation current differs from the shape observed at a concentration of 0.1 m as it is more peak-like. A reduction peak at -0.98 V is formed for all scans when the scan is reversed. The height of the reduction peak increases with the number of scans for the same concentration, and it has higher currents than the peak recorded at a concentration of 0.1 m.

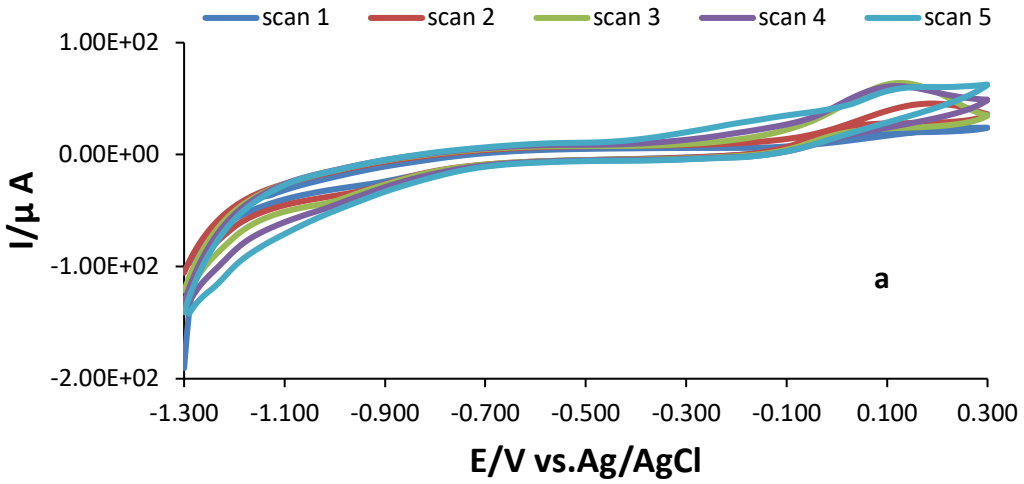


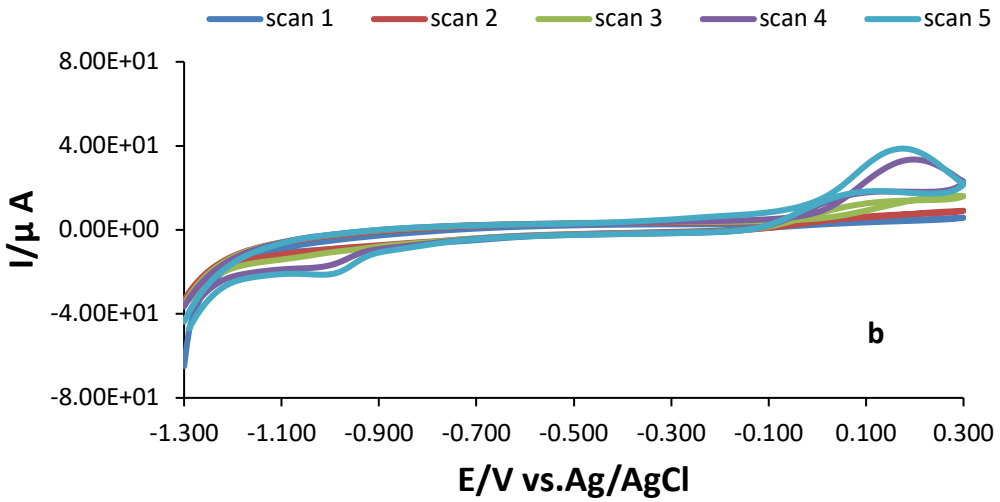

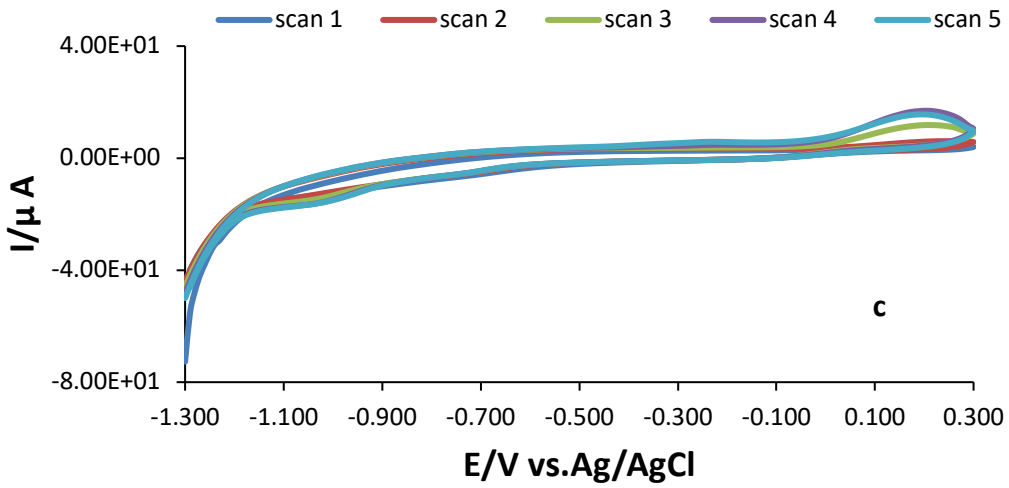


**Figure 6.12** Cyclic voltammetry at 0.05 $Vs^{-1}$ of iron electrode in a) 5.0, b) 10, c) 15 m LiTFSI.

In Figure 6.12(a,b,c), the CV results are shown for 5, 10 and 15 m of LiTFSI. For all scans oxidation starts at -0.1 V. This is a more positive potential than that observed in 0.1 and 1.0 m LiTFSI. This suggests that there is a kinetic barrier to the oxidation in these conditions so a greater overpotential is required for the oxidation to take place. The current increases rapidly with scanning for each concentration, but is less than that observed for the low concentrations in Figures 6.10 and 6.11 at 0.3 V. In addition, as the electrolyte concentration increases, the oxidation current decreases. A reduction peak at -0.98 V is formed for all concentrations when the scan is reversed. The height of the reduction peak increases with the number of scans for the same concentration.

These results indicate that at low concentrations (up to 0.4 m) of LiTFSI, the dissolution of iron becomes faster as salt concentration increases and the oxidation current increases. On the other hand, the iron dissolution rate and the current decreases at 5, 10 and15 m LiTFSI. The decrease in the rate at which iron oxidised could be linked to the increase in the viscosity of the solution and the decrease in its conductivity. In terms of conductivity, as described in Chapter 3 it generally rises as the concentration of electrolytes increases until a specific point is reached. This is because there is a greater abundance of charge carriers (ions) available. At larger concentrations, the conductivity may decrease as a result of ionic pairing, aggregation, and the creation of aggregates. These processes lower the amount of free ions that are available for charge transfer and

so current becomes limited. Higher concentrations of LiTFSI result in increased viscosity of the electrolyte solution, impeding the movement of ions. This could decrease the rate at which iron ions diffuse away from the electrode surface. The decrease in mass transfer can result in a lowering of the overall dissolution rate.

Comparison of the CVs in 0.1 m and 1.0 m LiTFSI with the CVs in Chapter 4 for similar concentrations of $Li_2SO_4$ shows that oxidation currents are about 10 times smaller in LiTFSI than in $Li_2SO_4$. The reason for this is that the TFSI anion is significantly larger in size compared to the sulphate anion ($SO_4^{2-}$). The increased size of the TFSI anion leads to decreased mobility when dissolved in a solution. Reduced ion mobility can lead to a decrease in ionic conductivity, resulting in a decrease in current. Furthermore, concentrated solutions of LiTFSI exhibit the formation of ionic pairs ($Li^+$ with $TFSI^-$) as well as more complex aggregates. These pairs and aggregates decrease the number of free ions available for charge transfer, reducing the overall current.

### 6.2.2.2 Chronoamperometry of Fe electrode in LiTFSI electrolytes

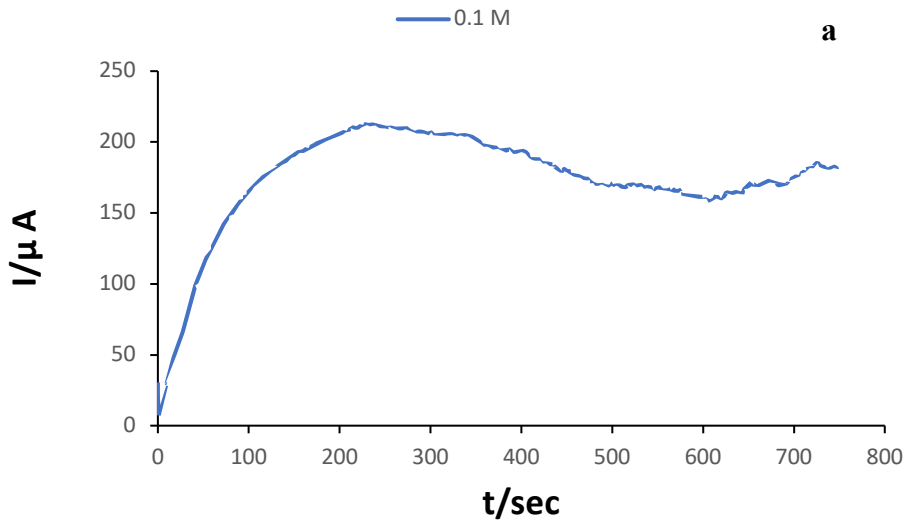

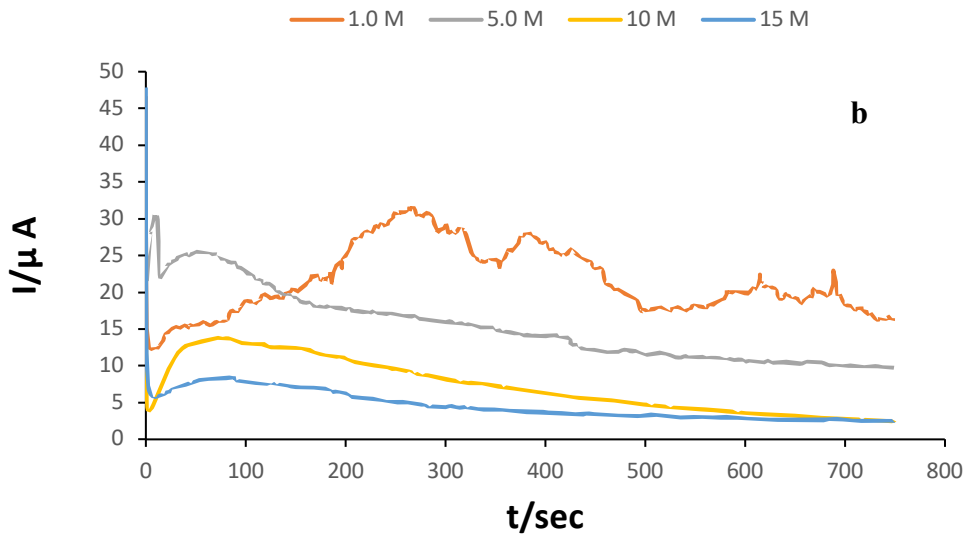


**Figure 6.13** Chronoamperometry performed at 0.2 V of iron electrode in a) 0.1 m and b) 1, 5 ,10 and 15 m of LiTFSI

For the measurements shown in Figure 6.13(a,b), the iron electrode was placed in with different concentrations of LiTFSI (0.1, 1.0, 5.0 ,10 ,15 m) and a potential of 0.2 V was applied because this is the potential at which the redox response is approximately highest in CV measurements, and the current was measured for 750 sec.

At 0.1 m (figure 6.13,a), the current increased continuously until it reached the maximum current at 240 seconds, then it began to decrease gradually until 600 seconds, then it increased slightly during a period from 600 to 750 seconds. When moving to figure (6.13,b), we notice that the current at 1.0 m increases until it reaches its maximum at 270 seconds, then the current value fluctuates until it reaches its lowest value at 750 seconds. While in 5.0 m, the current recorded a noticeable increase at the beginning of the time period, reaching its maximum value at 10 seconds. Then the current suddenly decreased and reached its lowest point at about 14 seconds, and then began to rise again after about 60 seconds, and so during the rest of the time period, the value of the current gradually decreased. On the other hand, when moving to high concentrations 10 and 15 m, the current records values below the 5.0 m concentration at 750 sec.

These results indicate that at low concentrations of LiTFSI, the current increases for a certain period of time and then the dissolution rate decreases at the end of the time. While at high concentrations, the current decreases early and continues

to decrease until the end of the period of time. The reason for this is that as the concentration increases, the mobility of ions decreases. This results in a decrease in conductivity and hence a decrease in current. This is consistent with the slow reaction rates observed and discussed for CV above.

#### 6.2.2.3 Raman spectroscopy of the Fe surface after anodic dissolution

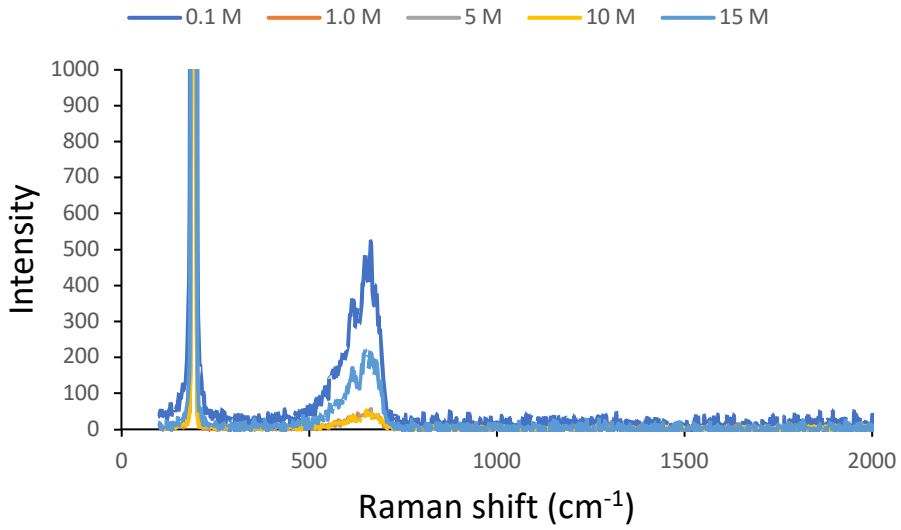


**Figure 6.14** Raman spectrum of iron electrode previously treated by chronoamperometry in different concentrations of LiTFSI at 0.2 V.

The Raman spectra shown in Figure 6.14 were recorded for iron electrodes that had previously undergone chronoamperometry at 0.2 V in different concentrations of LiTFSI. This is in order to observe the changes that occur to the electrode. Raman spectra of iron electrodes at all LiTFSI concentrations show only two peaks at 200 and 665 $cm^{-1}$ . The peak appearing at 200 $cm^{-1}$ belongs to the twisting vibration of the $CF_3$ group, while the peak observed at 665 $cm^{-1}$ belongs to bending vibration of the C–N–C group, based on the research of Liumin Suo et al[77].

**Table 6.3** Raman spectra of LiTFSI

| Assignment | Raman spectrum | | |
|---|---|---|---|
| | Absorption wavenumber $cm^{-1}$ | | |
| | This work | Literature Data | References |
| $CF_3$ twisting vibration | 200 | 138 | [77] |
| C–N–C bending vibration | 665 | 747 | [77] |

These results indicate that different concentrations of LiTFSI do not record differences in the Raman spectra.

Raman spectroscopy indicates the presence of TFSI anions on the electrode surface, suggesting their adsorption onto the surface. Adsorption decreases the quantity of active sites accessible for the electrochemical reactions and slows the reaction kinetics as a resistive layer is formed on the electrode surface. As a result, the electrochemical reaction in LiTFSI solutions is greatly reduced compared to sulphate solutions at lower concentrations, where there are no major adsorption effects. This accounts for the reduced currents and decreased reaction rates that are found in CV measurements for (LiTFSI) solutions more than $SO_4^{2-}$, as described above.

#### 6.2.2.4 IR difference spectra at 0.2 V:

The IR difference spectra in figures 53-54 show the changes in absorbance when potential 0.2 V was applied to Fe electrode in different concentrations of LiTFSI. The oxidation process is highest at a potential of 0.2 V in CV. It is expected that the iron is undergoing anodic dissolution at this potential and at a relatively high rate.

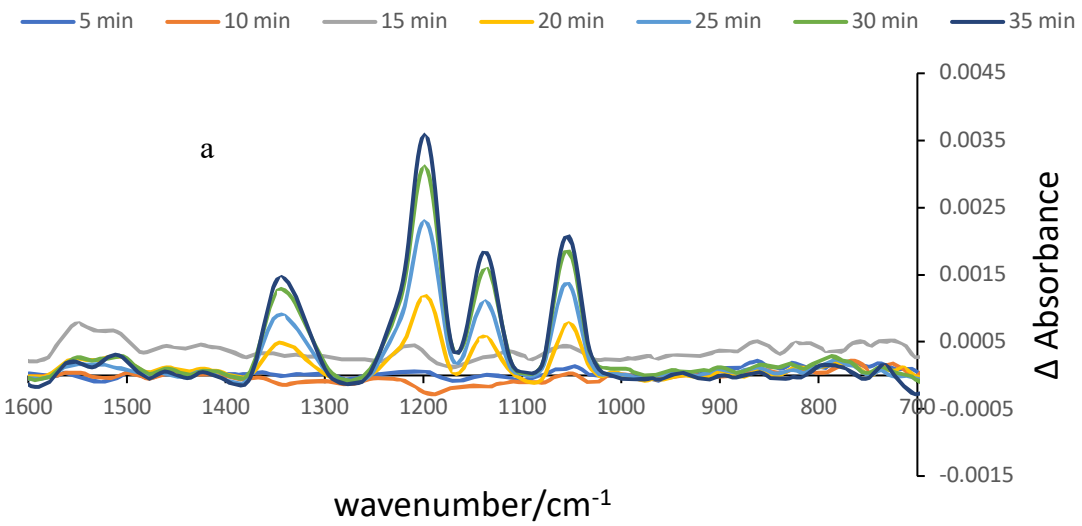

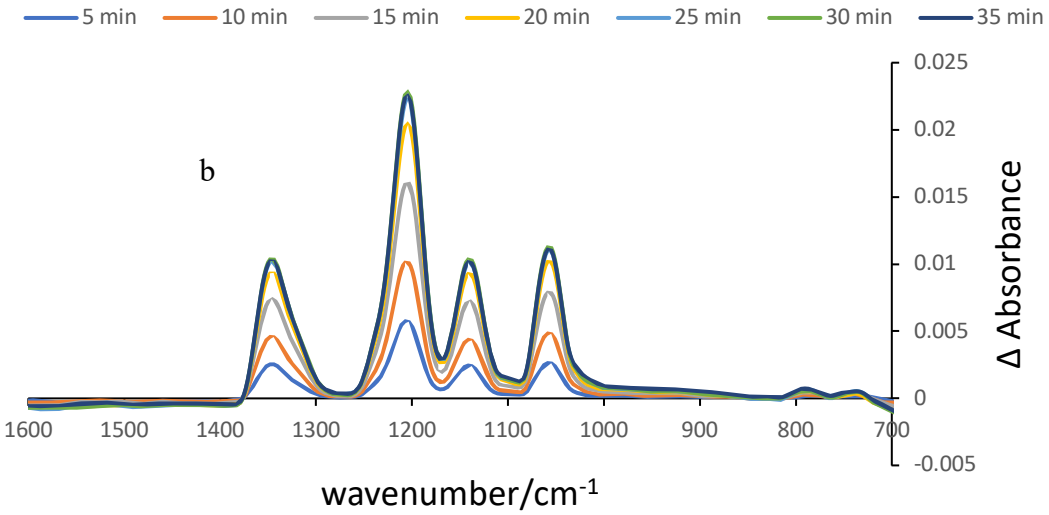


**Figure 6.15** Infrared spectrum of iron electrode in a) 0.1 m b) 1.0 m of LiTFSI at 0.2 V.

In figure 6.15(a, b), IR difference spectra show the changes in the absorbance peaks when potential 0.2 V was applied to the Fe electrode with a concentration of 0.1 and 1.0 m LiTFSI, respectively, over a period of 35 minutes in the wavenumber ranges from 700 $cm^{-1}$ to 1500 $cm^{-1}$. Four sharp positive peaks followed by two weak peaks appear for both concentrations, and their intensity increases with time after applying the potential. The absorption intensity at 1.0 m for all peaks is greater than that at 0.1 m during the same time periods. A peak at 1334 $cm^{-1}$ appears as a C–$SO_2$–N bonding mode for $TFSI^-$, and there is another C–$SO_2$–N bonding mode for LiTFSI at 1134 $cm^{-1}$. The sharp peak at 1195 $cm^{-1}$ was assigned to the asymmetric stretching mode for $CF_3$, followed by another peak at 1050 $cm^{-1}$ which was assigned to the asymmetric stretching mode for S–N–S. The two weak peaks at 780 and 730 $cm^{-1}$ are attributed as the $CF_3$ symmetric bending mode and the S–N stretching mode, respectively.

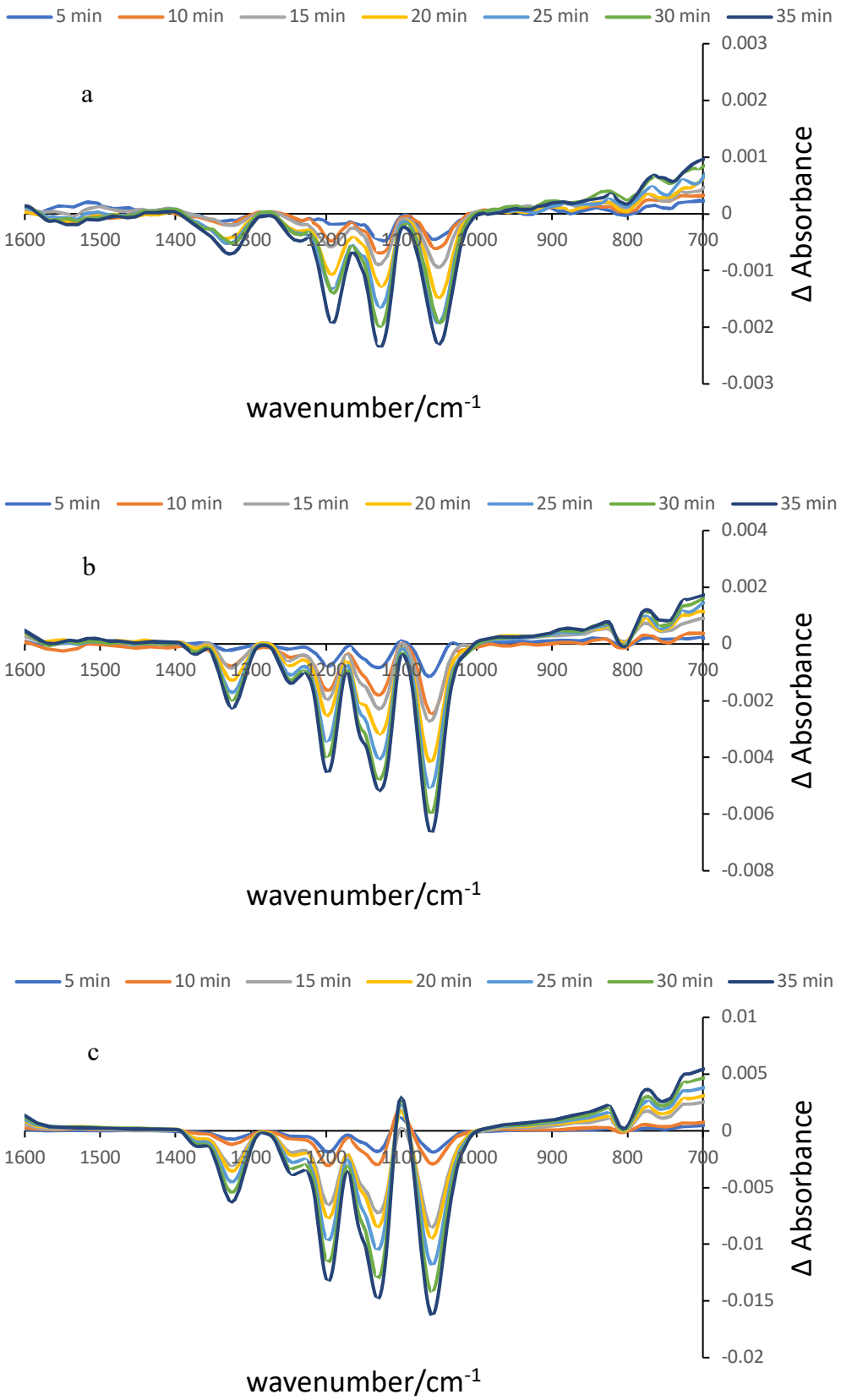


**Figure 6.16** Infrared spectrum of iron electrode in a) 5.0 m b) 10 m c) 15 m of LiTFSI at 0.2 V.

Figure 6.16(a,b,c) the absorption difference spectra of the iron electrode are shown for 5, 10 and 15 m, respectively .It was observed that four negative sharp peaks at 1334 ,1195, 1134 and 1050 $cm^{-1}$ occur for these three concentrations, and their intensity increases negatively with increasing time. There is a very clear negative shoulder to the higher wavenumber side of the peak for 10 and15 m but not 5 m. In addition, there is a small broad peak at 1242 $cm^{-1}$ for three concentrations. In Table 6.4, the IR spectrum results from Figure (6.15-16) above and those of previous LiTFSI studies are summarized.

**Table 6.4** The assignments of characteristic peaks of LiTFSI.

| Description of bands | Wavenumbers/$cm^{-1}$ | | References |
|---|---|---|---|
| | This work | Literature Data | |
| S–N symmetric stretching | 730 | 737-748 | [78,79] |
| $CF_3$ symmetric bending | 780 | 787 | [78] |
| S–N–S asymmetric stretching | 1050 | 1062-1056 | [78,79] |
| C–$SO_2$–N bonding mode | 1134 | 1143-1135 | [78,79] |
| $CF_3$ asymmetric stretching | 1195 | 1193 | [78] |
| C–$SO_2$–N bonding mode | 1334 | 1333 | [78] |
| $SO_2$ asymmetric stretching | 1396 | 1357 | [78] |

Although the positions of some peaks are the same as those observed for 0.1 m and 1.0 m solutions, at the higher concentrations the change in absorption is negative rather than positive. More experimental work is required to understand this change in behaviour, which was not observed in the $Li_2SO_4$ electrolytes studied. At concentrations of 0.1 and 1 m LiTFSI, the molecules are well dispersed in water and there are no strong interactions between them. The characteristic vibration modes of LiTFSI absorb infrared radiation such as C-F, S-N, and S=O stretching vibrations, and appear as positive bands in the ATR-IR spectrum. The bands are positive an increase over time, similar to the interpretation in Chapter 5, the concentration of $TFSI^-$ anion can increase near the electrode surface when $Fe^{2+}$ is dissolving, in order to neutralize the charge.

At concentrations of 5, 10 and 15 m LiTFSI, strong interactions occur between the solute and solvent, the network of hydrogen bonds in water is disrupted, and ionic pairs or groups are formed, which have different absorption properties for

IR compared to free ions. The mobility of the ions is also decreased due to the high viscosity caused by strong ion pairing and aggregation. The anion may for these reasons not be able to freely move to the region being probed by IR or may for some reason associated with intermolecular interactions be repelled from this region causing an apparent decrease in concentration.

### 6.2.3 Discussion, Conclusion and future work:

Lithium sulfate ($Li_2SO_4$) and lithium TFSI are both lithium salts but differ significantly in their structures. Understanding these differences is crucial for their application in areas such as battery technology. $TFSI^-$ anions are very large and therefore their diffusion rate is very slow, and they have a more hydrophobic character due to the fluorinated groups. LiTFSI has a high solubility, higher than that of $Li_2SO_4$, as mentioned previously, as 21 moles of LiTFSI are equivalent to 3-4 moles of $Li_2SO_4$. In these salts there is very little "free" water not bound to ions; Most of them are coordinated to $Li^+$. Sulfate and lithium ions are strongly hydrating ions, so they work to trap the free movement of water molecules. This effect can extend beyond the first hydration layer to several layers of surrounding water. They also tend to form double-solvent-separated ion pairs (2SIPs) and solvent shared ion pairs (SIPs). As for LiTFSI, it tends to form complex structures within the solution such as contact ion pairs (CIPs) and aggregates (AGGs) between the cation and the anion[80]. These differences between LiTFSI and $Li_2SO_4$ affect the dissolution of Iron and the formation of the passivation layer.

In the CV and chronoamperometry of lithium sulfate, it has been observed that at high concentrations the current stopped due to the formation of a passivation layer as a result of the deposition of iron sulfate on the surface of the iron electrode, and that the reaction current decreased at the highest concentrations. Raman results confirmed a film formation by the presence of peaks in the sulfate vibration positions. As for LiTFSI, from the CV results we find that with increasing concentration, the reaction current decreases and the iron dissolution rate decreases, but a passivation layer does not form on the surface. However there is some evidence from Raman spectroscopy that an adsorbed layer of $TFSI^-$ anions may form.

Lower currents in LiTFSI may be due to the large size and slow diffusion of TFSI anions, so they do not move quickly through the solution. This can create a diffusion-limited environment and a non-uniform ion distribution near the iron surface, resulting in low reaction current. The high concentrations of LiTFSI, leads to a high viscosity of the solution, which may impede the diffusion of ions and water molecules to the iron surface, which contributes to a decrease in the oxidation reaction current. There are also far fewer free water molecules, affecting the water layer around the iron, which is critical for subsequent dissolution. Without enough water, the oxidation reactions become less efficient.

To further understand the nature of LiTFSI solution, several other chemical methods can be used to gain a comprehensive understanding of the structural, dynamic, and reactive properties of LiTFSI and interactions with $Fe^{2+}$. One such method is the use of Nuclear Magnetic Resonance (NMR) Spectroscopy, which provides information on the dynamics and interactions of $Li^+$ and $TFSI^-$ ions with solvent molecules. Mass spectrometry (MS) can also provide information about ion composition, the presence of aggregates, and the potential formation of complex species in solution. Molecular Dynamics (MD) Simulations also provide detailed insights into the structure, dynamics, and interactions of ions in solution, complementing experimental data. It is also important to study the properties of the electrolyte by measuring its conductivity and viscosity.

Preliminary results regarding LiTFSI show that it is very viscous electrolyte and an unsuitable for applications such as an all-iron redox flow cell if used in high concentrations. At these high concentrations, the oxidation reaction becomes less efficient and thus the solubility of iron decreases.

# CHAPTER 7

# Conclusion

The development of all-iron redox flow batteries (Fe-RFBs) has become increasingly important in the search for sustainable and scalable energy storage solutions. Fe-RFBs offer a promising alternative to conventional energy storage technologies due to their low cost, environmental friendliness, and efficient redox processes. However, improving the performance of Fe-RFBs requires a deep understanding of the effect of electrolyte concentration on reactions, especially the anode reaction. In this thesis, the effect of different concentrations of lithium sulfate ($Li_2SO_4$) electrolyte (from 0.1 M to 2.5 M) on the anode reaction in Fe/Fe2+ cell was investigated using different techniques such as CV, Raman spectroscopy and IR as well as electrolyte viscosity and conductivity measurement. The main motivation for this study was to investigate the effect of higher concentrations of lithium sulfate electrolyte on the efficiency and stability of the anodic reaction as it is important in improving the overall performance of the Fe-RFBs.

At low concentrations, the results showed a slow rate of the anodic reaction due to limited ionic conductivity as there are fewer ions available in the electrolyte.
As the concentration increased, the ionic conductivity was sufficient to support more efficient electron transfer at the anode. The overall performance of the cell improved significantly in terms of reaction rates and increased anodic current.
At 1.8 M, the anodic reaction showed the highest current value. This concentration provided an ideal level of ionic conductivity to increase the number of ions in the electrolyte and increase its viscosity without the drawbacks observed at higher concentrations. This concentration allowed stable dissolution of iron ions without causing unwanted side reactions.

When the concentration was increased above 1.8 M, further increase in concentration negatively affected the performance. The viscosity increased with no increase in conductivity, which, which hindered the diffusion of ions. In addition, supersaturation of iron ions caused the precipitation of iron salts, which accumulated on the electrode surface, reducing the mobility of ions and

increasing the internal resistance. As a result, the effectiveness of the reaction decreased, and layers formed on the anode surface.

This study demonstrates that electrolyte concentration is an important factor in enhancing Fe-RFB performance. A balance between ionic conductivity and electrolyte stability must be achieved to maximize battery efficiency and longevity. At 1.8 M concentration, lithium sulfate provides sufficient ionic mobility to support a stable and efficient anodic reaction without experiencing the negative effects associated with higher concentrations

These results also highlight the importance of careful electrolyte engineering in Fe-RFB design. The ability to maintain high efficiency and extend the voltage window at the optimal concentration not only maximizes energy production but also supports long-term cycle stability. This improvement in battery performance is consistent with the broader motivations for Fe-RFB development, particularly the desire for sustainable, high-performance energy storage that can meet the demands of large-scale applications such as renewable energy storage and grid balancing.

The implications of these findings are important for the development of Fe-RFB technology. While Fe-RFBs already offer an attractive and cost-effective alternative to vanadium redox flow batteries (VRFBs), improving electrolyte concentration enhances their competitiveness.

Future work could explore alternative electrolyte or additives that stabilize iron ions at higher concentrations without causing precipitation, potentially allowing for higher energy densities.

More selective membrane designs and exploration of modified electrode surfaces could also enable Fe-RFBs to operate effectively at higher concentrations of lithium sulfate.

Understanding the electrolyte concentration limit is essential for scaling Fe-RFB technology. As these batteries scale to larger systems, achieving and maintaining optimal electrolyte balance will be critical to ensuring reliable performance across multiple operational scales.

This work advances a key aspect of Fe-RFBs, bringing them closer to real-world applications for large-scale energy storage needs.

Furthermore, the results contribute to the development of more efficient Fe-RFB systems, in line with the goals of developing sustainable and large-scale energy storage solutions. The results show that an electrolyte concentration of 1.8 M provides optimal performance for the anodic reaction in all-iron redox flow batteries. The results emphasize the importance of electrolyte concentration in achieving the desired balance between ionic conductivity and stability, supporting the broader goal of promoting Fe-RFB technology for large-scale energy storage applications. The insights gained here pave the way for future advances in electrolyte formulation, electrode design, and system scaling, emphasizing the importance of electrolyte optimization in the development of cost-effective and sustainable energy storage solutions.

## REFERENCE :


[1] A.Z. Weber, M.M. Mench, J.P. Meyers, P.N. Ross, J.T. Gostick, Q. Liu, Redox flow batteries: A review, J Appl Electrochem 41 (2011) 1137–1164. https://doi.org/10.1007/s10800-011-0348-2.

[2] H. Zhang, C. Sun, Cost-effective iron-based aqueous redox flow batteries for large-scale energy storage application: A review, J Power Sources 493 (2021) 229445. https://doi.org/10.1016/j.jpowsour.2020.229445.

[3] C. Ponce de León, A. Frías-Ferrer, J. González-García, D.A. Szánto, F.C. Walsh, Redox flow cells for energy conversion, J Power Sources 160 (2006) 716–732. https://doi.org/10.1016/j.jpowsour.2006.02.095.

[4] H. Zhang, X. Liu, H. Li, I. Hasa, S. Passerini, Challenges and Strategies for High-Energy Aqueous Electrolyte Rechargeable Batteries, Angewandte Chemie - International Edition 60 (2021) 598–616. https://doi.org/10.1002/anie.202004433.

[5] A. Aluko, A. Knight, A Review on Vanadium Redox Flow Battery Storage Systems for Large-Scale Power Systems Application, IEEE Access 11 (2023) 13773–13793. https://doi.org/10.1109/ACCESS.2023.3243800.

[6] C. Doetsch, J. Burfeind, Vanadium redox flow batteries, Storing Energy: With Special Reference to Renewable Energy Sources (2022) 363–381. https://doi.org/10.1016/B978-0-12-824510-1.00030-1.

[7] A. Dinesh, S. Olivera, K. Venkatesh, M.S. Santosh, M.G. Priya, Inamuddin, A.M. Asiri, H.B. Muralidhara, Iron-based flow batteries to store renewable energies, Environ Chem Lett 16 (2018) 683–694. https://doi.org/10.1007/s10311-018-0709-8.

[8] Y.K. Zeng, T.S. Zhao, L. An, X.L. Zhou, L. Wei, A comparative study of all-vanadium and iron-chromium redox flow batteries for large-scale energy storage, J Power Sources 300 (2015) 438–443. https://doi.org/10.1016/j.jpowsour.2015.09.100.

[9] Y.K. Zeng, X.L. Zhou, L. An, L. Wei, T.S. Zhao, A high-performance flow-field structured iron-chromium redox flow battery, J Power Sources 324 (2016) 738–744. https://doi.org/10.1016/j.jpowsour.2016.05.138.

[10] H. Chen, X. Zhang, shirui zhang, S. Wu, F. Chen, J. Xu, A comparative study of iron-vanadium and all-vanadium flow battery for large scale energy storage, Chemical Engineering Journal 429 (2022) 132403. https://doi.org/10.1016/j.cej.2021.132403.

[11] S. Selverston, R.F. Savinell, J.S. Wainright, Zinc-Iron Flow Batteries with Common Electrolyte, J Electrochem Soc 164 (2017) A1069–A1075. https://doi.org/10.1149/2.0591706jes.

[12] X. Zhou, L. Lin, Y. Lv, X. Zhang, Q. Wu, A Sn-Fe flow battery with excellent rate and cycle performance, J Power Sources 404 (2018) 89–95. https://doi.org/10.1016/j.jpowsour.2018.10.011.

[13] S. Yu, X. Yue, J. Holoubek, X. Xing, E. Pan, T. Pascal, P. Liu, A low-cost sulfate-based all iron redox flow battery, J Power Sources 513 (2021) 230457. https://doi.org/10.1016/j.jpowsour.2021.230457.

[14] L.W. Hruska, R.F. Savinell, Investigation of Factors Affecting Performance of the Iron-Redox Battery, J Electrochem Soc 128 (1981) 18–25. https://doi.org/10.1149/1.2127366.

[15] H. Susanto, Chemistry and Industrial Techniques for Chemical Engineers, 2020. https://doi.org/10.1201/9780429286674.

[16] J. Jiang, J. Liu, Iron anode-based aqueous electrochemical energy storage devices: Recent advances and future perspectives, Interdisciplinary Materials 1 (2022) 116–139. https://doi.org/10.1002/idm2.12007.
[17] J. Chullipparambil Balakrishnan, M. Pulikkotti Peter, D. Davis Kombarakaran, J. Ambadan Kunjilona, J. Vadakkan Thomas, Improvement in the Performance of an Fe/FeII Electrode in an All-Iron Redox Flow Battery by the addition of ZnII ions, ChemistrySelect 7 (2022) 1–8. https://doi.org/10.1002/slct.202201222.
[18] B.S. Jayathilake, E.J. Plichta, M.A. Hendrickson, S.R. Narayanan, Improvements to the Coulombic Efficiency of the Iron Electrode for an All-Iron Redox-Flow Battery, J Electrochem Soc 165 (2018) A1630–A1638. https://doi.org/10.1149/2.0451809jes.
[19] K.L. Hawthorne, T.J. Petek, M.A. Miller, J.S. Wainright, R.F. Savinell, An Investigation into Factors Affecting the Iron Plating Reaction for an All-Iron Flow Battery, J Electrochem Soc 162 (2015) A108–A113. https://doi.org/10.1149/2.0591501jes.
[20] F. Desai, N. Seyedhassantehrani, M. Shagar, S. Gu, R. Asmatulu, Preparation and characterization of KOH-treated electrospun nanofiber mats as electrodes for iron-based redox-flow batteries, J Energy Storage 27 (2020) 101053. https://doi.org/10.1016/j.est.2019.101053.
[21] D. Anarghya, M.S. Anantha, K. Venkatesh, M.S. Santosh, M.G. Priya, H.B. Muralidhara, Bermuda grass derived nitrogen-doped carbon as electrocatalyst in graphite felt electrode to increase the efficiency of all-iron redox flow batteries, Journal of Electroanalytical Chemistry 878 (2020) 114577. https://doi.org/10.1016/j.jelechem.2020.114577.
[22] A. Dinesh, M.S. Anantha, M.S. Santosh, M.G. Priya, K. Venkatesh, K.S. Yogesh Kumar, M.S. Raghu, H.B. Muralidhara, Improved performance of iron-based redox flow batteries using WO3 nanoparticles decorated graphite felt electrode, Ceram Int 47 (2021) 10250–10260. https://doi.org/10.1016/j.ceramint.2020.09.225.
[23] M.S. Anantha, D. Anarghya, C. Hu, N. Reddy, K. Venkatesh, H.B. Muralidhara, Electrochemical performance of graphene oxide modified graphite felt as a positive electrode in all-iron redox flow batteries, J Appl Electrochem 51 (2021) 331–344. https://doi.org/10.1007/s10800-020-01490-5.
[24] T. V. Sawant, J.R. Mckone, Flow Battery Electroanalysis: Hydrodynamic Voltammetry of Aqueous Fe(III/II) Redox Couples at Polycrystalline Pt and Au, ACS Appl Energy Mater 1 (2018) 4743–4753. https://doi.org/10.1021/acsaem.8b00859.
[25] M. Furquan, S. Ali, S.R. Hussaini, Z.M. Bhat, M.A.Z.G. Sial, A.S. Alzahrani, Z.H. Yamani, M. Qamar, Electrolyte Additives and 3D X-ray Tomography Study of All Iron Redox Flow Batteries in a Full-Cell Configuration for High Capacity Retention, Energy and Fuels 38 (2024) 4699–4710. https://doi.org/10.1021/acs.energyfuels.3c04842.
[26] X. Liu, T. Li, Z. Yuan, X. Li, Low-cost all-iron flow battery with high performance towards long-duration energy storage, Journal of Energy Chemistry 73 (2022) 445–451. https://doi.org/10.1016/j.jechem.2022.06.041.
[27] M. Shin, C. Noh, Y. Kwon, Stability enhancement for all-iron aqueous redox flow battery using iron-3-[bis(2-hydroxyethyl)amino]-2-hydroxypropanesulfonic acid complex and ferrocyanide as redox couple, Int J Energy Res 46 (2022) 6866–6875. https://doi.org/10.1002/er.7535.
[28] J.E. Enderby, G.W. Neilson, The structure of electrolyte solutions, Reports on Progress in Physics 44 (1981) 593–653. https://doi.org/10.1088/0034-4885/44/6/001.

[29] M. Sha, H. Dong, F. Luo, Z. Tang, G. Zhu, G. Wu, Dilute or Concentrated Electrolyte Solutions? Insight from Ionic Liquid/Water Electrolytes, Journal of Physical Chemistry Letters 6 (2015) 3713–3720. https://doi.org/10.1021/acs.jpclett.5b01513.
[30] C.H. Lin, K. Sun, M. Ge, L.M. Housel, A.H. McCarthy, M.N. Vila, C. Zhao, X. Xiao, W.K. Lee, K.J. Takeuchi, E.S. Takeuchi, A.C. Marschilok, Y.C.K. Chen-Wiegart, Systems-level investigation of aqueous batteries for understanding the benefit of water-in-salt electrolyte by synchrotron nanoimaging, Sci Adv 6 (2020) 1–11. https://doi.org/10.1126/sciadv.aay7129.
[31] T.S. Groves, C.S. Perez-Martinez, R. Lhermerout, S. Perkin, Surface Forces and Structure in a Water-in-Salt Electrolyte, Journal of Physical Chemistry Letters 12 (2021) 1702–1707. https://doi.org/10.1021/acs.jpclett.0c03718.
[32] P. Iamprasertkun, A. Ejigu, R.A.W. Dryfe, Understanding the electrochemistry of "water-in-salt" electrolytes: Basal plane highly ordered pyrolytic graphite as a model system, Chem Sci 11 (2020) 6978–6989. https://doi.org/10.1039/d0sc01754j.
[33] S.J. Konopka, B. McDuffie, Diffusion Coefficients of Ferri- and Ferrocyanide Ions in Aqueous Media, Using Twin-Electrode Thin-Layer Electrochemistry, Anal Chem 42 (1970) 1741–1746. https://doi.org/10.1021/ac50160a042.
[34] S. Prasad, C. Chakravarty, H.K. Kashyap, Concentration-dependent structure and dynamics of aqueous LiCl solutions: A molecular dynamics study, J Mol Liq 225 (2017) 240–250. https://doi.org/10.1016/j.molliq.2016.11.042.
[35] M. Cho, J. Jeon, Ion transport in super-concentrated aqueous electrolytes for lithium-ion batteries, Journal of Physical Chemistry C 125 (2021) 23622–23633. https://doi.org/10.1021/acs.jpcc.1c07382.
[36] O. Borodin, L. Suo, M. Gobet, X. Ren, F. Wang, A. Faraone, J. Peng, M. Olguin, M. Schroeder, M.S. Ding, E. Gobrogge, A. Von Wald Cresce, S. Munoz, J.A. Dura, S. Greenbaum, C. Wang, K. Xu, Liquid Structure with Nano-Heterogeneity Promotes Cationic Transport in Concentrated Electrolytes, ACS Nano 11 (2017) 10462–10471. https://doi.org/10.1021/acsnano.7b05664.
[37] L. Chen, J. Zhang, Q. Li, J. Vatamanu, X. Ji, T.P. Pollard, C. Cui, S. Hou, J. Chen, C. Yang, L. Ma, M.S. Ding, M. Garaga, S. Greenbaum, H.S. Lee, O. Borodin, K. Xu, C. Wang, A 63 m Superconcentrated Aqueous Electrolyte for High-Energy Li-Ion Batteries, ACS Energy Lett 5 (2020) 968–974. https://doi.org/10.1021/acsenergylett.0c00348.
[38] M. Okoshi, C.P. Chou, H. Nakai, Theoretical Analysis of Carrier Ion Diffusion in Superconcentrated Electrolyte Solutions for Sodium-Ion Batteries, Journal of Physical Chemistry B 122 (2018) 2600–2609. https://doi.org/10.1021/acs.jpcb.7b10589.
[39] P. Atkins, Atkins' Physical Chemistry, 2010.
[40] H. Paulsen, Cyclic Voltammetry-"Electrochemical Spectroscopy", Angewandte Chemie International Edition In English 23 (1984) 831–918. http://onlinelibrary.wiley.com/doi/10.1002/anie.198201553/abstract.
[41] A.C.Fisher, Electrode Dynamics, Oxford University Press Inc (1996).
[42] I.H.A. Al-Omairi, M.M. Radhi, A.A. Mohsin, Electrocatalytic Reduction and Voltammetric Determination of Curcumin by Blood Medium, International Journal of Drug Delivery Technology 12 (2022) 1604–1607. https://doi.org/10.25258/ijddt.12.4.21.
[43] R.N. Vyas, B. Wang, Electrochemical analysis of conducting polymer thin films, Int J Mol Sci 11 (2010) 1956–1972. https://doi.org/10.3390/ijms11041956.
[44] K. Mukherjee, S. Palchowdhury, M. Maroncelli, OH Stretching and Libration Bands of Solitary Water in Ionic Liquids and Dipolar Solvents Share a Single

Dependence on Solvent Polarity, Journal of Physical Chemistry B 126 (2022) 4584–4598. https://doi.org/10.1021/acs.jpcb.2c02445.
[45] E.Smith, G.Dent, Modern Raman Spectroscopy-Apractical Approch, 2005.
[46] J. Saveant, Molecular Catalysis of Electrochemical Reactions, Chem Rev 108 (2008) 2348–2378.
[47] R. McCreey, Raman Spectroscopy for Chemical Analysis, 2000.
[48] Y. Li XX, Blinn K, Fang, Application of Surface Enhanced Raman Spectroscopy to the study of SOFC electrode surfaces, Physical Chemistry 14 (2012) 919–923.
[49] B.L. Mojet, S.D. Ebbesen, L. Lefferts, Light at the interface: The potential of attenuated total reflection infrared spectroscopy for understanding heterogeneous catalysis in water, Chem Soc Rev 39 (2010) 4643–4655. https://doi.org/10.1039/c0cs00014k.
[50] N. Kitadai, T. Sawai, R. Tonoue, S. Nakashima, M. Katsura, K. Fukushi, Effects of ions on the oh stretching band of water as revealed by atr-ir spectroscopy, J Solution Chem 43 (2014) 1055–1077. https://doi.org/10.1007/s10953-014-0193-0.
[51] Stuart.B, Infrared Spectroscopy, 2014.
[52] T.S.R. Group, Fourier Transform Infrared (FTIR)- Attenuated Total Reflection (ATR) Spectroscopy, [Online]. Available: Https://Sites.Temple.Edu/Strongingroup/Laboratories/Atr/ (2018).
[53] P. Lakin, Infrared and Raman Spectroscopy, Elsevier (2011).
[54] S. and Liang.C. Krimm, Infrared Spectra of High Polymers, J. Mol. Spectrosc. 3 (1959) 554–574.
[55] X. You, C.R. Baiz, Importance of Hydrogen Bonding in Crowded Environments: A Physical Chemistry Perspective, Journal of Physical Chemistry A 126 (2022) 5881–5889. https://doi.org/10.1021/acs.jpca.2c03803.
[56] J. Zheng, J.A. Lochala, A. Kwok, Z.D. Deng, J. Xiao, Research Progress towards Understanding the Unique Interfaces between Concentrated Electrolytes and Electrodes for Energy Storage Applications, Advanced Science 4 (2017) 1–19. https://doi.org/10.1002/advs.201700032.
[57] E.R. Nightingale, Phenomenological theory of ion solvation. Effective radii of hydrated ions, Journal of Physical Chemistry 63 (1959) 1381–1387. https://doi.org/10.1021/j150579a011.
[58] S.J. Konopka, B. McDuffie, Diffusion Coefficients of Ferri- and Ferrocyanide Ions in Aqueous Media, Using Twin-Electrode Thin-Layer Electrochemistry, Anal Chem 42 (1970) 1741–1746. https://doi.org/10.1021/ac50160a042.
[59] H. Adler, THE AMERICAN MINERALOGIST,Vol 50, n.d.
[60] M. Zhang, Y. Gao, L. Fu, Y. Bai, S. Mukherjee, C.L. Chen, J. Liu, H. Bian, Y. Fang, Chain-like Structures Facilitate Li+ Transport in Concentrated Aqueous Electrolytes: Insights from Ultrafast Infrared Spectroscopy and Molecular Dynamics Simulations, Journal of Physical Chemistry Letters 14 (2023) 6968–6976. https://doi.org/10.1021/acs.jpclett.3c01494.
[61] W. Wachter, ˇSarka Fernandez, G. Hefter, R. Buchner, Ion Association and Hydration in Aqueous Solutions of LiCl and Li SO by Dielectric 24 Spectroscopy, J. Phys. Chem 71 (2007) 5287–5300. https://doi.org/10.1016/j.gca.2007.08.026.
[62] K. Takahashi, J.A. ; Bardwell, B. ; MacDougall, M.J. ; Graham, Mechanism of anodic dissolution and passivation of iron - I . Behavior in neutral acetate buffer solutions MECHANISM OF ANODIC DISSOLUTION AND, Electrochim Acta (1992) 477–487.

[63] F. Hibert, Y. Miyoshi, G. Eichkorn, W.J. Lorenz, Correlations between the Kinetics of Electrolytic Dissolution and Deposition of Iron, J Electrochem Soc 118 (1971) 1927. https://doi.org/10.1149/1.2407869.
[64] J.J. Podestá, A.J. Arvía, Kinetics of the anodic dissolution of iron in concentrated ionic media: galvanostatic and potentiostatic measurements, Electrochim Acta 10 (1965) 171–182. https://doi.org/10.1016/0013-4686(65)87017-7.
[65] P. Russell, J. Newman, Anodic Dissolution of Iron in Acidic Sulfate Electrolytes: I . Formation and Growth of a Porous Salt Film, J Electrochem Soc 133 (1986) 59–69. https://doi.org/10.1149/1.2108541.
[66] Z.A. Foroulis, Kinetics of Anodic Dissolution of Iron in High Purity Water., Boshoku Gijutsu 28 (1979) 10–17. https://doi.org/10.3323/jcorr1974.28.1_10.
[67] M.A. Maleeva, A.A. Rybkina, A.I. Marshakov, V. V. Elkin, The effect of atomic hydrogen on the anodic dissolution of iron in a sulfate electrolyte studied with impedance spectroscopy, Protection of Metals 44 (2008) 548–556. https://doi.org/10.1134/S0033173208060039.
[68] L. Nikolić-Bujanović, M. Čekerevac, M. Vojinović-Miloradov, A. Jokić, M.Š. Simičić, A comparative study of iron-containing anodes and their influence on electrochemical synthesis of ferrate(VI), Journal of Industrial and Engineering Chemistry 18 (2012) 1931–1936. https://doi.org/10.1016/j.jiec.2012.05.007.
[69] C.M. Chu, C.C. Wan, Effect of citric acid as a chelating agent on anodic behavior of pure iron with potentiostatic polarization and cyclic voltammetry methods, Mater Chem Phys 33 (1993) 189–196. https://doi.org/10.1016/0254-0584(93)90061-P.
[70] D.S. Azambuja, I.L. Muller, The influence of acetate concentration on the dissolution of iron in aqueous solutions, Corros Sci 36 (1994) 1835–1845. https://doi.org/10.1016/0010-938X(94)90022-1.
[71] V. Rouchon, H. Badet, O. Belhadj, O. Bonnerot, B. Lavódrine, J.G. Michard, S. Miska, Raman and FTIR spectroscopy applied to the conservation report of paleontological collections: Identification of Raman and FTIR signatures of several iron sulfate species such as ferrinatrite and sideronatrite, Journal of Raman Spectroscopy 43 (2012) 1265–1274. https://doi.org/10.1002/jrs.4041.
[72] S.K. Sharma, C.H. Chio, D.W. Muenow, RAMAN SPECTROSCOPIC INVESTIGATION OF FERROUS SULFATE HYDRATES, Hawaii Institute of Geophysics and Planetology (2006).
[73] I.U.T. Bethune, R.D.B. P, B. Cedex, IdentiÐcation of newly generated iron phases in recent anoxic sediments : 57 Fe Mo □ ssbauer and microRaman spectroscopic studies, J. Chem. Soc. 93 (1997) 3209–3215.
[74] J. Liu, D. Dong, A.L. Caro, N.S. Andreas, Z. Li, Y. Qin, D. Bedrov, T. Gao, Aqueous Electrolytes Reinforced by Mg and Ca Ions for Highly Reversible Fe Metal Batteries, ACS Cent Sci 8 (2022) 729–740. https://doi.org/10.1021/acscentsci.2c00293.
[75] A. Serva, N. Dubouis, A. Grimaud, M. Salanne, Confining Water in Ionic and Organic Solvents to Tune Its Adsorption and Reactivity at Electrified Interfaces, Acc Chem Res 54 (2021) 1034–1042. https://doi.org/10.1021/acs.accounts.0c00795.
[76] F. Lundin, L. Aguilera, H.W. Hansen, S. Lages, A. Labrador, K. Niss, B. Frick, A. Matic, Structure and dynamics of highly concentrated LiTFSI/acetonitrile electrolytes, Physical Chemistry Chemical Physics 23 (2021) 13819–13826. https://doi.org/10.1039/d1cp02006d.
[77] L. Suo, F. Zheng, Y.S. Hu, L. Chen, FT-Raman spectroscopy study of solvent-in-salt electrolytes, Chinese Physics B 25 (2015). https://doi.org/10.1088/1674-1056/25/1/016101.

[78] W. Kam, C.W. Liew, J.Y. Lim, S. Ramesh, Electrical, structural, and thermal studies of antimony trioxide-doped poly(acrylic acid)-based composite polymer electrolytes, Ionics (Kiel) 20 (2014) 665–674. https://doi.org/10.1007/s11581-013-1012-0.
[79] M. Sasikumar, A. Jagadeesan, M. Raja, R. Hari Krishna, P. Sivakumar, The effects of PVAc on surface morphological and electrochemical performance of P(VdF-HFP)-based blend solid polymer electrolytes for lithium ion-battery applications, Ionics (Kiel) 25 (2019) 2171–2181. https://doi.org/10.1007/s11581-018-2679-z.
[80] J. Han, A. Mariani, S. Passerini, A. Varzi, A perspective on the role of anions in highly concentrated aqueous electrolytes, Energy Environ Sci 16 (2023) 1480–1501. https://doi.org/10.1039/d2ee03682g.

# Appendix : Additional Figures for Chapter 5

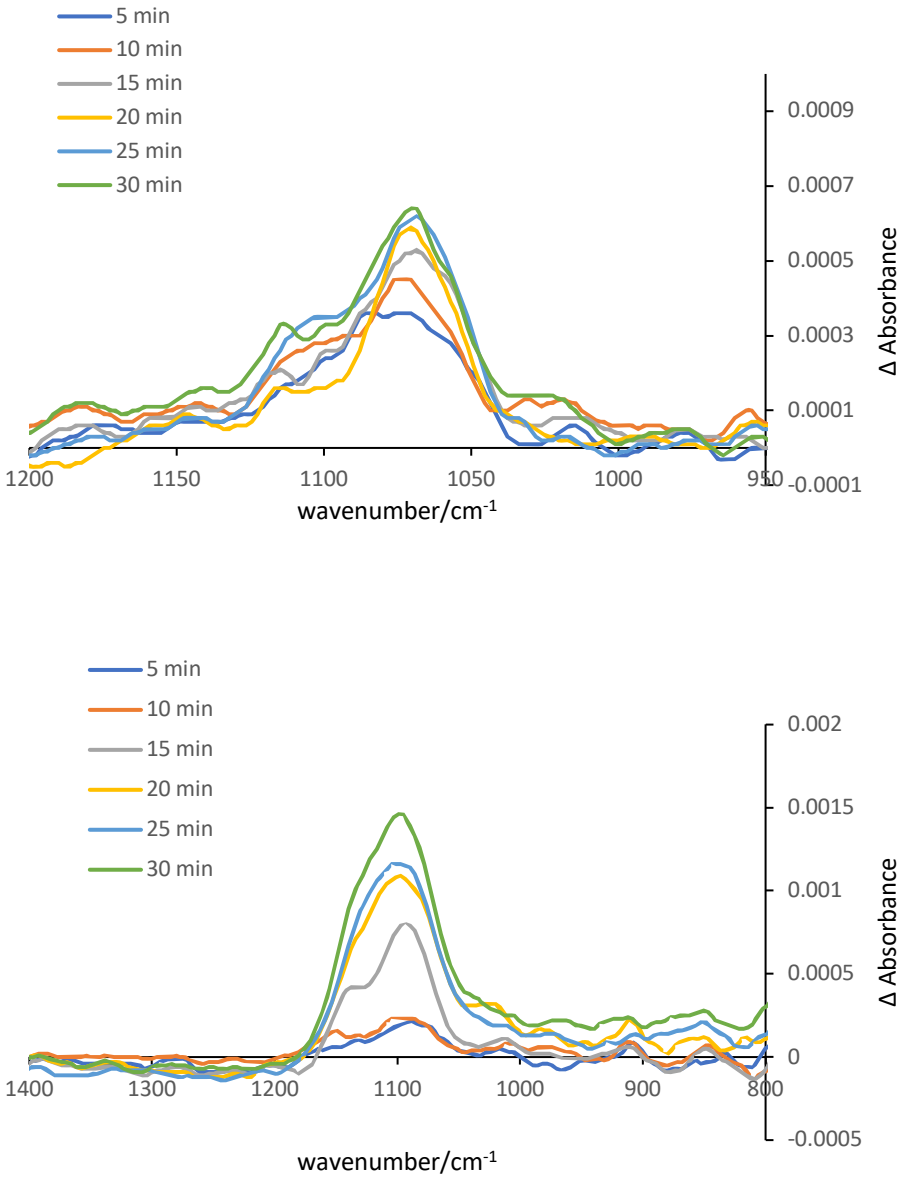


**Figure A.1** Infrared spectrum of iron electrode in a) 0.1 and b)0.4 M $Li_2SO_4$ at -0.4 V.

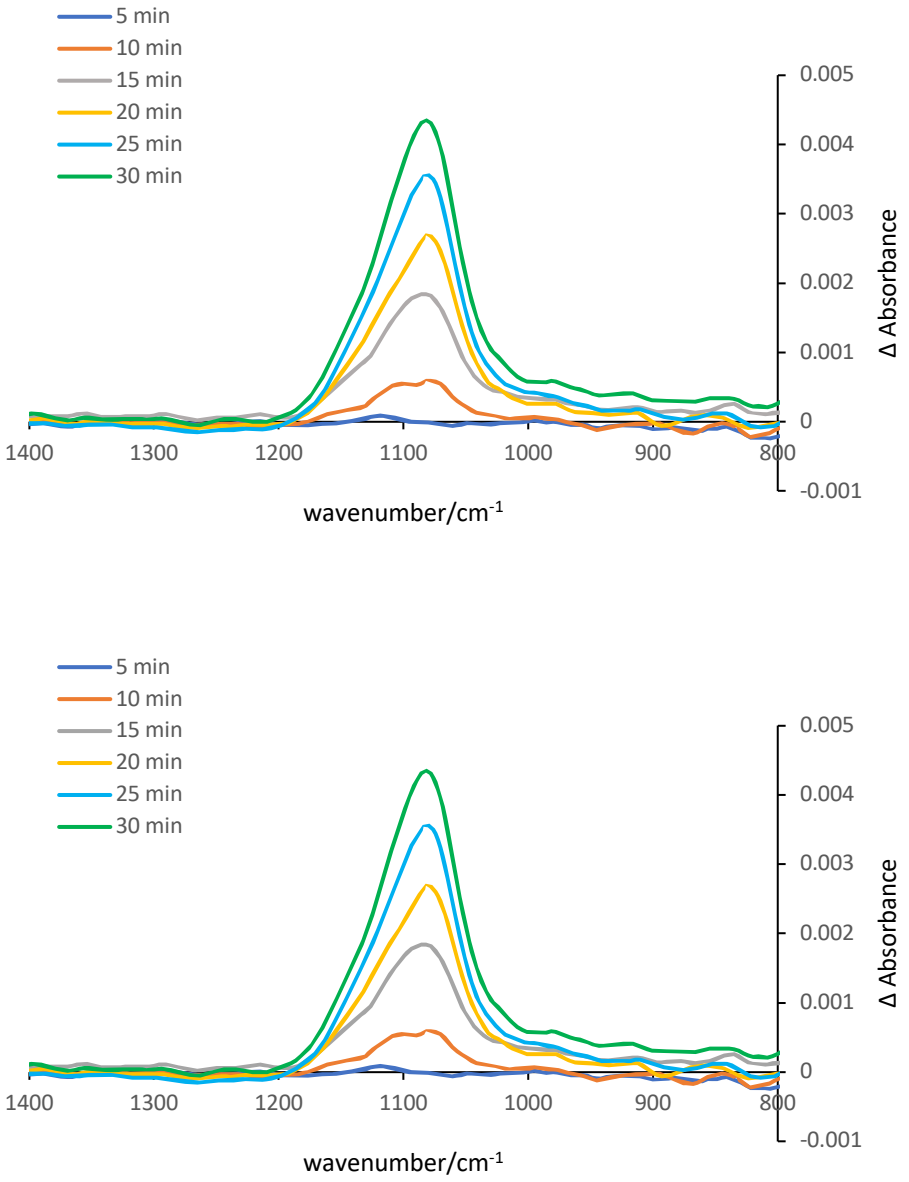


**Figure A.2** Infrared spectrum of iron electrode in a) 1 and b)1.8 M $Li_2SO_4$ at -0.4 V.

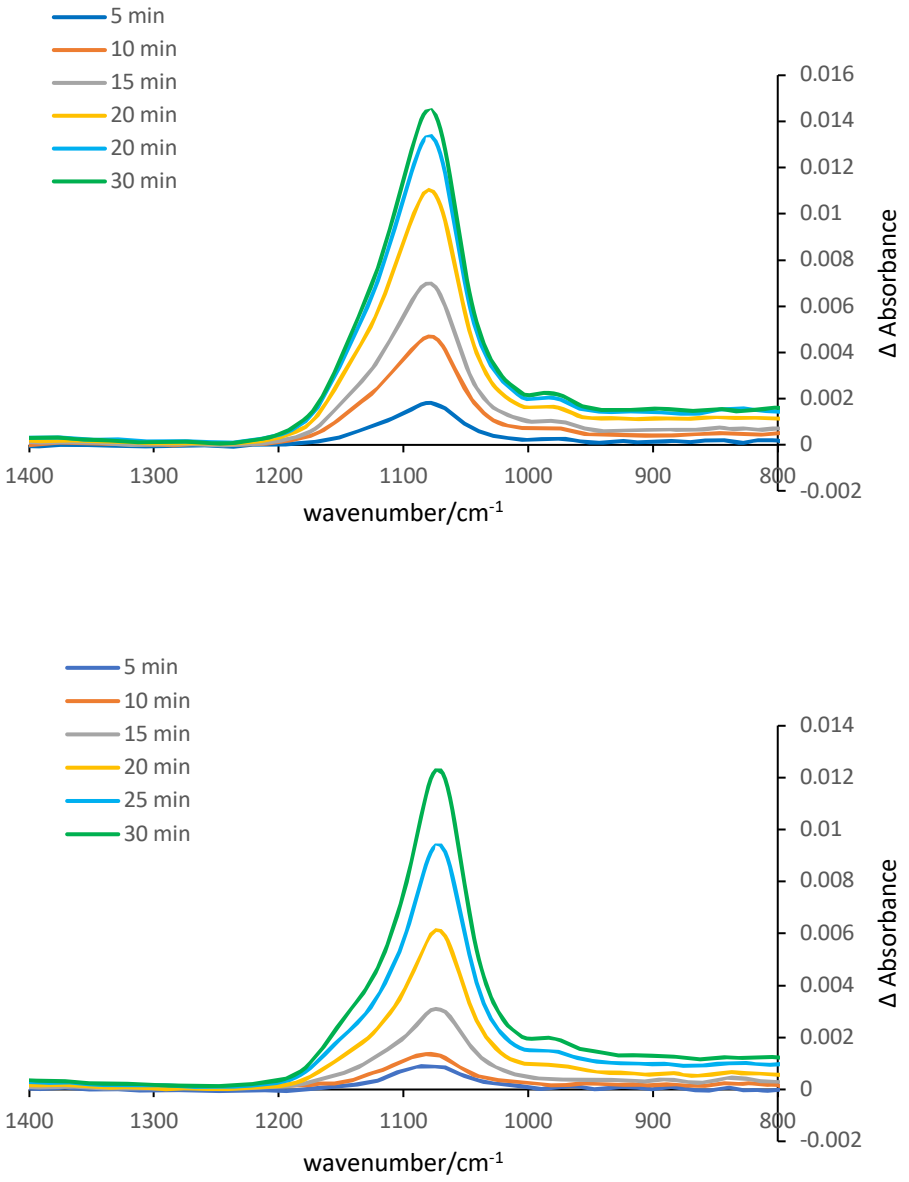


**Figure A.3** Infrared spectrum of iron electrode in a)2 and b)2.5 M $Li_2SO_4$ at -0.4 V.